THESIS FOR THE DEGREE OF DOCTOR OF PHILOSOPHY

Intermodulation Distortion in Periodic Structures and Microstructures

Martin Mattsson

CHALMERS
UNIVERSITY OF TECHNOLOGY

Department of Microtechnology and Nanoscience - MC2
Chalmers University of Technology
Gothenburg, Sweden, 2025

Intermodulation Distortion in Periodic Structures and Microstructures

Martin Mattsson

ISBN: 978-91-8103-181-2

Doktorsavhandlingar vid Chalmers tekniska högskola
Ny serie nr 5639
ISSN 0346-718X

Chalmers University of Technology
Department of Microtechnology and Nanoscience - MC2
Microwave Electronics Laboratory
SE-412 96 Gothenburg, Sweden
Phone: +46 (0)31 772 1000

Printed by Chalmers digitaltryck
Gothenburg, Sweden, February 2025

Till Sofie och Tage

Abstract

The rapid growth of wireless communication increases the demand for higher data rates, low latency, and availability. This leads to a complex infrastructure where multiple systems coexist in a densely populated frequency spectrum, requiring multi-carrier systems with high power and sensitive receivers. However, the requirements of modern communication systems increase the risk of interference from weak spurious signals. The spurious signals result from nonlinear mixing of two or more signals with different frequencies. The mixing products are denoted as intermodulation distortion (IMD) in active devices and passive intermodulation (PIM) in passive ones. The demand for highly linear devices is increasing due to these new challenges. As a result, understanding nonlinear behavior is crucial to develop accurate nonlinear models that will help mitigate IMD and PIM.

This thesis analyzes and models nonlinear effects in different structures, where the first part regards IMD in periodic structures. The periodic structure employed in this thesis is a loaded-line phase shifter that is periodically loaded by varactor-diodes. Various design factors were studied, including periodicity, bias, input power, and unit cell configuration. A polynomial varactor model was validated experimentally and scaled for circuit simulations to optimize phase-shift/loss and linearity. Results showed that evenly distributing varactor capacitance improves phase shift/loss, with a trade-off between minimizing loss and IMD.

The second part of this thesis explores PIM generation in microstructures. Firstly, PIM was analyzed using a rectangular coaxial transmission line with a replaceable aluminum alloy (AlSi10Mg) center conductor fabricated via additive manufacturing (AM) and compared to a milled aluminum counterpart. A nonlinear distributed transmission line was developed. It was found that AM fabricated conductors exhibit higher PIM levels due to increased surface roughness.

Secondly, the generation of PIM in anodized antenna feeding networks for satellite communications was analyzed. It was found that anodization could both improve and degrade PIM performance compared to untreated feeding networks. Cracks formed in the anodized coating, which were hypothesized to act as nonlinear sources. A thinner anodized coating resulted in fewer cracks and the best PIM performance, while a thicker coating produced more cracks and led to the worst PIM performance.

Keywords: Intermodulation distortion, passive intermodulation, loaded-line phase shifter, nonlinear analysis, additive manufacturing, thermal coating

List of publications

The following appended papers constitute the main work for this thesis:

[A] **M. Mattsson**, K. Buisman, and D. Kuylenstierna, “Modeling of intermodulation in a loaded-line phase shifter based on a polynomial varactor model,” in *International Journal of Microwave and Wireless Technologies,* vol. 16, no. 7, pp. 1113–1124, 2024.

[B] **M. Mattsson** and D. Kuylenstierna, "Multi-source Intermodulation in a Loaded-line Phase Shifter," in *2020 50th European Microwave Conference (EuMC),* Utrecht, Netherlands, 2021, pp. 280-283.

[C] **M. Mattsson** and D. Kuylenstierna, "Experimental Investigation of Distributed Intermodulation in an Artificial Transmission Line," in *Multipactor, Corona and Passive Intermodulation (MULCOPIM),* Valencia, Spain, 2022.

[D] **M. Mattsson**, Q. Khan, J. Karlsson, A. Svanberg, P. Magnusson, K. Buisman and D. Kuylenstierna, "Passive Intermodulation in 3D Printed Coaxial Transmission Lines", submitted to the *IEEE Journal on Multiscale and Multiphysics Computational Techniques,* Feb. 2025.

[E] **M. Mattsson**, R. Udiljak, J. Johansson, K. Buisman, and D. Kuylenstierna, "Passive Intermodulation in Surface Treated Antenna Feeding Networks", *manuscript,* Feb. 2025.

Other publications:

[a] **M. Mattsson**, "Intermodulation distortion in active and passive components". Lic. Dissertation Gothenburg, Sweden: Chalmers University of Technology, May, 2023.

As part of the authors’ doctoral studies, some of the work has previously been published in [a]. Text, figures, and tables from [a] may therefore be fully or partly reproduced in this thesis.

Acknowledgments

Since moving to Gothenburg and starting my doctoral studies, I have met so many amazing people. I am truly grateful for all the support, friendships, and experiences, and I want to express my gratitude.

First of all, I would like to thank my supervisor, Dan Kuylenstierna, for the invaluable guidance and support throughout this journey. I truly appreciate your generosity with your time, and your fast and great feedback. It has been a privilege to learn from you and to have you as my supervisor.

Secondly, I would like to thank all of my co-supervisors Koen Buisman, Joakim Johansson, and Richard Udiljak. Thank you for the support and all the technical discussions we have had, which have enriched my knowledge and improved my work.

I also want to sincerely thank my examiner, Christian Fager, for your support and for always making time to help whenever I needed it.

I am grateful to everyone I have met at the Microwave Electronics Laboratory. Working here has been a wonderful experience, and I feel fortunate that some of my colleagues have become close friends. A special thanks to Olivier, Hassona, Juan, Frida, Han, Decha, Göksu, Rob, Jonas, Ibrahim, and Vessen. You have made my working experience great but, more importantly, made life outside work enjoyable and memorable. My experience during this time has been truly amazing because of all of you.

To all my friends in Stockholm, thank you for all the amazing memories we have made together. You always bring so much joy into my life, and I am so grateful for that!

I want to thank my wonderful mom, dad, and brothers, for all their support and always being there for me. I am incredibly lucky to have you in my life.

Lastly, I want to express my deepest gratitude to my two favorite people and biggest supporters, Sofie and Tage. Thank you for always being there for me, lifting me up during stressful times, and creating a wonderful home to return to. Your support and love mean the world to me. You are the best part of this journey and the highlight of every day!

Notations and abbreviations

Notations

A_c	Area of crack
$\bar{B}$	Normalized load susceptance
C_0	Load capacitance of loaded transmission line
C_j	Variable junction capacitance
C_{j0}	Zero bias junction capacitance
C_n	Polynomial coefficient of the n^{th}-order
C_p	Parallel capacitance in varactor model
C_t	Shunt capacitance per unit cell length
C_v	Thermal capacity at constant volume
C_V	Varactor-diode capacitance
c_0	Speed of light in vacuum
d	Period of periodic structure
f	Frequency
f_B	Bragg frequency
$F_{\Delta\phi}$	Phase shifter figure of merit [deg./dB]
j_0	Current density distribution
J	Current density
L_s	Series inductance in varactor model
L_{dB}	Loss in dB
n	Grading coefficient in diode
R_2	Macroscopic nonlinear resistance
R_{th}	Thermal resistance
R_s	Series resistance in varactor model
T	Temperature
V_b	Breakdown voltage
V_R	Reversed bias voltage
Z_0	Unloaded transmission line impedance
Z_e	Effective characteristic impedance of loaded transmission line
β	Phase constant in loaded line phase shifter
Γ	Geometrical factor
$\Delta\phi$	Differential phase shift
ϵ_r	Relative electric permittivity
ϕ	Built-in potential in diode
ρ_{e0}	Static resistivity
θ_0	Electrical length of unloaded transmission line

θ_e	Effective electrical length of loaded transmission line
ω	Angular frequency

Abbreviations

5G:	Fifth generation Mobile Network
6G:	Sixth generation Mobile Network
ADS:	Advanced Design System
Al_2O_3:	Aluminum oxide
AM:	Additive Manufacturing
BPF:	Bandpass Filter
CPWG:	Grounded Coplanar Waveguide
dB:	Decibel
dBc:	Decibel Relative to Carrier
dBm:	Decibel Relative to 1 Milliwatt
DC:	Direct Current
DUT:	Device Under Test
FEM:	Finite Element Method
FIB:	Focused Ion Beam
FOM:	Figure Of Merit
HD_2:	Second-order Harmonic Distortion
HD_3:	Third-order Harmonic Distortion
IL:	Insertion Loss
IM:	Intermodulation
IM_2:	Second-order Intermodulation Distortion
IM_3:	Third-order Intermodulation Distortion

IM_5:	Fifth-order Intermodulation Distortion
IMD:	Intermodulation Distortion
IoT:	Internet of Things
IV:	Current-Voltage
IP_3:	Third-order Intercept Point
IIP_3:	Input Third-order Intercept Point
OIP_3:	Output Third-order Intercept Point
MM:	Metal-to-Metal
MIM:	Metal-Insulator-Metal
PBF-LB:	Powder Bed Fusion - Laser Beam
PCB:	Printed Circuit Board
PIM:	Passive Intermodulation
P1dB:	1-dB Compression Point
QV:	Charge-Voltage
RL:	Return Loss
RF:	Radio-Frequency
SEM:	Scanning Electron Microscope
S-parameters:	Scattering parameters
S1P:	1-port S-parameter
TRL:	Through-Reflect-Line
TWT:	Traveling Wave Tube
UC:	Unit Cell
VNA:	Vector Network Analyzer
Y2P:	2-port Equation-based Admittance

Contents

CHAPTER 1

Introduction

Wireless technology is essential in our modern society and is used in personal, professional, industrial, and scientific contexts. It has experienced immense growth during the past few decades due to its broad range of applications, e.g., Bluetooth, wireless internet, telecommunications, satellite communications, and deep space communications. Global mobile network data traffic is one area that has grown tremendously in the last decade, and the data traffic has increased from 18 exabytes (EB) per month at the beginning of 2018 to 157 EB per month at the end of 2024 [1]. This increase is driven mainly by video traffic, which accounts for approximately 74% of all mobile data traffic. The data traffic is projected to increase to 473 EB per month by the end of 2030. The deployment of the 5^{th} generation (5G) of cellular network technology is one of the recent advancements in wireless technology, which will accommodate the growing demand for higher data rates, lower latency, and availability. 5G mobile subscriptions currently make up 25% of all subscriptions, which is projected to increase to 80% by 2030 [1].

Moreover, satellite communication is another expanding area with several applications, such as Earth observation, navigation, weather forecasting, broadcasting, and telecommunication. Satellite communication is expected to be an integral part of the 5G and beyond communication systems. The 5G Non-Terrestrial Network is expected to enhance reliability and improve 5G capabilities for moving platforms and remote areas [2]. This technology can be used for backhauling, helping to offload the primary terrestrial network, and

enabling Internet of Things (IoT) services [2], [3]. Satellite internet service is another expanding area, with Starlink actively launching a satellite internet mega-constellation [4]. The initial deployment approved by the U.S. Federal Communication Commission involves 4,425 satellites in low Earth orbit and 7,518 in very low Earth orbit [5].

The ongoing and future advancements in wireless technology result in increased capacity, enabling us to meet the rising demand for higher data rates, lower latency, and better availability. These improvements also allow for new technologies, such as IoT. However, many new challenges are also introduced with higher capacity. Several changes are made to increase the capacity, such as higher frequencies, higher power signals, more systems with multiple input/output signals, and a more complex infrastructure where several communication systems have to co-exist closely together. These factors increase the risk of interference between communication systems, which degrade the system's performance or, in the worst case, block the radio communication. There are several types of interference that can range from noise to adjacent channel interference from an external system. In this thesis, interference from unwanted spurious signals is considered, known as intermodulation (IM) distortion (IMD) products. The intermodulation products are generated in multicarrier systems that contain nonlinear components. When encountering a nonlinear component, the signals mix, and a wide range of new frequency components are generated, covering the in-band, fundamentals, and harmonics. Most of these spurious signals can be removed by filters. However, spurious signals in close proximity to the fundamental tones, such as the third-order intermodulation (IM_3), cannot be removed by filters as it would also affect the fundamental tones. IMD can originate from both internal and external sources. External sources are in the form of any metal object, e.g., antennas, tower infrastructure, and metal fences. When these metal objects are radiated, they can generate intermodulation that may be radiated back to a communication system.

The probability of interference from intermodulation increases when the frequency spectrum becomes more densely populated and signal power increases. When the frequency spectrum becomes increasingly crowded, with more co-existing communication systems with similar frequency bands, the risk increases that one system generates intermodulation products within the same frequency band as another system's receiver. This issue is more prominent for wideband modulated signals, as the intermodulation product's bandwidth is proportional to the order, e.g., a fifth-order intermodulation (IM_5) product has a bandwidth five times as large as the carrier bandwidth. With an increase in input power, the amplitude of the intermodulation products increases with the order. An increase of 1 dB input power will increase the power of 3 dB and 5 dB for the

third- and fifth-order intermodulation products, respectively. A nonlinear device can be considered linear for certain power conditions, however the addition of higher power may put them into a nonlinear regime. Therefore, this will increase the requirements on highly linear devices. To meet these requirements, accurate models of nonlinear behavior are imperative to understand and mitigate IMD.

Active circuits like amplifiers, mixers, and multipliers exhibit nonlinear behavior due to components such as transistors and diodes, characterized by their current-voltage (IV) and charge-voltage (QV) relationships. In a communication channel, IMD results in spectral regrowth, i.e., there will be spectral leakage into adjacent channels. Spectral masks are applied as a communication standard, defining the allowed ratio of transmitted power in the main channel to the leakage in the adjacent channel. Techniques like feedback [6], predistortion [7], and bias condition selection improve linearity. Various models have been developed to describe the behavior of active circuits, e.g., empirical models that use an equivalent circuit [8] and behavioral modeling [9]. While these models have advanced significantly, development is still ongoing.

Passive devices can produce intermodulation, denoted as passive intermodulation (PIM). Like active devices, PIM occurs when two or more signals interact with a nonlinear element that mixes and generates new spurious signals. PIM has received less attention than IMD in active circuits. One reason is that linear models can typically represent passive structures over a wide range of power levels. The nonlinear sources in passive components are weakly nonlinear, and high power levels are required to generate detectable PIM. Nonlinear sources in passive devices are poorly understood due to less research attention, but also due to the complexity of modeling the nonlinear behavior. The nonlinear sources are typically distributed over the passive component, where several different sources can co-exist, and multiphysics models are often required to predict their behavior. Nevertheless, several physical sources of PIM have been proposed, including constriction resistance [10], electro-thermal induced PIM [11], tunneling [12], and nonlinear conductivity [13]. These types of sources have been studied in several components, e.g., waveguides [12], [14], coaxial connectors [15], transmission lines [16], [17], and antennas [18]. PIM is a prominent issue in the space industry, primarily due to high transmitting power and the susceptibility of receivers. The satellite component's PIM requirements can be as low as -140 dBm [19]. Understanding the underlying mechanism of PIM is imperative for the space industry, as it is costly to re-design components that do not comply with the requirements. For instance, several satellites have experienced PIM in their testing phases, such as FLTSATCOM (US Fleet Communications Satellite), MAR1SAR (US Maritime Satellite), MARECS (European Maritime Satellite), and IS-V (International communication satellite

number V) [20], [21]. This led to launch delays due to the systems' re-design.

This thesis aims to analyze and model IM effects in periodic and surface microstructures. IMD generated in periodic structures is covered in Paper [A], [B], and [C]. Paper [A] investigates an optimal loaded-line phase shifter in terms of linearity and phase-shift/loss. The optimal design regards two design parameters: the unit cell length and the varactor's Q factor. The paper also includes the design process of the loaded-line phase shifter and the nonlinear modeling of varactor-diodes employed in the design. Paper [B] reports on multi-source IM in a tunable loaded-line true-time delay phase shifter, where the varactor-diodes are separated by a quarter-wavelength. In Paper [C], IMD in artificial transmission lines is investigated. PIM generated due to microstructures is presented in Paper [D] and [E]. PIM generated by surface roughness is investigated in Paper [D]. Specifically, it examines a rectangular coaxial transmission line with a replaceable center conductor made of either milled aluminum or aluminum alloy (AlSi10Mg) produced by additive manufacturing (AM). Paper [E] investigates PIM generated in antenna feeding networks in satellite communications. The aluminum feeding networks are anodized with aluminum oxide (Al_2O_3) to increase thermal emissivity and protect them from high temperatures that can lead to thermoelastic movements. The study compares PIM levels produced by different thicknesses of aluminum oxides and non-anodized samples. The surface of the samples is observed and analyzed using scanning electron microscope (SEM) and focused ion beam (FIB) images to develop a nonlinear model.

This thesis has the following structure. Chapter 2 presents the fundamentals of nonlinear distortion. Chapter 3 is dedicated to IM generated in periodic structures. It provides a background and utilization of periodic structures and presents the design of a loaded-line phase shifter. Additionally, it presents the modeling process and the results regarding Paper [A], [B], and [C]. Chapter 4 presents PIM generated in AM structures. It provides background on AM processes and surface roughness models. Furthermore, the test structure, nonlinear model, and results are presented and discussed. Chapter 5 presents the PIM characteristics of anodized antenna feeding networks covered in Paper [E]. The different samples are presented and analyzed using SEM and FIB images. A nonlinear source due to the protective coating and a phenomenological model are proposed. Finally, Chapter 6 concludes this work and discusses future work.

CHAPTER 2

Fundamentals of Nonlinear Distortion

This chapter presents fundamental theory of nonlinear distortion. Section. 2.1 gives a mathematical description of how nonlinear devices generate new frequency content with an emphasis on intermodulation distortion. Section. 2.2 describes nonlinear distortion in passive devices.

2.1 Intermodulation distortion

To describe the generation of IMD products, a nonlinear system with a sinusoidal input signal with frequency f_1 will first be considered. The input signal can be described as $x(t) = A\cos(\omega t)$, where A is the amplitude of the signal, and the output can be obtained with the Taylor expansion

$$y(t) = a_1 x(t) + a_2 x^2(t) + a_3 x^3(t) ... + a_n x^n(t), \tag{2.1}$$

where a_n is the nth-order Taylor coefficient, which is determined around a bias point X_0 and is calculated by

$$a_n = \frac{1}{n!} \frac{d^n y(X_0)}{dx^n}. \tag{2.2}$$

The result of the output signal with the sinusodial signal is

$$y(t) = \frac{1}{2}a_2A^2 + \left(a_1A + \frac{3}{4}a_3A^3\right)\cos(\omega t) + \frac{1}{2}a_2A^2\cos(2\omega t) + \frac{1}{4}a_3A^3\cos(3\omega t) + ... \tag{2.3}$$

The result of (2.3) shows that the single input excitation has generated several signals. Two factors are related to the fundamental frequency, where the factor a_1A is the gain of the signal and $\frac{3}{4}a_3A^3$ represents the compression. The term $\frac{1}{2}a_2A^2$ represents a DC shift. The other two components are the second harmonic and third harmonic that have the amplitude of $\frac{1}{2}a_2A^2$ and $\frac{1}{4}a_3A^3$, respectively.

If the input instead contains two sinusoidal signals with the same amplitude A and frequency components of ω_1 and ω_2, $x(t) = A\cos(\omega_1 t) + A\cos(\omega_2 t)$, then the result of the Taylor expansion is

$$y(t) = a_2A^2 + \left(a_1A + \frac{9}{4}a_3A^3\right)\cos(\omega_{1,2}t) + \frac{1}{2}a_2A^2\cos(2\omega_{1,2}t) + \frac{1}{4}a_3A^3\cos(3\omega_{1,2}t) + a_2A^2\cos(\omega_1 \pm \omega_2) + \frac{3}{4}a_3A^3\cos(2\omega_{1,2} \pm \omega_{2,1}). \tag{2.4}$$

The Taylor expansion with the two-tone excitation also generates a DC shift and harmonics, but also a set of new signals that is a mix of the frequency components ω_1 and ω_2. These new signals are the intermodulation products. The term $a_2A^2\cos(\omega_1 \pm \omega_2)$ is the second order intermodulation (IM_2) product, and the term $\frac{3}{4}a_3A^3\cos(2\omega_{1,2} \pm \omega_{2,1})$ is the third order intermodulation product. The frequency of the intermodulation products can be calculated as $f_{IM} = |mf_1 \pm nf_2|$, where f_1 and f_2 are the two fundamental frequencies, and m and n are integers that give the intermodulation order $N = m + n$. The two-tone frequency spectrum of order 3 is presented in Fig. 2.1. It is clear from the figure, that the frequency components at the baseband and the harmonics can be removed by filters. The frequency content in close proximity to the fundamental tones of f_1 and f_2 cannot be filtered out as it will affect the fundamental tones as well. The IM_3 product is closest to the fundamental tones and it is the IMD product that is often causing the greatest problems. The amplitude of the IMD products is reducing with increasing order, and the IM_3 has the largest amplitude of the uneven IMD products. Due to its amplitude and its close proximity to the fundamental tones, the IM_3 is generally of main

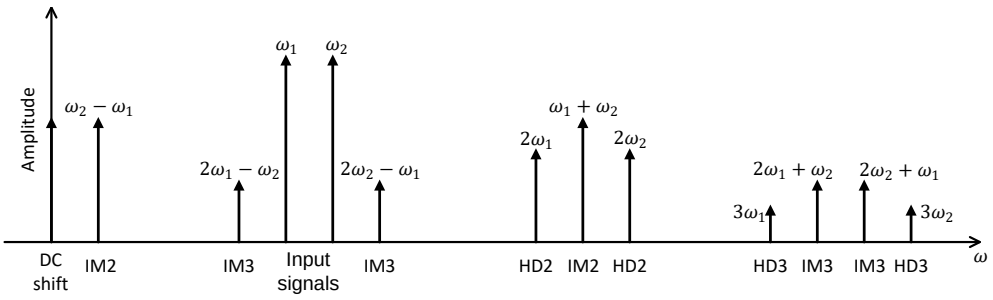

Figure 2.1. The two-tone frequency spectrum illustrated to the third-order, where the two fundamental tones have the frequency of f_1 and f_2.

interest when studying a nonlinear system.

The relationship between output and input power is of interest when studying a nonlinear system. Fig. 2.2 depicts the output power as a function of input power for one of the fundamental signals and one of the IM_3 products. At small input power, the fundamental output power increases by 1 dB when the input power is increased by 1 dB, resulting in a slope of 1 dB/dB. The slope for a higher-order signal is proportional to the order of the signal. Therefore, a IM_3 product has a slope of 3 dB/dB and a IM_5 product has a slope of 5 dB/dB. This linear relationship stops at large input signals due to compression. A metric utilized to know when a device goes into compression is the 1-dB compression point (P1dB), which is defined as when the output power decreases by 1 dB compared to an extrapolated line of its linear relationship at small input power. To characterize a device's linearity, the linear relationship is extrapolated for both the fundamental tone and the IM_3 product, and the intersection of these two lines is called the third-order intercept point (IP_3). The intercept point will correspond to an input power (IIP_3) and output power (OIP_3), and a greater value of IIP_3 or OIP_3 indicates a more linear device. Intercept points of higher orders are sometimes employed to characterize the linearity, however, the IP_3 is most commonly utilized.

2.2 Passive intermodulation distortion

Intermodulation distortion is commonly associated with active components that are known to be nonlinear. When intermodulation is generated in a passive component, it is called passive intermodulation (PIM). However, it is the same phenomenon where two or more signals pass through a nonlinear element that produces mixing products of the input signals. Most passive elements are assumed to be linear. However, all passive components have intrinsic weakly nonlinear sources that can generate PIM with large enough input power. PIM

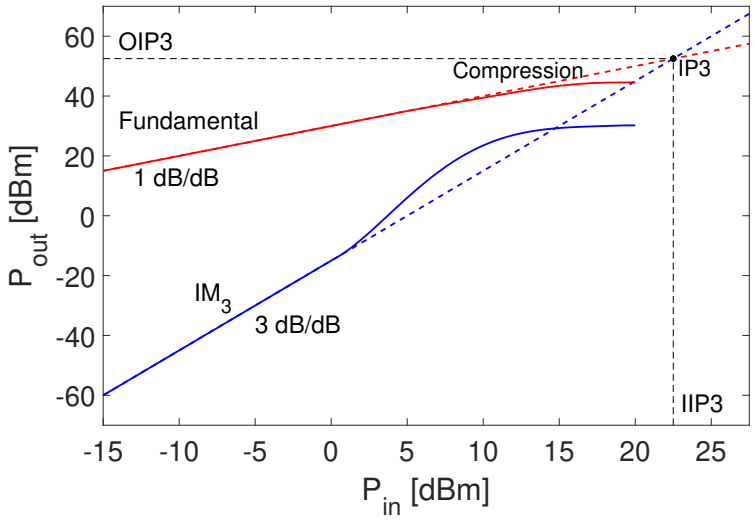

Figure 2.2. The relationship between output and input power of the fundamental tone and the third-order intermodulation. The dashed lines show the extrapolations of the fundamental tone and the third-order intermodulation, and their intersection is the third-order intercept point.

is also an issue in systems with high demands on the dynamic range. In satellite communication systems, PIM is a major problem due to high power levels and sensitive receivers, with PIM requirements of -140 dBm [19]. This complicates the measurement of PIM, as the required dynamic range can reach levels of -200 dBc. Satellites are often composed of various communication systems that both have transmitters and receivers, which create high demands for these to not interfere with each other. The growing demand for high data rates in satellite communication and telecommunications is increasing the input power and the number of signal carriers, making PIM a rising concern.

2.2.1 Sources of passive intermodulation

PIM can be generated both internally and externally. External PIM occurs outside an antenna system and is caused by metallic objects such as metal fences, tower structures, and support systems, which re-radiate PIM to the antenna. Internal PIM is generated within the system itself and can be categorized into several groups, including metallic contacts, materials, electro-thermal effects, geometric effects, and contamination (dust, dirt, and metal flakes).

Contact nonlinearity is one of the most studied PIM sources and can be generated in waveguide flanges [12], coaxial connectors, and wire mesh antennas [22]. The nonlinearity is caused by the surface roughness of the metals, which reduces the contact area. This can lead to several nonlinear effects, such

as tunneling, thermionic emission, or the Poole-Frenkel effect.

Materials can also cause PIM due to nonlinear properties. Ferromagnetic materials, such as nickel and iron, exhibit a nonlinear magnetic hysteresis curve, leading to PIM generation [23]. Ferrimagnetic materials, often used in devices like circulators [24] and isolators [25], also produce PIM. Additionally, superconducting materials are intrinsically nonlinear because of the dependence of the superfluid density on the current density [26]. This type of nonlinearity has been studied and modeled in several components, including resonators [26], filters [27], and transmission lines [28].

The electrical and thermal domains have vastly different time constants. However, if the baseband components have a similar time constant to the thermal domain, then the two domains can interact and generate electro-thermal distortion. PIM generated due to electro-thermal effects has been studied in microstrip lines [16], antennas [29], and attenuators [30].

The geometry of a structure can induce PIM. The effect of bends on PIM in connector-microstrip assemblies [31], superconducting transmission lines [32], and coaxial connectors [33] has been studied and shown to increase PIM. Moreover, many PIM sources are current-dependent, and higher current densities are associated with elevated PIM levels. Therefore, geometries that generate high current densities, such as sharp corners, will increase PIM levels.

The following text presents a more in-depth explanation of some PIM sources.

Metallic contacts

The connection between two metals can generate PIM, which has been studied for several components, e.g., coaxial connectors [15], [34]–[36], waveguide flanges [12], [14], [37], [38], and wire mesh antennas [18], [22], [39], [40]. The contact area between two metals is only a small fraction of the total area due to the surface roughness, as depicted in Fig. 2.3. This creates void regions and contact regions. Metals have a natural insulation layer of oxidation or sulphides, and the thickness of the insulation layer depends on the type of metal. For instance, gold has a thin or no insulation layer, whereas aluminum typically has an oxidation layer of 2-3 nm thickness. Therefore, the contact points between two metals have two types: MIM contact and MM contact. If an insulating layer exists, the MM contact is formed by applying enough contact pressure to break the insulating layer. In [12], the generation of PIM in the metallic contact between waveguide flanges was studied. They employed the surface model from [41] and the result from [42] to model the connection between two metals. The surface model utilizes a statistical approach that distributes asperities (peaks on the surface) over the surface. Fig. 2.4 depicts the topography of the surface model where one surface is modeled as flat, and

the other is modeled as a rough surface with spherical asperities. The asperities are assumed to have the same radius of curvature r, z is the asperity height and is assumed to have a Gaussian distribution, d is the distance between the mean of asperity heights and the flat surface, and l is the interference distance (the distance of the asperity that penetrates the flat surface).

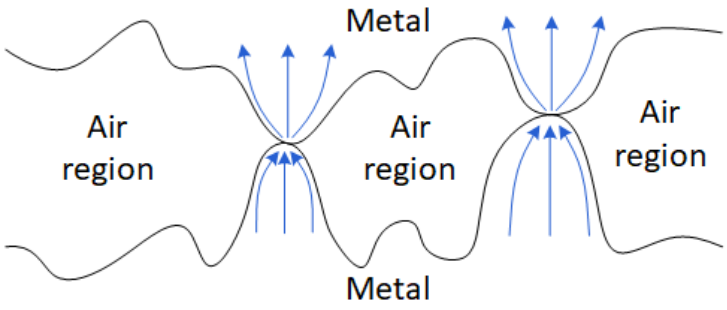

Figure 2.3. Illustration of the rough surface contact between two metals. The blue lines represent the constriction current due to the limited contact area.

Several nonlinear phenomenons that generate PIM in metallic contacts have been proposed, and the type of nonlinearity depends on whether there is a void region, a MIM contact, or a MM contact. In the void region, the nonlinearity is associated with field emission or gas breakdown (corona) [12]. MIM contact zones can generate PIM from tunneling, thermionic emission, or the Poole-Frenkel effect. In the MM contact zones, the PIM is generated by constriction resistance, which is related to the change in the direction of the current lines in the area between the MM contact.

The insulating layer in a MIM contact functions as a potential barrier, where a current can flow through due to the tunneling effect. For a wave to propagate through the insulating layer depends on the amplitude of the wave function and the energy of the barrier, i.e., the width of the barrier. The wave will decay exponentially through the barrier and if the amplitude of the wave is large enough, some of its energy will decay to the other side. A model for the tunneling effect in MIM contacts is described in [43], which gives an I-V relation for the tunneling current. The model has been employed in [44] and [12] to demonstrate the generation of PIM in MIM contacts.

Electro-thermal effects

PIM can be generated in lossy passive components through coupling between the electrical and thermal domains. The electro-thermal distortion was studied for lossy passive components in [11], [30]. The electrical and thermal domains have time constants that differentiate by several order of magnitude. However,

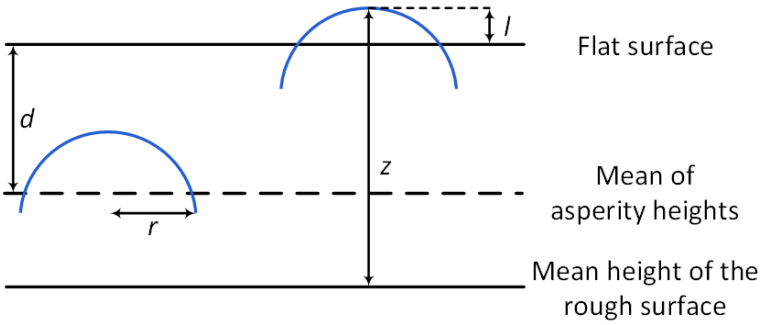

Figure 2.4. The topography of the surface model employed in [12].

an interaction between the two domains is possible if the modulated radio-frequency (RF) signal has baseband components that have a period comparable to the thermal time constant. This creates a strong coupling between the electrical and thermal domains and results in an electro-thermal distortion. The coupling is induced by self-heating in resistive materials when high power RF signals are applied. If two or more RF signals are applied, a time varying signal envelope will exist. If the power envelope contains the baseband frequency components, the resistance will vary from periodic heating and cooling. This will effectively function as a passive mixer that will upconvert the envelope frequencies, and result in PIM.

To understand the coupling between the electrical and thermal domains, we begin with the resistance of a metal. The metal has an electrical resistance and a thermally-based resistance [45]. From the thermally-based resistance, a specific resistance ρ_e can be modeled that also includes the temperature dependence

$$\rho_e(T) = \rho_{e0}(1 + \alpha T + \beta T^2 + ...), \tag{2.5}$$

where T is the temperature, ρ_{e0} is the static resistivity and α and β are temperature coefficients of resistance. The coupling of the thermal and electrical domain is generated from dissipated electrical power, which depends on the current density and the specific resistance of the material. The dissipated electrical power is called self-heating and is expressed as

$$Q = J^2 \rho_e, \tag{2.6}$$

where J is the current density. The heat generated by self-heating is then transferred in the material, which can be described with the heat conduction equation

$$\nabla \cdot \left(\frac{\nabla T}{R_{th}} \right) - C_v \frac{\partial T}{\partial t} = Q, \tag{2.7}$$

where R_{th} is the thermal resistance and C_v is the thermal capacity at constant volume. The thermal resistance is the ability of a material to resist the flow of heat through it. The thermal capacity represents the material's capacity to store heat and its ability to conduct heat to its surroundings. The nonlinear system describing the electrical and thermal coupling is found by substituting 2.5 and 2.6 into 2.7, and is described as follows

$$\nabla \cdot \left(\frac{\nabla T}{R_{th}} \right) - C_v \frac{\partial T}{\partial t} = J^2 \rho_{e0} (1 + \alpha T + \beta T^2 + ...). \tag{2.8}$$

The nonlinear electro-thermal process has a static and a dynamic part with the respective power signals P_s and P_d, dissipating through the static and dynamic resistance R_s and R_d, respectively. The total power dissipated over the static and dynamic resistance is converted to the heat signal $Q\,(P_s + P_d)$. The thermal resistance and capacitance constitute a low pass filter, and the heat signal will be filtered by this thermal response. Fig. 2.5a shows the spectrum of a two-tone signal that is applied to a restive element. The two-tone signal will have a time-varying signal envelope. The instantaneous power of the signal envelope will vary periodically at the beat frequency of the two-tone signal, and Fig. 2.5b depicts the sum and difference frequency components. This will, in turn, create periodic cooling and heating at baseband frequencies as long as the beat frequency is within the bandwidth of the lowpass filter, as depicted in Fig. 2.5c. The resistance will also vary periodically. This periodic oscillation will result in a passive mixer generating IMD by up-converting the envelope frequencies to RF frequencies, as shown in Fig. 2.5d.

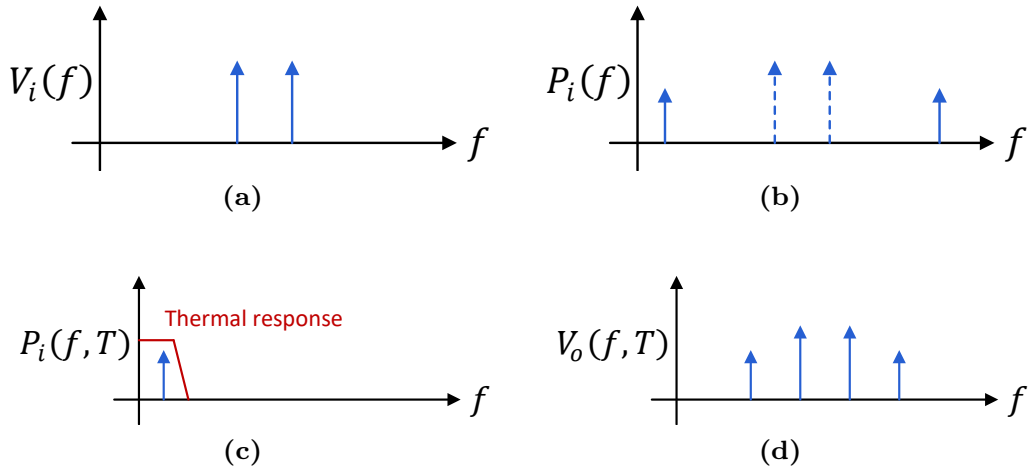

Figure 2.5. Electro-thermal distortion generated in a resistive element by a two-tone excitation. (a) The spectrum of the input voltages. (b) The input power spectrum resulting from the two-tone spectrum. (c) The baseband component of the input spectrum that is within the thermal response. (d) The resulting output spectrum generated from electro-thermal mixing.

CHAPTER 3

Intermodulation in Periodic structures

This chapter explores IMD generated in periodic structures, more specifically, loaded-line phase shifters. Firstly, the basics of periodic structures are presented in Section 3.1. In Section 3.2, the design of loaded-line phase shifters is explained. Section 3.3 describes the modeling of the varactor-diodes employed in the phase shifters. Then, the realized phase shifters are presented in Section 3.4. A two-tone measurement is presented in Section 3.5. The phase shifter performance and nonlinear behavior are presented in Section 3.6 and Section 3.7, respectively. Lastly, Section 3.8 examines whether there is an optimum design of loaded-line phase shifters with respect to phase-shift/loss and linearity.

3.1 Basics of periodic structures

Periodic structures consist of transmission lines or waveguides periodically loaded with reactive elements, such as discontinuities or lumped components. They exhibit passband-stopband response and can support waves with phase velocities less than the speed of light [46]. These characteristics are employed to modify electromagnetic waves, e.g., filters [46], traveling-wave tubes [47], phase shifters [48], and steerable antennas [49]. Fig. 3.1 illustrates two cases of a transmission line with shunt capacitive loading and series inductive loading.

In a smooth transmission line, it is not possible to change the phase velocity by modifying the geometry. The phase velocity in a transmission line is

$$v_p = \frac{1}{\sqrt{L_t C_t}}, \tag{3.1}$$

where L_t is the series inductance per unit cell length and C_t is the shunt capacitance per unit cell length. Suppose the geometry of the smooth transmission line is changed to increase the shunt capacitance per unit cell length. In that case, it will decrease series inductance per unit cell length, and the phase velocity will stay consistent. The addition of periodic reactive elements enables a change in the phase velocity by increasing the propagation constant β. An unloaded transmission line with low impedance is employed for the transmission line with series inductance in Fig. 3.1a. The loading inductance increases the transmission line's characteristic impedance to its desired value. The opposite happens for the transmission line with shunt capacitive loading in Fig. 3.1b. An unloaded high-impedance transmission line is employed, and the shunt capacitance decreases the characteristic impedance. This type of shunt capacitive loading will be employed in the following sections.

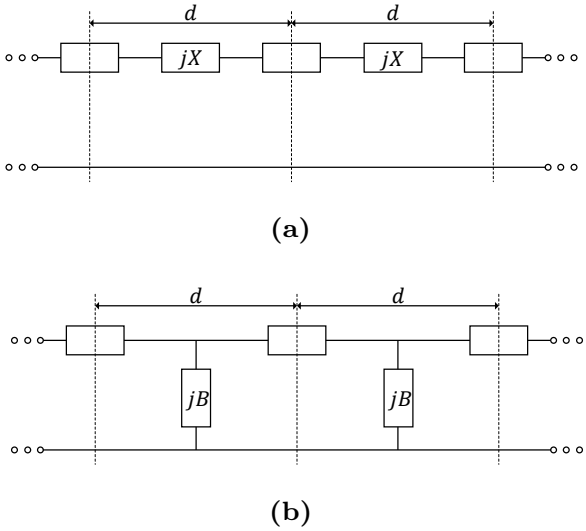

Figure 3.1. Illustration of a periodically loaded transmission line with (a) series inductance loading, and (b) shunt capacitive loading.

3.2 Design of a loaded-line phase shifter

A tunable phase shifter has the purpose of modifying the phase shift or the group delay of a transmitted signal with the smallest possible loss. There are several implementations of tunable phase shifters, e.g., switched-line phase shifters, hybrid-coupled reflection-type phase shifters [50]–[52] and loaded-line phase-shifters [48], [53]. Only the two latter may be used for analog tuning.

Tuning mechanisms include mechanical, magnetic, and electronic. For electronic tuning, semiconductor varactor diodes are typically employed due to ease of manufacturing, compatibility with circuits, and good performance [48], [54]. In the following text, the design basics of a loaded-line phase shifter and the different performance metrics are presented.

A loaded-line phase shifter is composed of a transmission line periodically loaded by shunt-susceptances. Fig 3.2 illustrates a loaded-line phase shifter with N number of T-unit cells (UC), where each UC is composed of two transmission lines of length $d/2$, and with a shunt-loaded varactor-diode in between. The unloaded transmission line is characterized by its unloaded electrical length θ_0 and impedance Z_0. The varactor-diodes function as the loading and they are reversed biased, meaning that they act as a nonlinear capacitor and share similarities with the design in Fig. 3.1b, where we wanted a high-impedance unloaded transmission line. The varactor-diode has a voltage-controlled capacitance $C_V(V_R)$, where V_R is the reversed bias voltage. The transmission line has an inductance per unit cell length L_t and a capacitance per unit cell length C_t. The transmission line and the varactor-diode can be modeled as an artificial transmission line with an effective electrical length θ_e and characteristic impedance Z_e. The unit cell's effective characteristic impedance can be calculated with

$$Z_e = \sqrt{\frac{L_t}{C_t + C_V(V_R)/d}} = \sqrt{\frac{L_t}{C_t}} \times \frac{1}{\sqrt{1 + IF(V_R)}} = Z_0 \frac{1}{\sqrt{1 + IF(V_R)}} \quad (3.2)$$

where

$$I_F = \frac{C_V(V_R)}{C_t d} \quad (3.3)$$

is known as the inclusion factor. Under the condition $C_V \gg C_t d$, (3.2) can be simplified to

$$Z_e = \sqrt{\frac{L}{C_V(V_R)}}, \quad (3.4)$$

where $L = L_t d$ is the inductance per unit cell. Equation (3.2) is valid as long as the frequency is far below the Bragg frequency f_B, which is defined as the frequency where the period d between two varactor-diodes is equal to half of the guided wavelength λ_g. In terms of the loaded-line phase shifter parameters, the Bragg frequency [55] is

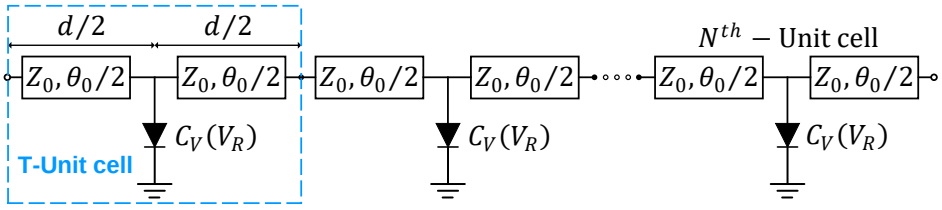

Figure 3.2. Illustration of the periodic loaded-line phase shifter with N number of T-unit cells.

$$f_B = \frac{1}{\pi d\sqrt{L_t C_t(1 + I_F(V_R))}}. \tag{3.5}$$

To achieve a large phase shift, both L and C_V shall be large, and to obtain a large L the unloaded transmission line needs to be of high-impedance. The capacitance $C_V(V_R)$ changes with the bias condition, and only one bias point will achieve a perfect match with the system impedance. Therefore, the phase shifter will be mismatched when tuning the phase and there will be two extreme bias points of $V_{\min}$ and $V_{\max}$. When designing a phase shifter, the differential phase shift $\Delta\phi$ is of interest, which is defined as the phase shift between the two extreme bias points and is expressed as follows

$$\Delta\phi = \beta(V_{\min}) - \beta(V_{\max}). \tag{3.6}$$

In reality, an increased phase shift normally comes with increased attenuation due to mismatch and dissipation. Therefore, phase shifters are also evaluated for a phase-shift/loss figure of merit (FOM). The FOM is expressed as

$$F_{\Delta\phi} = \frac{\Delta\phi_{\text{degree}}}{L_{\text{dB}}}, \tag{3.7}$$

where L_{dB} is the total loss in the phase shifter. The total loss will vary depending on the applied bias, and in this work, L_{dB} is defined as the total loss for the bias state with the most significant loss.

3.3 Varactor-diode modeling

To correctly evaluate the performance of a loaded-line phase shifter in simulation, an accurate varactor model has to be implemented, especially to describe the nonlinear behavior of the phase shifter. The varactor-diode can be represented by an equivalent circuit model [see Fig. 3.3] that is composed of a series inductance (L_s), a series resistance (R_s), a parallel capacitance (C_p),

and the variable junction capacitance (C_j). The variable junction capacitance is the nonlinear component in the model introduced due to the reversed bias of the varactor. The impedance of the varactor-diode can be written as

$$Z(V_R) = R_s + j\left(\omega L_s - \frac{1}{\omega C_V(V_R)}\right), \tag{3.8}$$

where $C_V(V_R) = C_j(V_R) + C_p$. The model of C_j depends on the doping profile of the p-n junction. In the case of a uniformly doped and linearly graded junction, the variable junction capacitance is typically modeled as

$$C_j(V_R) = \frac{C_{j0}\phi^n}{(\phi + V_R)^n}, \tag{3.9}$$

where C_{j0} is the zero bias junction capacitance of the diode, ϕ is the built-in potential, and n is the grading coefficient [56]. This model has shown good accuracy for uniform varactor-diodes. However, when the doping profile is highly nonuniform, (3.9) may not accurately describe the C-V characteristics of the varactor-diode. Instead, a piecewise model or a capacitive polynomial series may be used. The C-V characteristics as a polynomial series can be expressed as

$$C_j(V_R) = C_0 + C_1 V_R + C_2 V_R^2 + ... + C_n V_R^n, \tag{3.10}$$

where C_n is the polynomial coefficient of the n^{th}-order.

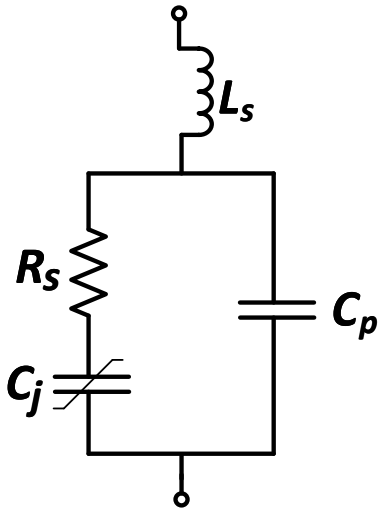

Figure 3.3. Equivalent circuit model of the reversed bias varactor-diode.

3.3.1 Extraction of varactor-diode model parameters

The model parameters in Fig. 3.3 can be extracted by measuring the S-parameters of the varactor-diode and using (3.8). The modeled bias range of the varactor should be larger than the bias range of the phase shifter to properly model the nonlinear behavior because it has to cover the RF voltage swing, which includes both DC and RF voltage. Due to the T-network configuration of the measured two-port, the varactor's impedance is equal to Z_{12}. From (3.8) we can see that R_s is given by $\mathrm{Re}(Z_{12})$, and that $\mathrm{Im}(Z_{12})$ contains both L_s and $C_V(V_R)$. However, at low frequencies, the parasitic inductance is small, which makes it possible to estimate both values from the $\mathrm{Im}(Z_{12})$.

This method was utilized in Paper [A] to extract the model parameters of the hyperabrupt varactor SMV1233-079LF [57]. To obtain Z_{12}, the two-port network's S-parameters were measured, and the effects of the transmission lines were de-embedded. Then, Z_{12} was calculated from the de-embedded S-parameters. The S-parameters were measured from DC to 5 GHz with a bias voltage ranging from 0.3 V to -12 V. The C-V characteristic was obtained from $\mathrm{Im}(Z_{12})$ at 200 MHz. A lower frequency would be preferred due to a smaller influence of the parasitic inductance, but the VNA calibration had limited precision at low frequency. A polynomial curve fitting of the measured C-V characteristics extracted the polynomial coefficients, which include both C_j and C_p. The two models of C_j presented in (3.9) and (3.10) were evaluated for the varactor SMV1233-079LF. The parameters in (3.9) were obtained from the datasheet combined with optimization to fit the measured C-V characteristics as best as possible. Fig. 3.4 depicts a comparison of the C-V characteristics and the relative error between the measured data and the two models. The measured data and polynomial model have excellent agreement with a maximum relative error of 2.4%. In contrast, the measured data and the model in (3.9) show large discrepancies, where the maximum relative error is 9.9%. Showing that the polynomial model is a better fit for the highly nonuniform varactor-diode.

The series inductance was determined from the frequency-dependency of the measured C-V. A least-square fit of the imaginary part of (3.8) versus frequency for each bias voltage was utilized to determine L_s. The extracted value was $L_s = 1.51$ nH. The datasheet value is 0.7 nH and it is expected that the larger extracted value is from the pads connecting the varactor. At higher frequencies, L_s has a greater influence on $\mathrm{Im}(Z_{12})$ and to adequately model the nonlinear behavior this influence should be modeled to at least the frequency of the third harmonic. Fig. 3.5a depicts the $\mathrm{Im}(Z_{12})$ for the second and third harmonic, corresponding to 3 GHz and 4.5 GHz, respectively.

Lastly, the series resistance was found from $\mathrm{Re}(Z_{12})$. The measured resistance versus bias is depicted in Fig. 3.5b. At low frequency, the measurement is noisy,

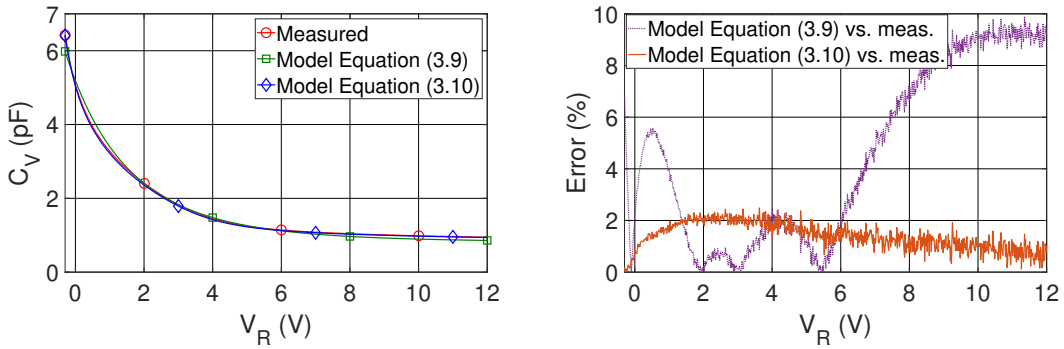

(a) **(b)**

Figure 3.4. A comparison of measured data, the varactor-diode model in (3.9), and the varactor-diode model in (3.10) for the SMV1233-079LF varactor-diode's (a) C-V characteristics, and (b) the relative error between the measured data and the two models.

and at higher frequency the resistance increases due to the skin effect and distributed effects in the varactor. The resistance was obtained by finding the average for each frequency and then calculating the average of those averages. The frequencies were limited to 1.5 GHz to 2.5 GHz to avoid the measurement noise and the skin effect and distributed effects at high frequency. The obtained R_s was 1.49 Ω, which is close to the datasheet value of 1.2 Ω.

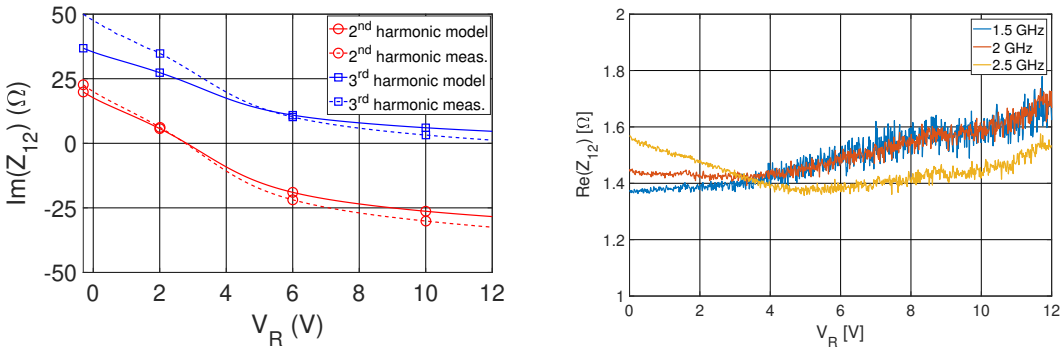

(a) **(b)**

Figure 3.5. (a) Modeled and measured Im(Z_{12}) for the second harmonic (3 GHz) and third harmonic (4.5 GHz). (b) Real part of the measured varactor impedance.

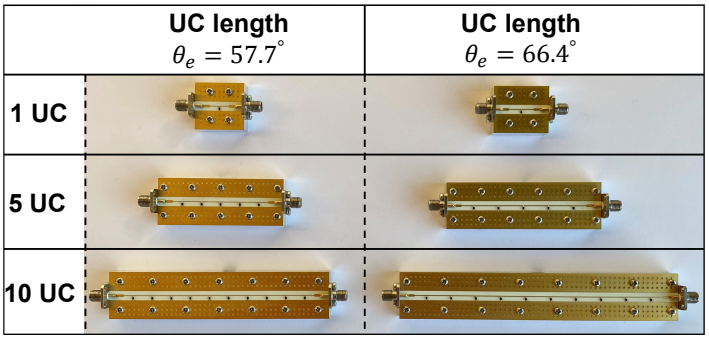

Figure 3.6. The fabricated phase shifters in Paper [A].

3.4 Realized loaded-line phase shifters

In this section, the realized loaded-line phase shifters are presented. All phase shifters are implemented in a grounded coplanar waveguide (CPWG) configuration with substrate Rogers RO4350 with the relative permittivity $\epsilon_r = 3.66$ and height 0.508 mm. The design frequency is 1.5 GHz and $Z_e = 50\ \Omega$. The main difference is the type of varactor-diode. The phase shifters in Paper [A] are designed with the hyperabrupt SMV1233-079LF varactor-diode. Paper [B] and Paper [C] employ a BAT63 silicon Schottky diode [58].

Fig. 3.6 depicts six loaded-line phase shifters realized in Paper [A]. The differences are the unit cell length and the number of unit cells, which are 1, 5, and 10 unit cells. An illustration of a unit cell is shown in Fig. 3.7a, composed of a high-impedance transmission line, a shunt-varactor, and thru lines at the input and output. A Thru-Reflect-Line (TRL) [59] was designed to de-embed the effect of the coaxial connector and the thru line. The phase shifters' had the bias tuning range from $V_R = 3$ V to $V_R = 8$ V. A lower V_R increased losses, and a higher V_R only slightly increased $\Delta\phi$. In Fig. 3.7b, θ_e and Z_e are presented for the two unit cells at the center of the tuning range $V_R = 5.5$ V. The shorter unit cell has a $\theta_e = 57.7^\circ$ at 1.5 GHz and a $Z_0 = 100\ \Omega$. The longer unit cell has a $\theta_e = 66.4^\circ$ at 1.5 GHz and a $Z_0 = 90\ \Omega$. A final comment about the design, only one varactor-diode for each unit cell is connected to one of the ground planes compared to Paper [B] and Paper [C], which had two varactor-diodes for each unit cell. This would increase the loading. However, to maintain $Z_e = 50\ \Omega$, the unloaded impedance needs to be increased, resulting in a too narrow transmission line.

Paper [B] and Paper [C] utilize the same fabricated designs, but the model was further developed in Paper [C]. Three phase shifters were fabricated that differ in the number of unit cells, which were 1, 4, and 7 unit cells, as depicted in Fig. 3.8a. The unit cell is designed with a $\theta_e = 90^\circ$ at 1.5 GHz and $Z_0 = 76\ \Omega$.

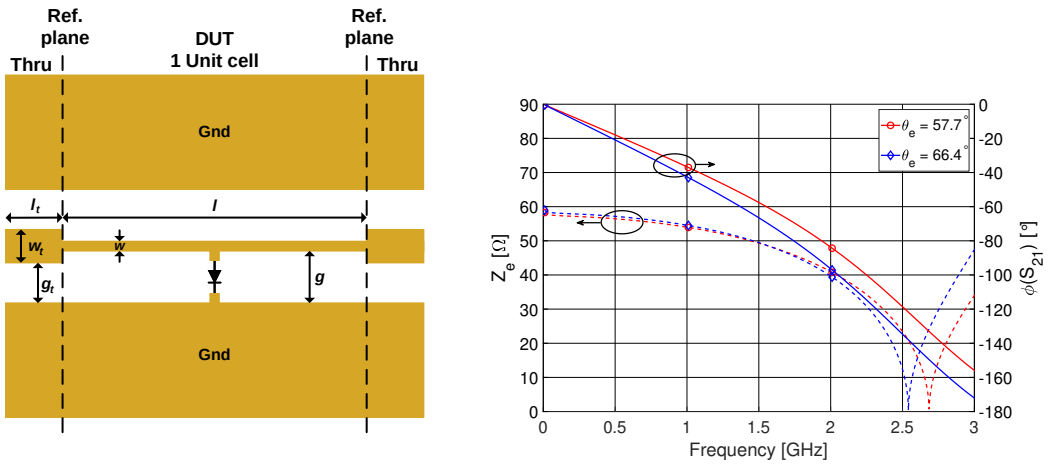

(a) (b)

Figure 3.7. (a) Illustration of the phase shifter with a single unit cell and the thru lines. The dimensions of the unit cell with $\theta_e = 57.7°$ are $l = 10.1$ mm, $w = 0.31$ mm, and $g = 2.34$ mm. The dimensions of the unit cell with $\theta_e = 66.4°$ are $l = 13.14$ mm, $w = 0.4$ mm, and $g = 2.29$ mm. The dimensions of the thru line are $l_t = 8$ mm, $w_t = 1.183$ mm, and $g_t = 1.9$ mm. (b) The simulated Z_e and θ_e for the two unit cells.

The unit cell is symmetric with two varactor-diodes that are connected to the top and bottom ground plane. The C-V characteristic of the BAT63 Schottky diode is shown in Fig. 3.8b. At 1 MHz the diode's junction capacitance C_{j0} is 0.75 pF. The reversed bias applied to the phase shifters was varied from 0.3 V to 3 V. The lower and upper limit was selected because at a $V_R < 0.3$ V losses were too high, and at $V_R > 3$ V the tuning saturated.

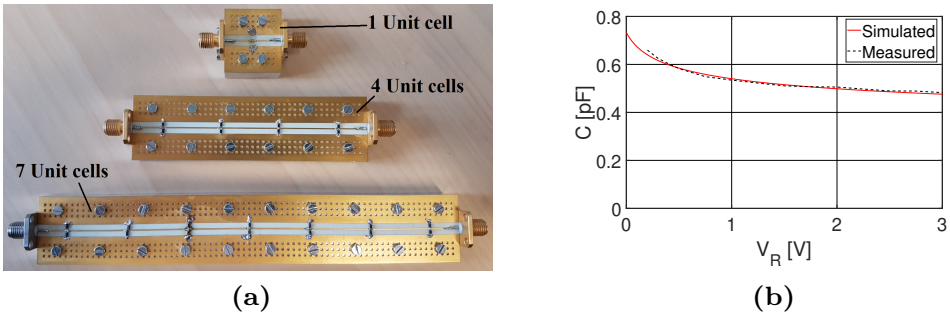

(a) (b)

Figure 3.8. (a) Realized phase shifters with the BAT63 Schottky varactor-diode employed. (b) Measured and simulated C-V characteristics of the BAT63 Schottky varactor-diode.

3.5 Two-tone measurement

This section describes the two-tone measurement in Paper [A]. A two-tone test is a typical measurement setup to measure IMD in a device, which utilizes two fundamental signals that are combined and fed into a DUT. The resulting IMD is typically measured using a spectrum analyzer. The two fundamental tones had frequencies of 1.5 GHz and 1.55 GHz, generating the lower-band and upper-band IM_3 products at 1.45 GHz. and 1.6 GHz, respectively. The measurement setup in Paper [A] is shown in Fig. 3.9. In this setup, a Keysight PNA-X N5247B is employed for both signal generation and IMD measurement. Two sources generate the two fundamental signals internally of the PNA, and the two signals eject two different ports. Each port is connected to a low-pass filter (DC-2250 MHz) that is connected to an isolator. The low-pass filter suppresses any higher-order harmonics generated in signal sources. The isolator suppresses leakage between the channels and reflections from the DUT, which can otherwise result in generation of IMD in the sources. After the isolator, the two signals are combined in a 6-dB combiner and fed into the DUT. The DUT is then connected to a third PNA port with the swept IMD measurement type enabled, which measures the generated IMD. The measurement setup's noise floor was measured to -115 dBm, and the residual intermodulation was below this level.

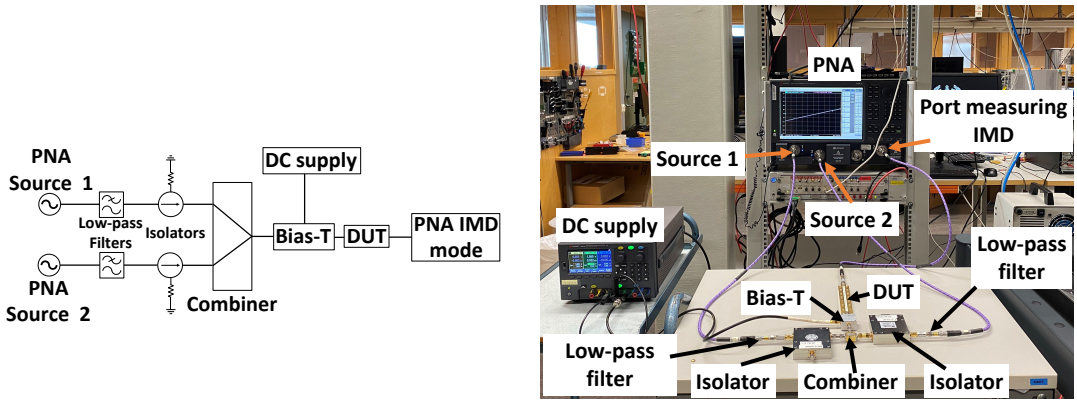

(a) (b)

Figure 3.9. (a) Illustration of the two-tone measurement setup for forward IM. The fundamental signals are generated by the PNA internally, and the IM is measured with the same PNA at a third port in swept IMD measurement mode. (b) The measurement setup.

3.6 Phase shifter performance

The performance metrics of the phase shifters in terms of the differential phase shift, FOM, insertion loss (IL), phase shift, and return loss (RL) were obtained from the S-parameters. The S-parameters were measured using an N5222A PNA Microwave Network Analyzer, while simulations were conducted using Advanced Design System (ADS). The results evaluate performance and validate the varactor-diode model.

The phase shifters in Paper [A] have unit cell lengths of 57.7° and 66.4°. Their results show similarities, and the following figures present the results of the shorter unit cell. Fig. 3.10 depicts the IL and phase shift for the phase shifters with a unit cell length of 57.7°. For all phase shifters, the measured data agree well with the results from the model. The measured IL for the phase shifters with 5 and 10 unit cells are larger than the simulated IL, which may be attributed to higher metal loss due to deviating conductivity and higher surface roughness in the fabricated phase shifters. There is also some deviation in phase shift after 2 GHz between simulated and measured results, where the phase shifter becomes more dispersive. Fig. 3.11a depicts $\Delta\phi$ between $V_{\mathrm{Rmin}} = 3$ V and $V_{\mathrm{Rmax}} = 8$ V. Fig. 3.11b depicts the FOM over frequency for V_{Rmax}. The measured result has unrealistic values at low frequency due to limited precision in VNA calibration, which greatly impacts the low IL. The measured FOM is lower than the simulated FOM after 0.5 GHz because of the larger measured IL. Table 3.1 compares the results of all phase shifters, and it shows that the measured $\Delta\phi$ at 1.5 GHz is greater for the phase shifters with the longer unit cell length of 66.4°. This is to some extent surprising as the phase shift is expected to increase as the varactor inclusion factor increases. However, a longer unit cell is also more dispersive and the dispersion accelerates the phase shift. The FOM is larger for the phase shifters with the shorter unit cell length of 57.7° due to lower IL. Consequently, the phase shifters with the shorter unit cell present the best performance in terms of both FOM and linearity.

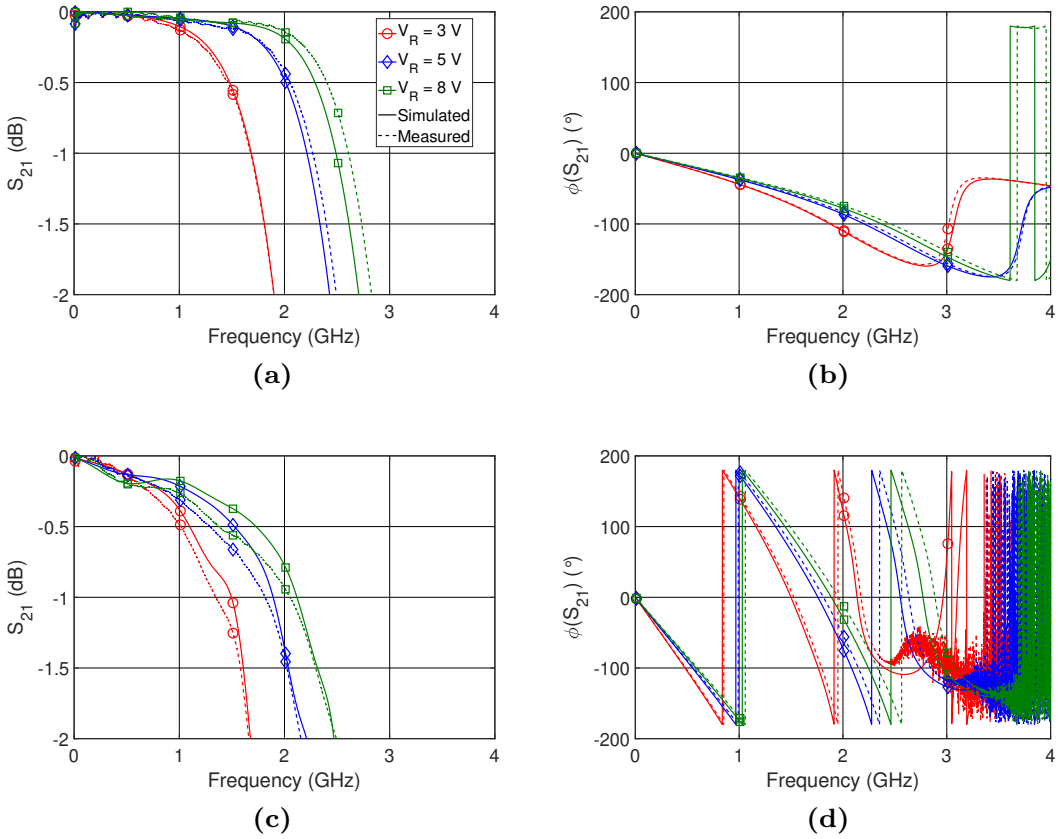

Figure 3.10. The simulated and measured S-parameters for the phase shifter with a unit cell length of 57.7°. The results for 1 unit cell (a) IL, and (b) phase shift. The results for 5 unit cells (a) IL, and (b) phase shift.

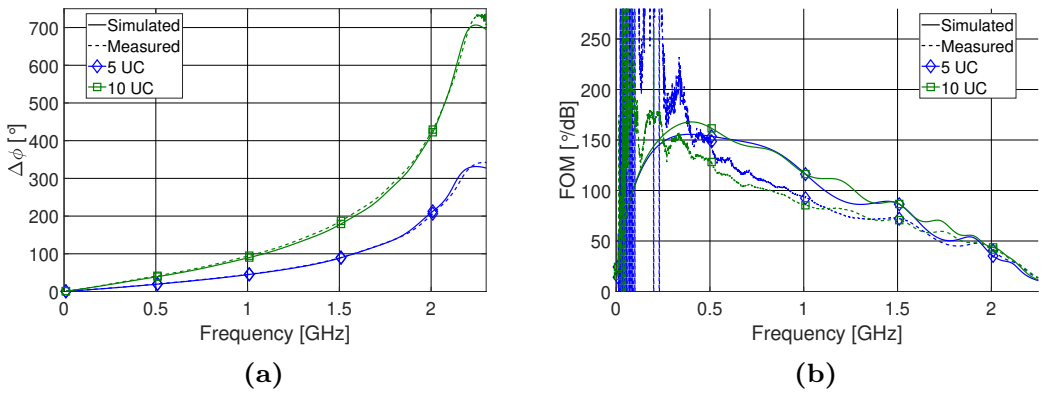

Figure 3.11. (a) The differential phase shift between $V_{\mathrm{Rmin}} = 3$ V and $V_{\mathrm{Rmax}} = 8$ V for and (b) FOM for phase shifters with a unit cell length of 57.7°.

Table 3.1. Summary of the measured $\Delta\phi$, FOM, IL, RL at 1.5 GHz, and the $IIP3$ at 1.6 GHz for all fabricated phase shifters in Paper [A]. The IL is presented when $V_{\mathrm{Rmin}} = 3$ V, which gives the largest IL. The RL is selected at $V_R = 5$ V. The $IIP3$ is selected at $V_R = 5.5$ V.

Unit cell length $\theta_e = 57.7°$										
UC	**$\Delta\phi$ [°]**		**FOM [°/dB]**		**IL [dB]**		**RL [dB]**		**IIP3 [dBm]**	
	Sim.	Meas.	Sim.	Meas.	Sim.	Meas.	Sim.	Meas.	Sim.	Meas.
1	18.0	18.9	33.3	33.2	0.54	0.57	29.1	32.9	34.5	35.1
5	88.3	88.9	87.4	72.3	1.01	1.23	28.9	46.4	27.7	28.7
10	177	185	87.6	70.8	2.02	2.61	30.9	33.6	25.5	26.2
Unit cell length $\theta_e = 66.4°$										
UC	**$\Delta\phi$ [°]**		**FOM [°/dB]**		**IL [dB]**		**RL [dB]**		**IIP3 [dBm]**	
	Sim.	Meas.	Sim.	Meas.	Sim.	Meas.	Sim.	Meas.	Sim.	Meas.
1	18.7	19.9	32.8	30.6	0.57	0.65	29.2	32.1	34.2	34.8
5	94.8	97.7	72.9	64.7	1.30	1.51	37.9	43.0	27.0	28.4
10	188	195	77.4	69.1	2.43	2.82	32.9	36.8	24.2	26.0

Paper [B] and Paper [C] employ the same design, however, the model was further developed and improved in Paper [C]. Therefore, the following results are from Paper [C]. The measured and simulated IL and phase shift are shown in Fig. 3.12 for the phase shifter with 4 unit cells. The simulated and measured results have good agreement from DC to the design frequency. At higher frequencies, there are some discrepancies that are probably the result of distributed effects that the model does not capture.

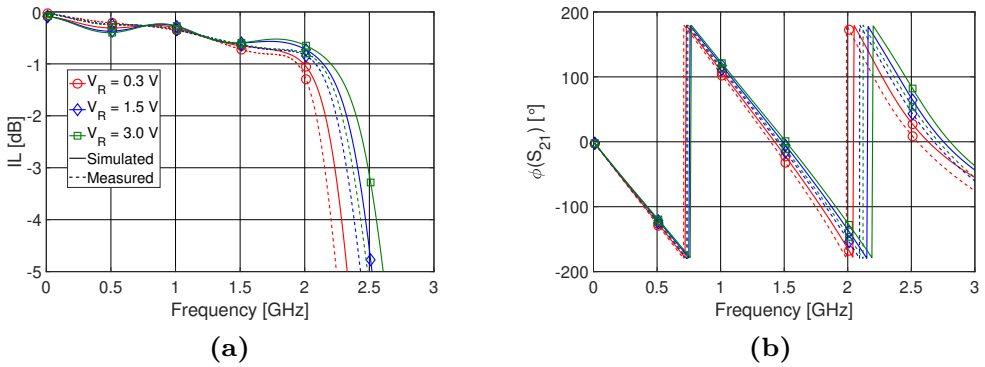

(a) **(b)**

Figure 3.12. The simulated and measured S-parameters for the phase shifter in Paper [C]. The results for the phase shifter with 4 unit cells (a) IL and (b) phase shift.

3.7 Nonlinear behavior

Accurately modeling IMD due to a varactor requires capturing parasitic elements, especially inductance. Also, accounting for impedance at the input and output of the DUT is imperative. Ideally, the measurement system maintains a 50 Ω impedance to the DUT across all frequencies and biases, but this is rarely achieved. Therefore, the S-parameters of the measurement system and the thru lines are included in the simulation, as depicted in Fig. 3.13a. The improved agreement between measured and simulated IMD is shown in Fig. 3.13b.

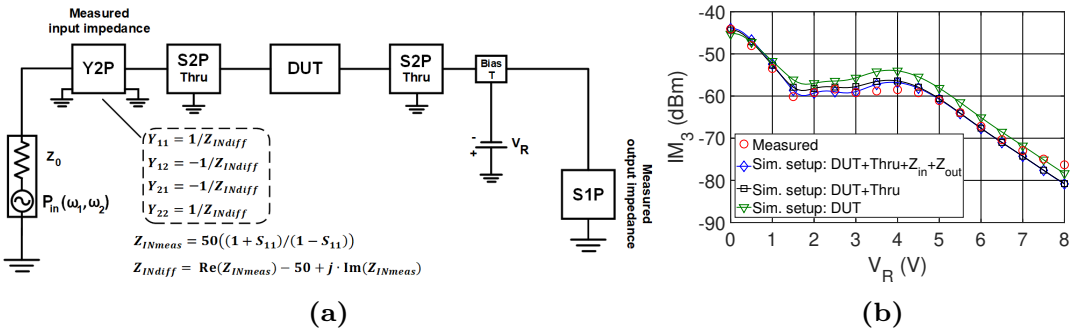

Figure 3.13. (a) Illustration of the simulation setup in ADS, and (b) improved IM_3 agreement. In the simulation setup, the measured input impedance of the measurement setup is incorporated as an equation-based admittance (Y2P) component in ADS, along with the S2P file of the thru. On the output side, the setup includes the measured output impedance represented as an S1P file, the biasing network, and the S2P file of the thru. The simulated system impedance is $Z_0 = 50\ \Omega$.

In Paper [A], IM_3 was simulated and measured for input power from -18 dBm to 1.6 dBm. Table 3.1 compares phase shifter linearity using $IIP3$, obtained by extrapolating input power and IM_3. It shows that more unit cells increase nonlinearity, as $IIP3$ decreases. Additionally, the shorter unit cell improved linearity. Fig.3.14 shows IM_3 as a function of V_R with $P_{\text{in}} = 1.6$ dBm. The model accurately predicts nonlinear behavior, especially for phase shifters with a single unit cell. There are some discrepancies between the model and the measurements for the phase shifters with 5 and 10 unit cells in the range of 3 V to 5 V. At $V_R = 0$ V, IM_3 peaks for a single unit cell but reaches a minimum for phase shifters with 5 and 10 unit cells. The minimum is attributed to suppression of the input signals, the measured IL > 70 dB at 1.5 GHz when $V_R = 0$ V. For a single unit cell with $\theta_e = 57.7°$, the measured IL is 12.9 dB. Lastly, Fig. 3.15 compares the model in (3.9) to the measured IM_3, showing its inability to capture the hyperabrupt varactor's nonlinear behavior. The discrepancy grows with more unit cells, highlighting the need for precise C-V modeling.

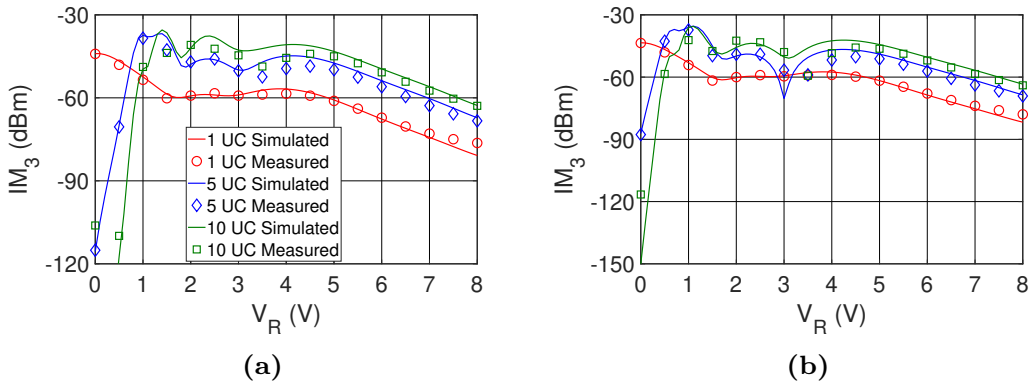

Figure 3.14. IM_3 for the phase shifter with a unit cell length of 57.7° in Paper [A] for (a) upper-band (b) lower-band.

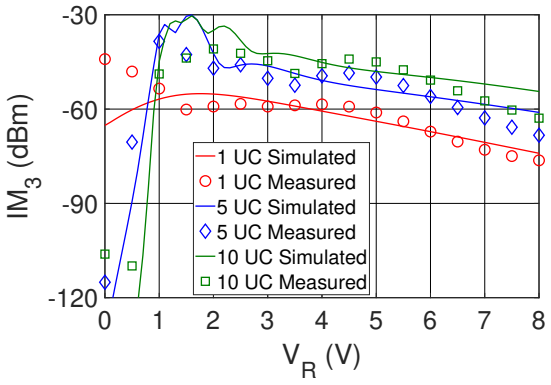

Figure 3.15. Measured and simulated IM_3 when the model in (3.9) is employed.

Fig. 3.16a shows the simulated and measured IM_3 of the phase shifter with 7 unit cells from Paper [B] and [C], with the model from Paper [C], as it was further developed. The varactor model parameters were from the datasheet, and the coaxial connector was modeled as an LC network. These parameters were optimized to match the measured S-parameters. The model was employed to examine simulated forward and backward IM_3 when varying the number of unit cells. The results are depicted in Fig. 3.16b, where 1 to 11 unit cells are simulated at $V_R = 0.5$ V and $P_{\text{in}} =$ -10 dBm. As the number of unit cells increases, the forward IMD also increases. In contrast, the reverse IM_3 behavior depends on whether the phase shifter has an odd or even number of unit cells. For even numbers, IM_3 increases with more unit cells, while for odd numbers, the trend is reversed. It can be observed that the IM_3 for 2 and 11 unit cells is similar. This observation can be explained by destructive interference, as explained in [16]. When two nonlinear sites are separated by an odd number of

quarter wavelengths, the IM_3 value is minimized due to destructive interference. Conversely, when an even number of quarter wavelengths are present between the sites, a maximum of IM_3 is obtained. Hence, the lower IM_3 value with 11 unit cells can be attributed to the destructive interference of the multiple IM sources.

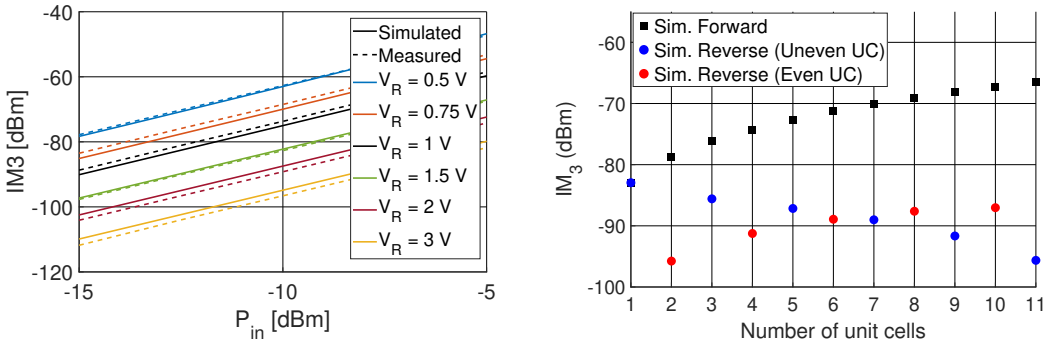

(a) **(b)**

Figure 3.16. (a) Measured and simulated IM_3 for the phase shifter with 7 unit cells in Paper [B] and [C]. (b) Simulated IM_3 with varying number of unit cells.

3.8 Model based optimization

The following section examines whether there is an optimal design for loaded-line phase shifters in terms of figure of merit (FOM) and linearity. The model developed in Paper [A] is used, with a unit cell length of 57.7°. Therefore, the parameters C_V, θ_0, R_s, and L_s refer to that unit cell. The effect of the cell length and the varactor-diodes quality factor is investigated.

3.8.1 Influence of unit cell length

The influence of unit cell length was examined by reducing the unit cell length of the reference unit cell ($\theta_e = 57.7°$). The effect of reducing the unit cell length is that the capacitance per unit cell length will increase, which is undesirable for the comparison. Instead, the capacitance per unit cell length should be consistent for all different unit cell lengths that were compared to have a fair comparison. This was achieved by modifying the varactor's capacitance with the same amount of reduction of the unit cell length. However, reducing C_V will also affect the quality factor of the varactor, and therefore, the series resistance had to be modified to compensate for the change in quality factor. Fig. 3.17 illustrates how θ_0, C_V, and R_s are scaled with the value N. As we

are reducing the length of the unit cell, θ_0 and C_V are divided by N, and R_s is multiplied by N. This enables a comparison where the unit cell length is different while the capacitance per unit cell length and the quality factor is maintained for each unit cell. In this study, N is chosen to have the value of 1, 2, 4, and 8, where $N = 1$ for the reference unit cell.

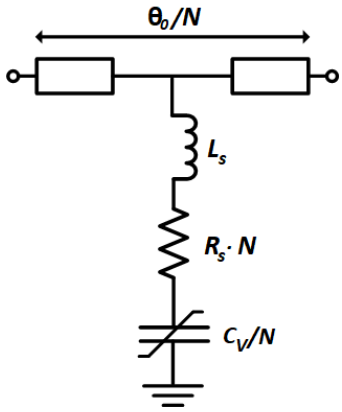

Figure 3.17. Modification of the unit cell to maintain the same capacitance per unit cell length and quality factor for all phase shifters. The reference unit cell has an $N = 1$.

The reference phase shifter was designed with 10 unit cells, which gives a differential phase shift larger than 180°. The physical length was the same between all phase shifters in the comparison. Therefore, the phase shifters with unit cell lengths of $\theta_0/2$, $\theta_0/4$, and $\theta_0/8$ had 20, 40, and 80 unit cells, respectively. The unit cells had different IL, and it was suspected that they might have different tuning ranges that optimized their FOM. Therefore, the differential phase shift and the FOM were plotted as functions of V_{Rmin} when V_{Rmax} was set to 8 V, at the design frequency of 1.5 GHz, as depicted in Fig. 3.18. If the tuning range is the same, one can conclude from the figure that the largest differential phase shift is generated for the phase shifter with the longest unit cell, and the greatest FOM is generated for the phase shifter with the shortest unit cell. However, with a shorter unit cell, the IL reduces and enables a larger tuning range with a larger FOM. Therefore, Fig. 3.18 was utilized to find the V_{Rmin} that generated the maximum FOM for each phase shifter. The figure shows that the phase shifters with a unit cell length of θ_0, $\theta_0/2$, $\theta_0/4$, and $\theta_0/8$, generate the largest FOM when V_{Rmin} is 3 V, 2.25 V, 2 V, and 1.75 V, respectively.

The differential phase shift and FOM was then studied versus frequency in Fig. 3.19 when V_{Rmin} is selected to maximize FOM for each phase shifter. The phase shifter with the shortest unit cell has the greatest FOM over the

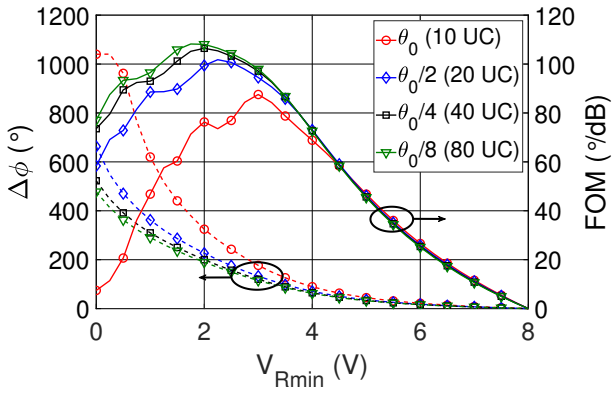

Figure 3.18. The differential phase and FOM when V_{Rmin} is varied and V_{Rmax} is set to 8 V, for each phase shifter with the different unit cell lengths of θ_0, $\theta_0/2$, $\theta_0/4$, and $\theta_0/8$. The plot shows which V_{Rmin} generates the largest FOM for each phase shifter when $V_{\mathrm{Rmax}} = 8$ V.

majority of the frequency spectrum and the largest differential phase shift from DC to 1.7 GHz. However, it should be noted that both FOM and $\Delta\phi$ are quite similar for all phase shifters with reduced unit cell length from DC to 1.7 GHz. The upper-band IM_3 versus V_R is depicted in Fig. 3.20 to evaluate the linearity of the phase shifters. In the lower region of V_R, the IM_3 is the smallest for the phase shifter with a unit cell length of θ_0, and the largest IM_3 is found for the phase shifter with a unit cell length of $\theta_0/8$. At a V_R above 4.4 V, the reference phase shifter obtains the largest IM_3. This demonstrates that having many small nonlinear elements does not necessarily provide good linearity.

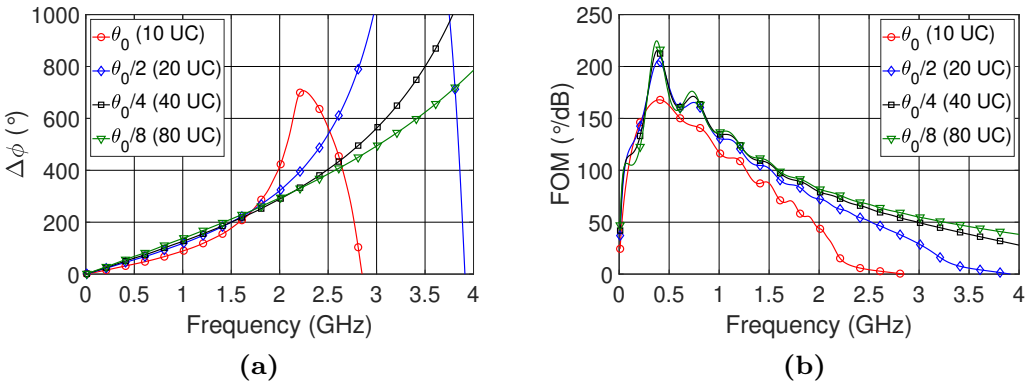

(a) **(b)**

Figure 3.19. (a) Differential phase and (b) FOM when V_{Rmin} is selected to generate maximum FOM for each phase shifter with the different unit cell lengths of θ_0, $\theta_0/2$, $\theta_0/4$, and $\theta_0/8$.

To summarize the results, a phase shifter with shorter unit cells presents better phase shifter performance. In the case of IM_3, a phase shifter designed with fewer but longer unit cells can enhance linearity. It is a trade-off between phase shifter performance and linearity. In the comparison presented, a good trade-off would be the phase shifter with a unit cell length of $\theta_0/2$ as it has good linearity over the full bias range and a FOM = 102 °/dB at 1.5 GHz. This FOM value is similar to the phase shifter with a unit cell length of $\theta_0/8$ with a FOM = 108 °/dB.

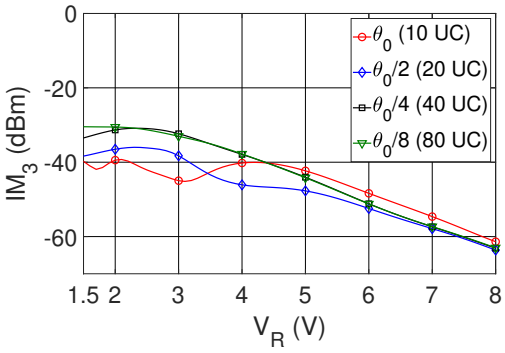

Figure 3.20. Upper-band IM_3 at $P_{\text{in}} = 1.6$ dBm for each phase shifter with the different unit cell lengths of θ_0, $\theta_0/2$, $\theta_0/4$, and $\theta_0/8$.

3.8.2 Influence of varactor-diode quality factor

The same reference unit cell is employed in this study as the previous section. The quality factor of the reference unit cell is denoted as Q_0, and the quality factor was modified by changing R_s in the varactor-diode model. Five phase shifters were compared and the quality factor of their varactor-diodes are $4Q_0$, $2Q_0$, Q_0, $Q_0/2$, and $Q_0/4$, which corresponds to the series resistance of $R_s/4$, $R_s/2$, R_s, $2R_s$, and $4R_s$, respectively. Fig. 3.21a depicts the quality factor for each varactor-diode at 1.5 GHz. All phase shifters consist of 10 unit cells and have the same length. The quality factor affects θ_e marginally. As a result, the differential phase shift remains similar across all phase shifters. However, the quality factor affects the IL greatly as depicted in Fig. 3.21b. An increased quality factor leads to improved IL, which in turn results in a larger FOM [see Fig. 3.21c].

Fig. 3.22 shows the IM_3 for the five phase shifters, the result shows that a larger quality factor increases the IM_3. The increased IM_3 is the result of the smaller series resistance. When R_s is reduced, the voltage swing over R_s is smaller and the voltage swing over C_V increases, which in turn increases

the IM distortion. From the results, one can see that a larger quality factor improves the phase shifter performance greatly. However, it should be noted that there is a trade-off between low varactor loss and IMD.

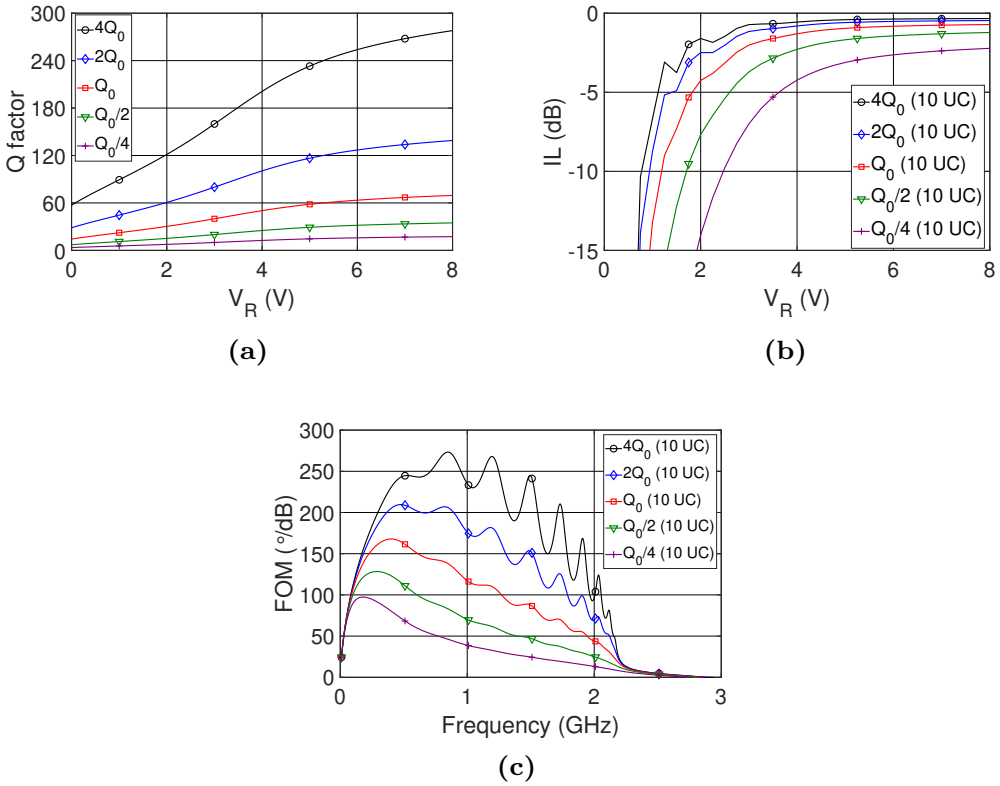

Figure 3.21. The phase shifters' (a) Q factor, (b) IL and (b) FOM for varying Q factors.

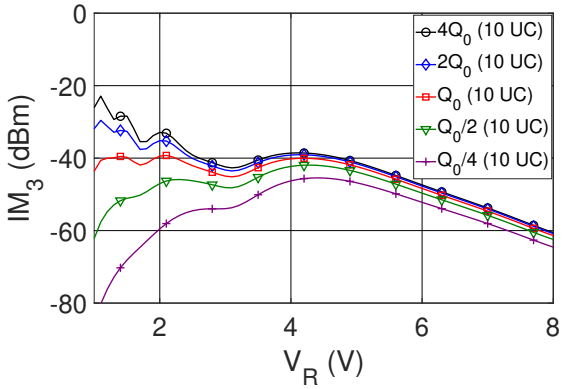

Figure 3.22. Upper-band IM_3 for varying Q factor at $P_{in} = 1.6$ dBm.

CHAPTER 4

Passive Intermodulation due to Additive Manufacturing

This chapter examines how components fabricated by additive manufacturing (AM) affect the PIM level and how they compare to milled components. Section 4.1 provides a general overview of additive manufacturing and a more in-depth explanation of the powder bed fusion-laser beam process. Section 4.2 presents the expected nonlinear source in additive manufacturing. Section 4.3 explains the design and fabrication of the test structure, which are utilized to study PIM in AM components. Moreover, the two-tone measurement setup to measure PIM is described. Section 4.4 provides a distributed nonlinear transmission line model. In Section 4.5, the PIM level in the test structures is presented and discussed.

4.1 Additive manufacturing

Additive manufacturing (AM), commonly called 3D printing, is a manufacturing technique that builds objects by adding material in a selective process, typically layer by layer. This process is the opposite of subtractive manufacturing (SM), where sections of a raw material block are removed through methods such as milling, laser cutting, or electroerosion. AM has gained a large interest in research and industry due to its ability to produce prototypes quickly, create complex designs, produce lightweight structures, and support large-scale production. It is applied in many industries, such as healthcare, automotive, and aerospace. For instance, in the healthcare sector, AM can be used to produce

orthodontic implants and prostheses [60], while in the automotive industry, it enables the creation of monolithic parts that do not require welding [61]. In recent years, the development of microwave and millimeter-wave devices by AM technology has increased due to advancements in precision and material properties, making AM more suitable for manufacturing RF components [62]. Antennas, filters, and waveguides are a few examples of RF components manufactured by AM. Due to AM's ability to reduce cost by minimizing waste and time in production, it is particularly appealing to the space industry. In 2013, NASA and Aerojet Rocketdyne successfully produced AM rocket engine components, achieving a 70% reduction in costs and shortening the manufacturing time from over a year to just four months compared to traditional processes [63].

AM is categorized into seven processes: binder jetting, directed energy deposition, material extrusion, material jetting, powder bed fusion, sheet lamination, and vat photopolymerization. These AM processes can be further divided based on various manufacturing techniques. Each process has advantages and disadvantages, and the suitability of a specific process often depends on the object being produced. The powder bed fusion (PBF) process uses a high-power laser or electron beam to melt and fuse metal powders layer by layer. This results in dense and durable metal components with excellent mechanical properties. PBF offers superior resolution and strength compared to other AM processes, making it well-suited for industries requiring high-performance materials. Therefore, PBF is an excellent choice for producing radio RF components. The following section provides a more detailed explanation of the PBF process.

4.1.1 Powder bed fusion

Powder bed fusion is a process that creates metallic structures using metallic powders. The process begins by applying a fine layer of metal powder across a build plate with a roller. A high-energy laser or electron beam then selectively exposes specific geometries, causing the metal powder to fuse together. Once this layer is finished, the build plate is lowered, and a new layer of metal powder is applied. This cycle is repeated until the final component is complete. Fig. 4.1 illustrates the powder bed fusion process utilizing a laser beam (PBF-LB). The main difference between using a laser beam and an electron beam is their power and speed. Generally, the electron beam operates at higher power and speed, resulting in a poorer surface finish than a laser [61].

Various metal powders can be used in PBF, including the titanium alloy Ti6Al4V, aluminum alloy Al-Si-Mg, and cobalt-chromium alloy Co-Cr. The selection of material depends on the application, e.g., cobalt-chromium alloys

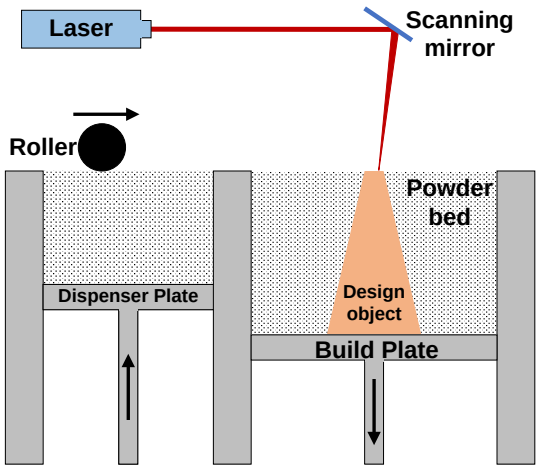

Figure 4.1. Illustration of the powder bed fusion process, where a laser beam selectively fuses the metal powder to create the design object.

are employed in biomedical applications due to their biocompatibility, hardness, and resistance to corrosion [64]. Aluminum alloys are lightweight and are preferred for automotive and aerospace components.

The quality of mechanical properties and surface roughness (R_{rms}) depends on the material and the parameters of the PBF process, as they affect the volumetric energy density that heats up and melts the powder. The metallic powder's grain size, shape, and energy absorption will affect the fusion. The laser source's wavelength and power, scanning speed, layer thickness, and the chamber's temperature control all play important roles in the final product's quality [65]. Suboptimal parameters can cause several effects that degrade quality, such as increased R_{rms} and porosity. The balling effect increases R_{rms} and results in higher porosity, which lowers conductivity [66]. This effect occurs due to an unstable melt pool, causing the molten material to break apart and creating inconsistencies in the melt track. These inconsistencies can lead to inter-layer porosity or instability in the powder layer [67]. Slower laser speeds and longer heating times can help reduce the balling effect. Formation of satellites [65] and Dross formation [68] are phenomenons that occur from the sintering of powder or powder agglomerates to the surface of the solidified material, which also contributes to higher R_{rms}.

4.2 Surface roughness and its effect on PIM

PBF-LB is a promising method for fabricating RF components due to its high resolution and mechanical, electrical, and thermal properties. However, despite its advantages, PBF-LB technology faces challenges such as increased surface

R_{rms} compared to milled metals, which can affect the overall quality of the final product. The amount of additional R_{rms} in AM components depends on the method and material employed. Aluminum alloy (AlSi10Mg) is frequently utilized in the design of RF components as a complement to milled aluminum. The R_{rms} for milled aluminum is approximately 0.5 μm, whereas for PBF-LB AlSi10Mg, it can range from 8 to 20 μm [69].

Surface roughness has been linked to PIM generation through multiple mechanisms. In [12], PIM levels were studied for conductor junctions with surface roughness, which create PIM due to current constriction at asperities and tunneling through MIM contacts. Additionally, surface roughness can induce PIM through electro-thermal effects in imperfect conductors. In imperfect conductors, RF power dissipation from conductor and dielectric losses can lead to self-heating, causing resistivity changes in the conductors [70]. Such effects have been observed in printed lines and lossy conductors [11], where nonlinear sources are distributed across the structure. Equivalent circuits of nonlinear distributed transmission lines are often employed to model these distributed effects [71], [72]. Furthermore, increased porosity in the metal due to the balling effect may also lead to higher PIM levels due to lower conductivity, which increases the surface resistivity.

4.2.1 Surface roughness and conductivity in AlSi10Mg

The surface roughness of a conductor refers to irregularities that deviate from a smooth, ideal surface. These irregularities affect the losses in the conductor because they disrupt the current, resulting in larger surface impedance. Different models have been proposed to explain how irregularities impact losses in a conductor. S. P. Morgan proposed a model in 1949 utilizing triangular or square grooves in a conductor surface to estimate the attenuation in the conductor [73]. The model has been modified and improved to estimate the attenuation up to higher frequencies by first Hammerstad and Jensen [74], and then by Groiss et al. [75]. The Groiss model is valid up to 12 GHz. One physics-based roughness model was proposed by P. G. Huray et al., where the model employed a 3D "Snowball" model to calculate the increased losses due to the surface roughness [76]. The model uses non-uniform spheres, referred to as "snowballs," arranged in the shape of a 3D pyramidal stack. This model has demonstrated good accuracy up to 50 GHz. However, the model is complex, and it is difficult to measure and determine each size of the snowballs accurately. A simplified model is the one-ball Huray model that assumes an equal-sized "snowball" [77]. With this model, a roughness correction factor (H_r) can be calculated and multiplied with the smooth surface impedance (Z_s) to determine the rough surface impedance

$$Z_r(\omega) = H_r(\omega) Z_s(\omega) \tag{4.1}$$

where ω is the angular frequency. The roughness correction factor is described by

$$H_r(\omega) = 1 + \frac{3}{2} \sum_{i=1}^{n} \frac{4\pi r^2 N_i}{A_{\text{flat}}} \left[1 + \frac{\delta}{r} + \frac{\delta^2}{2r^2} \right]^{-1} \tag{4.2}$$

where r is the radius of a snowball, N_i is the number of snowballs, A_{flat} is the area of the flat surface, and δ is the skin depth. The skin depth is defined as

$$\delta = \sqrt{\frac{1}{\pi f \mu \sigma}} \tag{4.3}$$

where f is the frequency, μ is the magnetic permeability, and σ is the electrical conductivity. With higher porosity, the electrical conductivity decreases, which will increase δ and the conductor's surface resistance (R_s).

In [78], the Q-factor was studied in cavity resonators fabricated by milled aluminum and PBF-LB AlSi10Mg. The structures were printed at RISE Research Institutes of Sweden, and the R_{rms} was extracted by a Sensofar Neox S 3D optical profiler. In Paper [D], PBF-LB samples were fabricated at RISE. Therefore, the surface roughness is expected to be similar to what was obtained in [78]. Table 4.1 shows the material and electrical properties of aluminum and AlSi10Mg used in the model developed in Paper [D].

Table 4.1. Properties of Aluminum and AlSi10Mg.

Parameter	**Aluminum**	**AlSi10Mg**
σ [S/m]	3.4×10^7	1.6×10^7
μ_r	1.000021	1.000028
R_{rms} [μm]	0.5	10.42

4.3 Rectangular coaxial transmission line

The following section presents the test structures and measurement setup designed in Paper [D]. This paper examines the differences in PIM levels between PBF-LB AlSi10Mg and milled aluminum. These manufacturing methods and materials result in vastly different surface roughness profiles, and the effects of the surface roughness on losses, current density, and PIM have been investigated. An experimental study based on a rectangular coaxial transmission line

test structure with an interchangeable center conductor has been carried out, where the test structure was designed to exhibit high currents on the center conductor to yield a dominant PIM response from it. A distributed model of the rectangular coaxial transmission line was developed to characterize the nonlinear resistance of the different center-conductors tested and to describe the nonlinear behavior.

4.3.1 Design of test structure

A rectangular coaxial transmission line [see Fig. 4.2a] with an interchangeable center conductor was designed to examine the effect of PIM in PBF-LB manufactured structures. This setup provides flexibility as it allows for the replacement of several center conductor samples. Milled and PBF-LB printed center conductors were fabricated using aluminum and AlSi10Mg materials, respectively. The outer conductor was realized by milled aluminum. Four types of center conductors were tested:

1. Milled aluminum - Square cross-section
2. PBF-LB AlSi10Mg - Square cross-section
3. Milled aluminum - Circular cross-section
4. PBF-LB AlSi10Mg - Circular cross-section

The two cross-sections are illustrated in Fig. 4.2b and Fig. 4.2c. The square conductor has a side length of $a = 3.5$ mm, and the circular conductor has a diameter of 3.5 mm. The outer conductor is square-shaped with a side length of $b = 13$ mm. The rectangular coaxial transmission line was designed to generate a transverse electromagnetic (TEM) wave that induces high surface currents on the center conductor, resulting in a dominant PIM level at the center conductors. Additionally, the design prevents unwanted modes and provides structural strength to the center conductor to avoid bending or breaking.

4.3.2 Realized coaxial transmission line

The fabricated rectangular coaxial transmission line is depicted in Fig. 4.3. The outer conductor was realized by milling two sections along its length. These two sections included waveguide transitions on the input (TX) and output (RX), which were required to connect the DUT to the measurement setup. The TX was designed to match a WR112 interface, and the RX was designed to match a WR90 interface. The TX transition supports the TE_{10} mode, which transforms into a TEM mode when transitioning to the DUT.

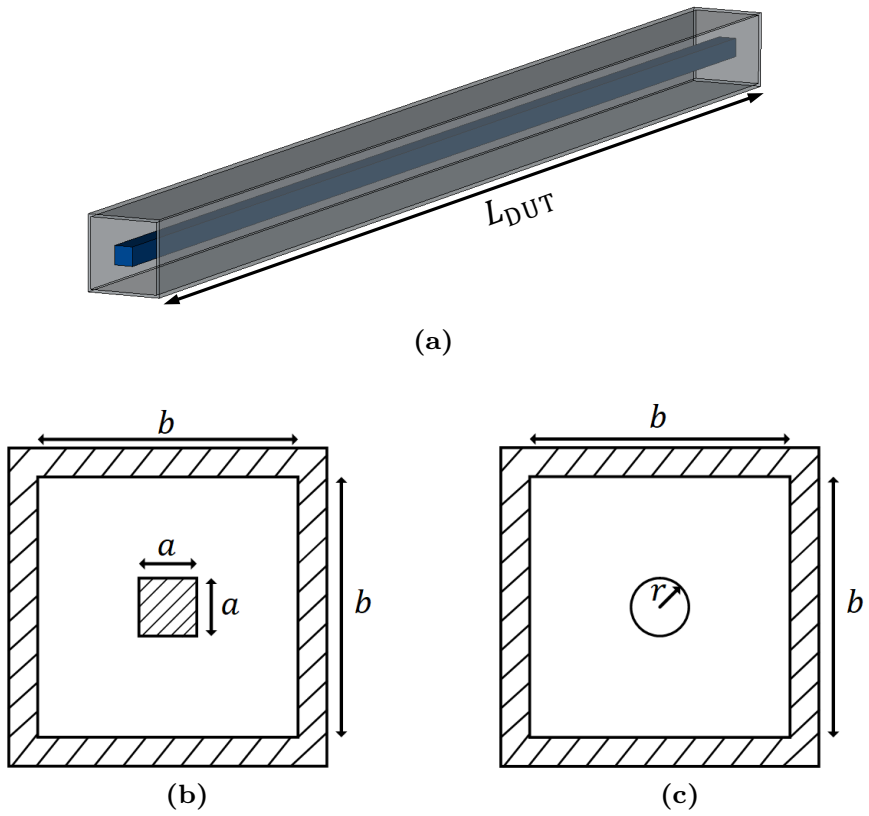

Figure 4.2. The rectangular coaxial transmission line (a) illustration of DUT (b) cross-section of the square center conductor and (c) cross-section of the circular center conductor. The parameters have the following values $L_{\mathrm{DUT}} = 250$ mm, $a = 3.5$ mm, $b = 13$ mm, and $r = a/2$.

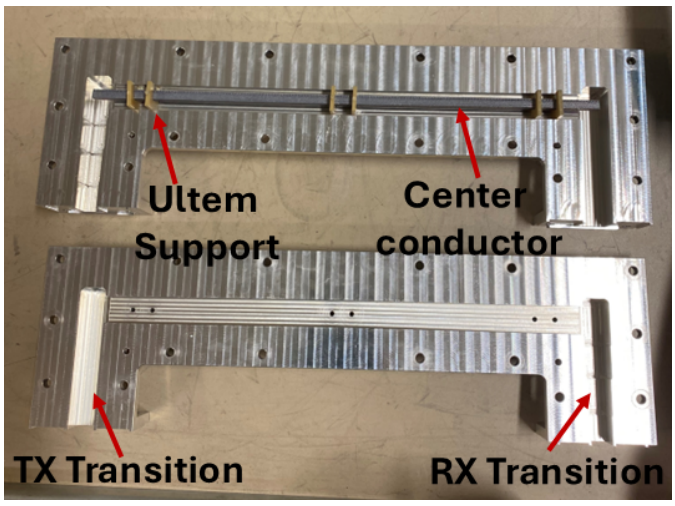

Figure 4.3. The DUT before assembling. The two milled aluminum parts comprise the TX and RX waveguide transitions, as well as the outer conductor of the DUT. The top milled part shows the inner conductor attached by six Ultem supports.

The two sections are assembled with several screws that are designed to apply a pressure of 70 MPa. This contact pressure ensures that the aluminum reaches its elastic deformation[79], which has been shown to minimize PIM between metallic contact [12]. The center conductor is held in place by six Ultem support pieces within an air cavity. An air cavity was used to avoid dielectric nonlinear sources [80]. The Ultem support is expected to have a negligible effect on PIM due to its electrical properties.

The PBF-LB center conductors were manufactured at the RISE Research Institutes of Sweden using an SLM280 Twin machine. This machine employs two IPG fiber lasers with a maximum power output of 400 W and focused spot sizes of 0.075 mm. The fabricated center conductors are shown in Fig. 4.4, where a clear difference in surface roughness between the milled and AM printed conductors can be observed. In the circular PBF-LB center conductors, unwanted small metallic discontinuities were generated during the manufacturing process caused by the attachment points in the printing setup. These discontinuities were unavoidable in manufacturing and could not be removed in post-process. The discontinuities can affect the PIM level as sharp corners create high surface currents that may lead to higher PIM levels. Scanning electron microscope (SEM) images were captured to examine the surface microstructures of the PBF-LB structures. Fig. 4.5 displays these SEM images, revealing a high roughness profile, the balling effect, and grains that are fused together.

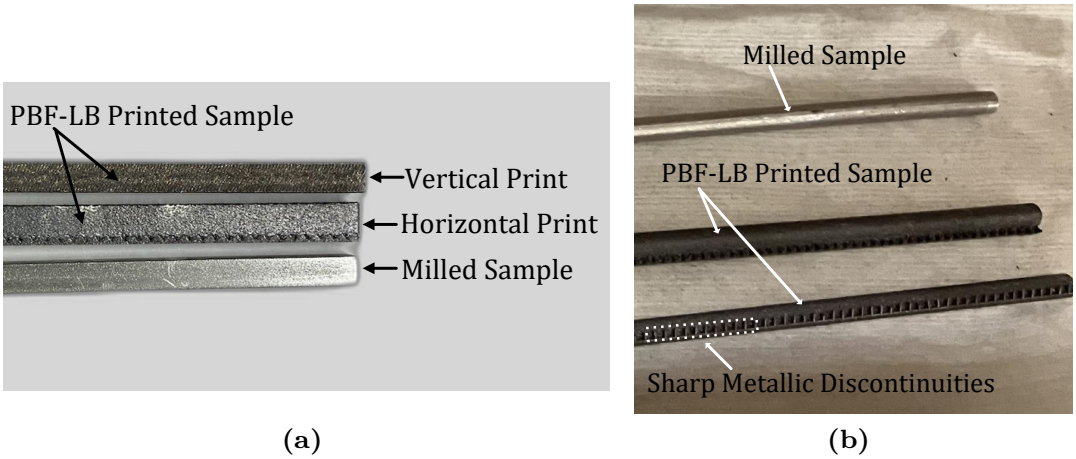

Figure 4.4. The milled and PBF-LB printed center conductors with the cross-sections (a) square and (b) circular.

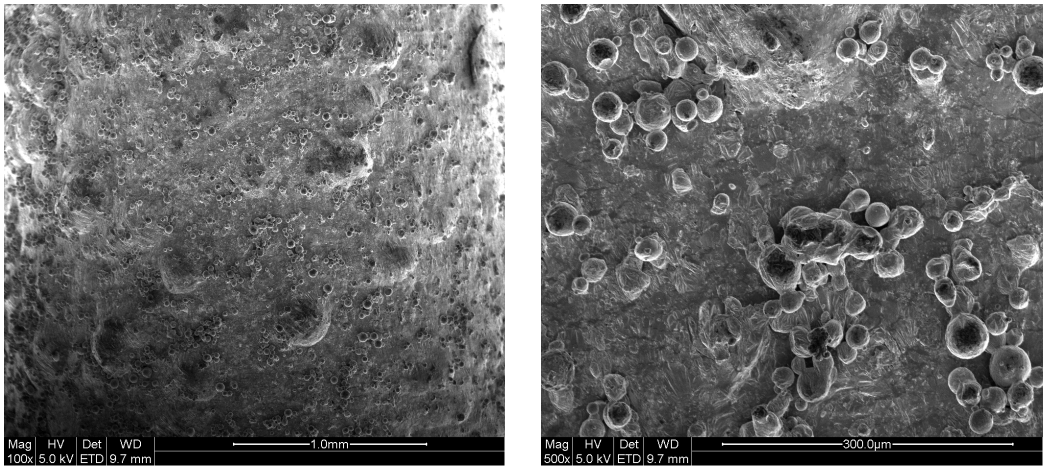

(a) **(b)**

Figure 4.5. SEM images of the PBF-LB samples with (a) 100x magnification and (b) 500x magnification. The images display a more pronounced roughness profile and the balling effect.

4.3.3 Measurement setup

The PIM measurement setup follows the same premise as the two-tone measurement explained in Section 3.5. However, the input power is significantly greater due to the weakly nonlinear sources in a passive component. This results in more strict requirements of the measurement setup in terms of dynamic range, low PIM components, and isolation.

The PIM level of the coaxial transmission line was measured at the facility of Beyond Gravity in Gothenburg. The measurement setup was designed for the X-band, and two carrier signals with the frequencies $f_1 = 7240$ MHz and $f_2 = 7625$ MHz were employed with an input power ranging from 39 dBm to 46 dBm. The measured third-order passive intermodulation (PIM_3) signal had the frequency $f_{PIM3} = 8010$ MHz. The PIM generated in the DUT is transmitted and received by two horn antennas. The full measurement setup is illustrated in Fig. 4.6a, where each equipment number is presented in Table. 4.2. The setup begins with two signal sources that generate the two fundamental tones that are combined and then amplified in a traveling wave tube (TWT) amplifier. The power level is then monitored before entering a chain of bandpass filters (BPF) with a total isolation of 200 dB that removes any IM products generated by the amplifier and PIM products generated by the amplifier's output waveguide. The BPFs are designed with high-pressure flanges to mitigate metallic contact PIM. After the BPFs, the carriers enter the waveguide transition that leads to the DUT. The carriers and the generated

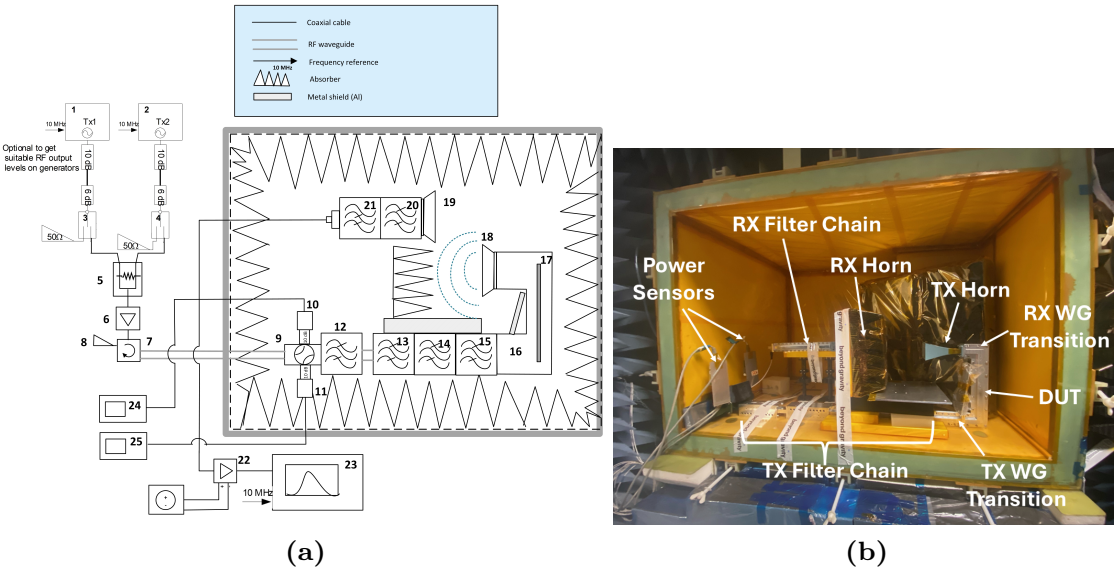

(a) (b)

Figure 4.6. PIM measurement setup with (a) illustration of the setup where each component is described in Table 4.2, and (b) anechoic chamber containing the DUT, the TX- and RX-filter chains, and the TX and RX horn antennas.

PIM signals are transmitted from a horn antenna to a receiving horn antenna. The received signal passes through the RX BPFs designed for 8010 MHz. A spectrum analyzer is then measuring the PIM signal. The antennas and the BPFs are inside an anechoic chamber, as shown in Fig. 4.6b. Due to the presence of the two horn antennas, path losses and misalignment losses were considered. The coupling between the antennas was measured to 45 dB, which was employed to determine the actual generated PIM power in the DUT.

4.4 Distributed nonlinear transmission line model

A transmission line can be represented by a lumped-element equivalent circuit model. The circuit model is composed of cascaded line segments, where the linear part of the line segment is represented by the per-unit-length capacitance C_0, conductance G_0, inductance L_0, and resistance R_0. The line segment's length scales the per-unit-length parameters. Additionally, the equivalent circuit model can incorporate distributed nonlinearities.

The presence of PIM in transmission lines is caused by weakly intrinsic nonlinear sources, such as material properties, that are distributed along the transmission line. In the case of coaxial transmission lines, the primary PIM source is anticipated to be the surface roughness. The lumped-element equivalent circuit model is well suited to describe the distributed nonlinearities

Table 4.2. Equipment for test setup shown in Fig. 4.6a.

No.	Equipment type	No.	Equipment type
1	Signal source	14	BPF TX signal
2	Signal source	15	BPF TX signal
3	RF door safety switch	16	DUT
4	RF door safety switch	17	Interchangeable center conductor
5	Wilkinson divider	18	TX Horn
6	TWT amplifer	19	RX Horn
7	Circulator	20	BPF RX signal
8	High power load	21	High-pass filter
9	Waveguide directional coupler	22	Low-noise amplifier
10	Power sensor Forward Tx Power	23	Spectrum analyzer
11	Power sensor Reflected Tx Power	24	Power meter Forward Tx Power
12	BPF TX signal	25	Power meter Reflected Tx Power
13	BPF TX signal		

of the coaxial transmission line. The line segment of this model is illustrated in Fig. 4.7. This model includes some simplifications. Firstly, the conductance can be neglected because the cavity is air-filled. Additionally, the nonlinear capacitance can be disregarded because it relates to nonlinearities in the dielectric material [80]. We also assume that the nonlinear inductance can be removed. In superconductors, nonlinear inductance can have a pivotal role in modeling PIM where the nonlinearity is associated with kinetic inductance in the superconductors [32]. Additionally, in bent structures, nonlinear inductance may affect PIM [33]. In a straight transmission line with a regular conductor, there should not be any nonlinear effects from the inductance. Therefore, only a weakly current dependent nonlinear resistance $\Delta R(i)$ is considered. The nonlinearity is assumed to have a quadratic form and is restricted to the second order. Higher-order terms can be included to approximate higher-order PIM components. For a coaxial line, both the inner and outer conductors must be

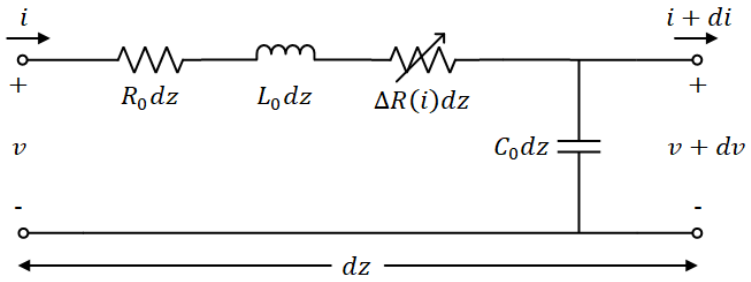

Figure 4.7. A line segment of a distributed transmission line model represented by its linear per-unit-length parameters R_0, L_0, C_0, and its nonlinear resistance $\Delta R(i)$.

considered, leading to the following expression

$$\Delta R(i) = (R_{\mathrm{i},2} + R_{\mathrm{o},2})i^2 \tag{4.4}$$

where the subscripts i and o denote the inner and outer conductors, respectively, while R_2 represents the macroscopic nonlinear parameter of the conductor, with the units $\Omega\mathrm{A}^{-2}\mathrm{m}^{-1}$.

In [81], a superconducting device's quadratic nonlinear resistance is formulated. This formulation can be adapted for a normal conductor as the following

$$R_2 = 2\sigma\mu^2\omega^2\delta^4 \frac{\Gamma}{j_0^2} = a_2 \frac{\Gamma}{j_0^2} \tag{4.5}$$

where j_0 is the characteristic current density and Γ is the geometrical factor, which is expressed as

$$\Gamma = \frac{\int j^4 dS}{(\int j dS)^4}. \tag{4.6}$$

The geometrical factor, with the unit of m^{-6}, is derived by integrating the current density distribution across the cross-sectional area of the conductor. The characteristic current density, with the units of Am^{-2}, serves as a scaling parameter for the nonlinearity and is fitted to measurement data to determine the nonlinear resistance. The expression of a_2 in (4.5) has the units $\Omega\mathrm{m}$, resulting in the units $\Omega\mathrm{A}^{-2}\mathrm{m}^{-1}$ for R_2. The geometrical factor can be determined analytically if a well-defined expression exists for the current density distribution. Otherwise, a numerical simulation of the current density distribution is required to calculate Γ.

4.4.1 Linear model parameter extraction

A circular coaxial cable have closed-form expressions of the per-unit-length parameters [82]. However, deriving these expressions for a rectangular coaxial transmission line is more complicated. Various methods, such as conformal mapping, finite element method (FEM), method of moments (MoM), and Equivalent Electrodes Method (EEM), have been used to determine the capacitance, inductance, and characteristic impedance (Z_c) [83]–[87]. To approximate L_0 and C_0, closed-form expressions from [85] were employed obtained by FEM, MoM and curve fitting techniques. The expressions works for both rectangular coaxial transmission lines with circular and rectangular inner conductors. The following expression were used

$$L_0 = L_K + A_1 \exp\left[-\frac{(r - r_0)}{t_1}\right] \tag{4.7}$$

$$C_0 = \varepsilon_r \left(C_K + A_1 \exp\left[-\frac{(r - r_0)}{t_1}\right] + A_2 \exp\left[-\frac{(r - r_0)}{t_2}\right] \right) \tag{4.8}$$

where L_K, C_K, A_1, A_2, r_0, t_1, t_2 are coefficients that vary depending on geometry, and r is the ratio between the inner and outer conductor. The circuit model was compared with EM simulations and they provided accurate results. However, slight tuning of the inductance were performed to match the phase.

The linear resistance was estimated by calculating the linear resistance of a circular coaxial cable made of aluminum and fitting the results to the EM simulation. Table 4.3 presents the per-unit-length parameters for each case. The circuit simulation and EM simulation are compared in Fig. 4.8 for the rectangular coaxial transmission line with a circular inner conductor, which shows excellent agreement. The higher surface roughness in PBF-LB printed structures increases losses significantly, especially at higher frequencies, as shown in Fig. 4.9. At 8 GHz, the loss is around 6.5 times greater for the PBF-LB printed structures.

Table 4.3. Per-unit-length parameters for different cases.

Center conductor	$\boldsymbol{C_0}$ [pF/m]	$\boldsymbol{L_0}$ [nH/m]	$\boldsymbol{R_0}$ [Ω/m]
Milled Circular	39.8	279.6	4.45
PBF-LB Circular	39.8	282.8	30.6
Milled Square	45.85	242.9	4.4
PBF-LB Square	45.85	245.6	29.1

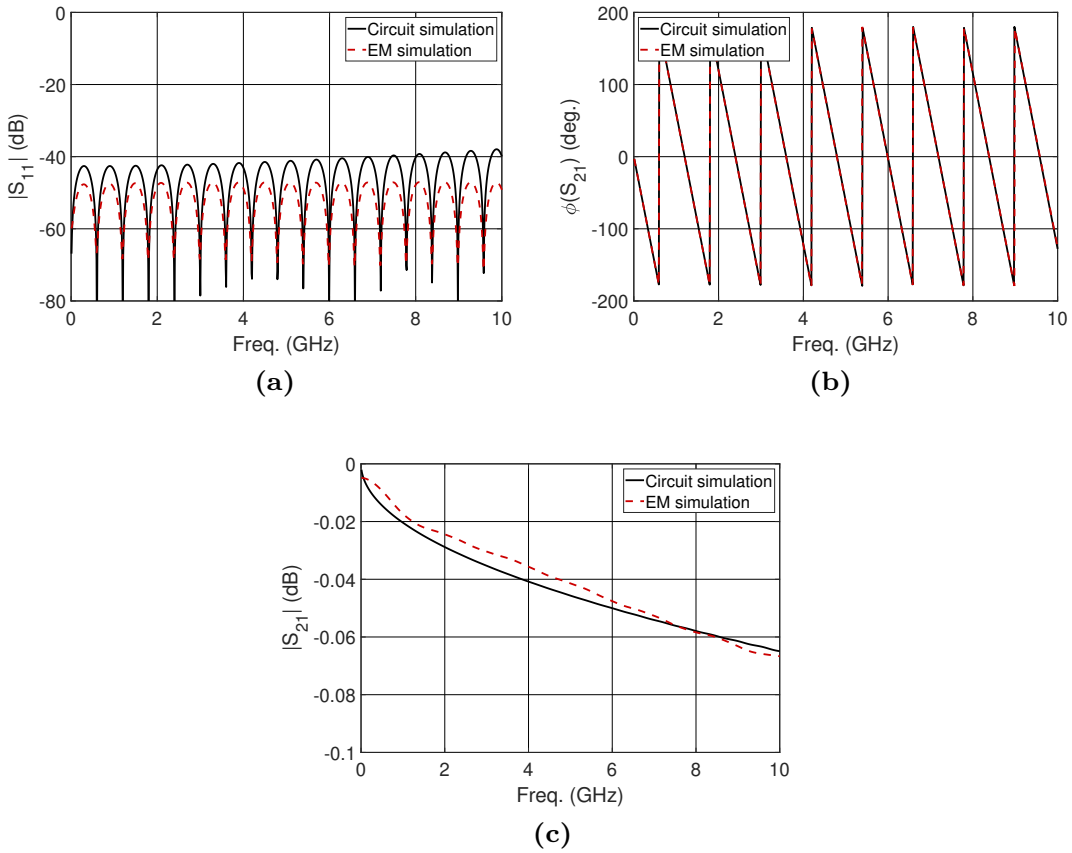

Figure 4.8. Comparison between the circuit model and EM simulation of the coaxial WG with circular inner conductor for (a) RL, (b) phase, (c) IL.

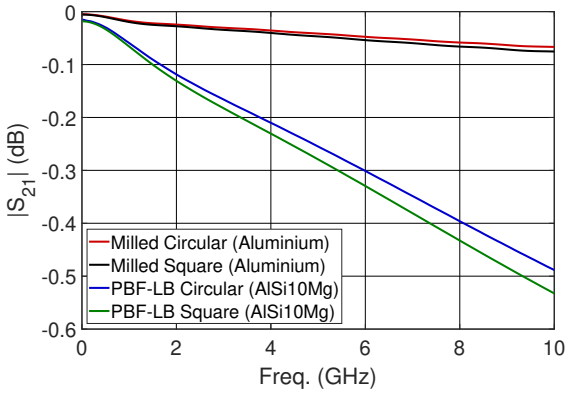

Figure 4.9. Losses EM simulated in rectangular coaxial transmission line for the different inner conductors.

4.4.2 Nonlinear resistance extraction

The nonlinear resistance is the last parameter to be obtained in the distributed model, which is described in (4.5). The parameters σ, μ, ω, and δ are known. The unknown parameters are Γ and j_0. The geometric factor is determined by numerically finding the current density distribution. It is solved numerically due to the rectangular geometry, which makes it very challenging to define an accurate analytical expression for the current density distribution. Lastly, j_0 in (4.5) is a fitting parameter determined by measurements.

All variations of the rectangular coaxial transmission lines were simulated in COMSOL Multiphysics. The magnetic field (H-field) was analyzed to better understand the current density distribution pattern. Fig. 4.10a and Fig. 4.10b depict the H-field of the coaxial transmission line of the milled square and circular inner conductor. The square inner conductor displays a higher maximum H-field compared to the circular inner conductor, with the maximum field located at the corners of the square. In contrast, the circular inner conductor shows a more evenly distributed field around its radius. The fields for the outer conductor are similar in both cases, with nulls in the corners and maximum field strength in the center of each side.

The current density distribution for the coaxial transmission line with a square inner conductor has a similar pattern as the H-field. In Fig. 4.11a, the square inner conductor's current density distribution is shown for milled aluminum. The corners of the inner conductor exhibit peak values and current density decreases with the skin depth inside the conductor. Fig. 4.11b compares the current density distribution along the edge between the milled and the PBF-LB printed square inner conductor. The milled conductor demonstrates a higher current density compared to the PBF-LB printed conductor, which is attributed to its lower surface impedance.

Fig. 4.12a shows the current density distribution along the center diameter of the circular inner conductor. The maximum is at the surface and decreases with the skin depth inside the conductor. There is a small sinusoidal variation of the current density distribution along the circumference of the circular inner conductor. The maxima are located along the x- and y-axes, shown in Fig. 4.10b, corresponding to the peaks of the H-field. The minima are located at 45 degrees relative to the maxima, directed towards the corners of the outer conductor.

Fig. 4.12b depicts the outer conductor's current density along the edge of the coaxial transmission line with a circular inner conductor. The results show that the outer conductor's current density is higher for the sample with a milled inner conductor, with a maximum at the center that decreases to zero at the corners. Similar results were observed for the outer conductor with a

square inner conductor.

The geometric factor was obtained by integrating the simulated current density distribution. The geometric factors for the inner conductors are summarized in Table 4.4. The circular inner conductor has similar Γ for the milled and PBF-LB printed conductors, where the latter has the largest Γ. The square inner conductor has a larger difference in Γ, whereas the PBF-LB printed conductor's Γ is twice as large. The outer conductor has similar Γ for all cases.

Due to the lower current density in the outer conductor, we assume that the inner conductor is expected to be the primary source of nonlinearity. Therefore, we neglect $R_{o,2}$ and simplify the nonlinear resistance to $R_2 = R_{i,2}$.

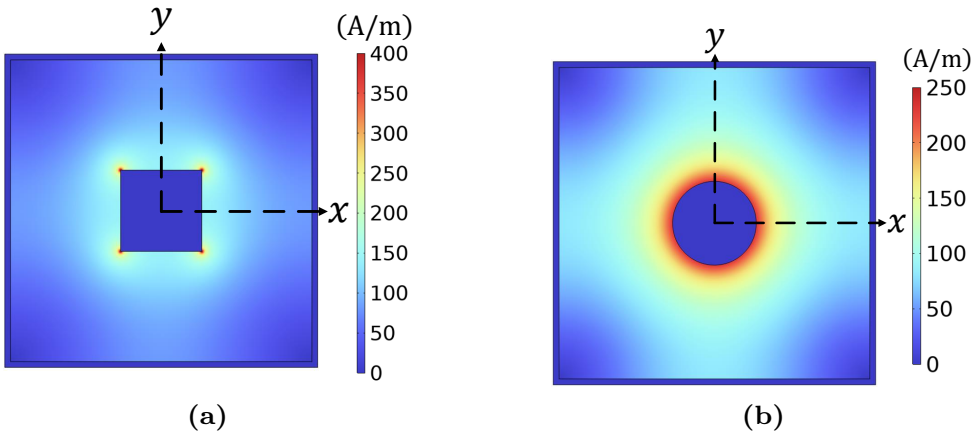

Figure 4.10. The H-field in the rectangular coaxial transmission line of the milled (a) square and (b) circular inner conductor.

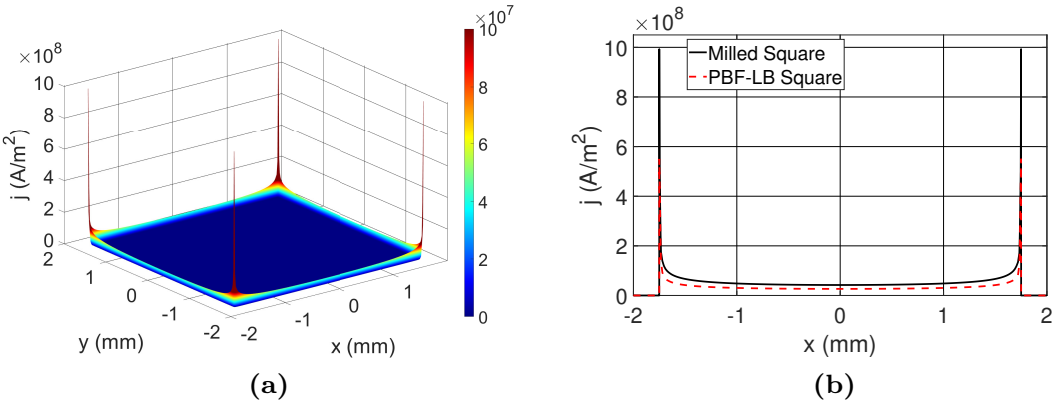

Figure 4.11. The current density distribution of the square inner conductor is represented in (a) a 3D plot of the milled inner conductor, and (b) along the edge for both milled aluminum and PBF-LB AlSi10Mg.

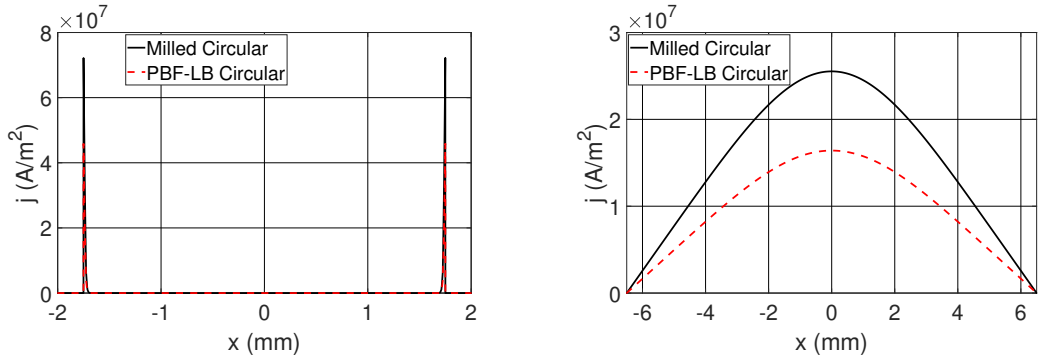

Figure 4.12. The current density distribution in the coaxial transmission line with a circular inner conductor is illustrated for (a) across the central diameter of the inner conductor, and (b) along the edge of the outer conductor.

4.5 Passive intermodulation in PBF-LB printed components

The forward PIM level of the four cases of the coaxial transmission line was measured with the measurement setup in Section 4.3.3 at 8010 MHz, with an input power ranging from 39 to 46 dBm. Simulations were performed in ADS using the Harmonic balance simulator. In this simulation, the coaxial transmission line was represented by a 1 mm line segment, which was cascaded to match the total length of the coaxial transmission line. The nonlinear resistance in the model was calculated with (4.5) and j_0 was obtained from the measurement results. All parameters to calculate $R_{i,2}$ are presented in Table 4.4.

The PIM level of the coaxial transmission line with square and circular inner conductors is shown in Fig. 4.13. The result shows that geometry greatly affects the PIM level, as there is a 13 dB difference between the milled circular and square inner conductor. The square inner conductor exhibits the highest PIM level, which can be attributed to the sharp edges that create high surface current densities. Moreover, from the significant disparity in PIM levels, it can be concluded that the inner conductor is the primary source of PIM and that the contribution of the outer conductor to the total nonlinear resistance in the model can be considered negligible.

The results show that the PBF-LB samples exhibit higher PIM compared to their milled counterpart. The PIM level for the square inner conductor is 6 dB larger for the PBF-LB sample. The circular samples show a significant difference of 19 dB between the milled and PBF-LB printed circular inner

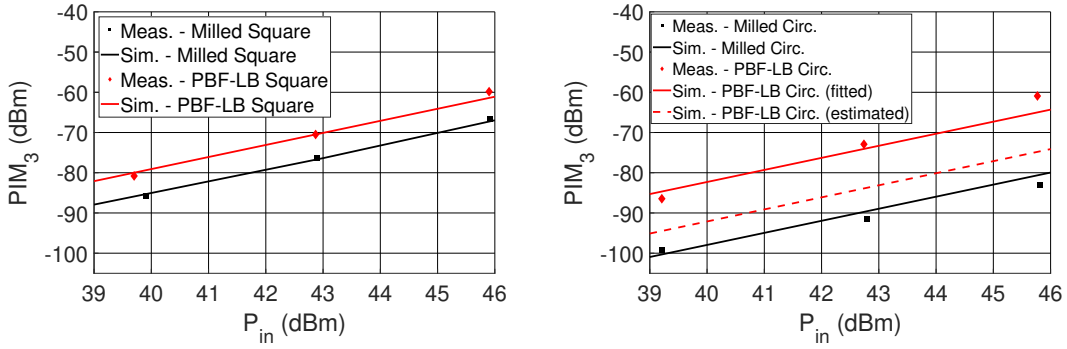

Figure 4.13. The measured and simulated PIM level for the rectangular coaxial transmission line with (a) square and (b) circular inner conductor.

conductor. The difference may result from the sharp metal discontinuities created during the fabrication process of the PBF-LB printed sample, shown in Fig. 4.4b. The sharp edges of the discontinuities create current crowding, which can lead to pronounced nonlinear effects. Additionally, the slope for the measured PBF-LB printed circular inner conductor is different compared to the other cases. It has a 3.8 dB/dB slope, whereas the other cases have a 3 dB/dB slope. This indicates that there is a nonlinear source different from the distributed surface roughness.

An estimate of the PBF-LB printed circular inner conductor's PIM level was calculated [see Fig. 4.13b]. The PIM level was obtained by assuming that the ratio of the characteristic current density of the milled and the PBF-LB

Table 4.4. The values of the characteristic current density, geometrical factor and the nonlinear resistance for the inner conductors. The inner conductor is expected to be the primary source of nonlinearity and $R_{o,2}$ can be neglected, therefore, $R_{i,2} = R_2$.

Center conductor	$\boldsymbol{a_{i,2}}$ [Ωm]	$\boldsymbol{j_{i,0}}$ [A/m^2]	$\boldsymbol{\Gamma_i}$ [1/m^6]	$\boldsymbol{R_{i,2}}$ [Ω/(A^{2}m)]
Milled Square	2.35×10^{-7}	7.1×10^{8}	6.9×10^{21}	3.2×10^{-3}
PBF-LB Square	5×10^{-7}	6.1×10^{8}	5.4×10^{21}	7.3×10^{-3}
Milled Circular	2.35×10^{-7}	1.91×10^{8}	1.18×10^{20}	7.6×10^{-4}
PBF-LB Circular	5×10^{-7}	0.94×10^{8}	1.25×10^{20}	7.1×10^{-3}
PBF-LB Circular (estimated)	5×10^{-7}	1.64×10^{8}	1.25×10^{20}	2.3×10^{-3}

printed circular samples should be similar to the square samples. The square samples' ratio of j_0 is 0.86. By multiplying this ratio with the j_0 of the milled circular inner conductor, we can estimate a characteristic current density of $1.64{\times}10^8$ $\mathrm{A^2m^{-1}}$ for the PBF-LB printed sample. A new R_2 is calculated with the estimated j_0, which is employed to simulate a new PIM level. The PIM level shows a 5.8 dBm difference between the milled and PBF-LB printed samples. This may be a more realistic difference for a PBF-LB printed circular inner conductor without discontinuities.

CHAPTER 5

Passive Intermodulation in Surface Treated Feeding Networks

This chapter examines the PIM characteristics of anodized antenna feeding networks. Section 5.1 briefly explains why different protective coatings are employed in space applications. In Section 5.2, the antenna feeding network and the studied samples are introduced. Section 5.3 provides an analysis of the sample's microstructure, followed by a phenomenological model in Section 5.4. Section 5.5 presents the PIM levels for the different feeding networks under ambient conditions and during thermal cycling. These results are compared to the model results in Section 5.6. Lastly, Section 5.7 provides a discussion regarding potential nonlinear sources and the observed nonlinear behaviors in the feeding networks.

5.1 Space communication and its environment

The harsh conditions of space put a lot of constraints and requirements on the equipment, especially for antennas, as they have to be mounted outside the spacecraft. They have to handle thermal cycles between high to low temperatures, high fluxes of electromagnetic radiation, and high vacuum, and they have to withstand the impact of debris. Reliability is critical, as in-space repairs are impossible. Various coatings are used to protect components and enhance performance. These include thermal coatings with high solar reflec-

tivity and emissivity, optical coatings, and atomic oxygen resistant protective coatings [88]. Thermal coatings that increase emissivity serve as heat sinks, radiating heat into space without adding much weight to the spacecraft. The following sections examine the effects of a specific thermal coating on PIM.

5.2 Antenna feeding networks

Beyond Gravity has designed several antennas for Global Navigation Satellite System (GNSS) receivers, comprising helix and patch excited cup antennas [89]. Fig. 5.1 shows one of the high-power patch excited cup (HPPEC) antenna designed by Beyond Gravity [90]. The antenna comprises three patches surrounded by a metallic cup. The two lower patches act as a resonant cavity, and the top patch functions as a reflector that improves the aperture efficiency. The antenna has two ports that can both be utilized for transmission and reception, with the frequency bands 1515-1562 MHz and 1623-1678 MHz, respectively. The radiator tower is fed by a feeding network that also functions as a polarizer network that provides the two ports with different polarization, right-hand circular polarization (RHCP) and left-hand circular polarization (LHCP). The feeding network is made of aluminum with a protective coating of aluminum oxide Al_2O_3 formed through anodizing. Aluminum is a poor radiator of heat, and the aluminum oxide coating increases the thermal emissivity, which allows the feeding network to dissipate heat through radiation, reducing the ohmic loss. This protection allows operation under large temperature changes and reduces the risk of thermoelastic movements.

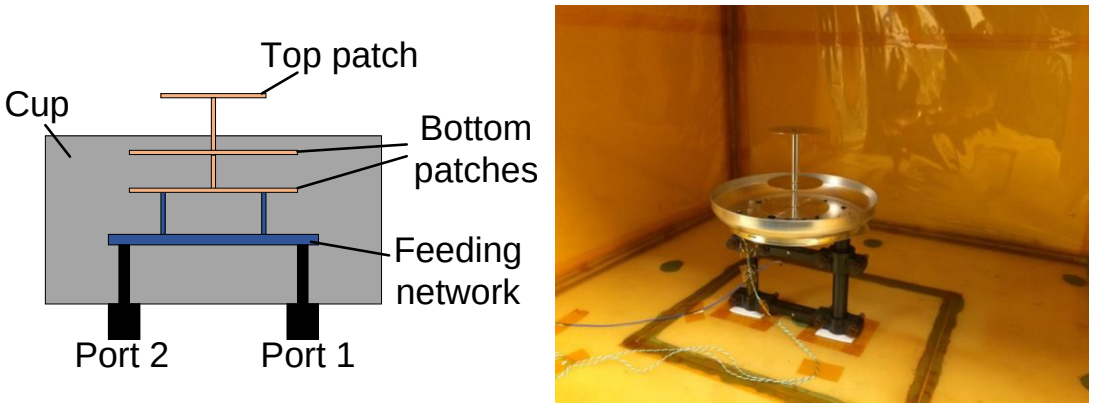

(a) **(b)**

Figure 5.1. The high-power patch excited cup antenna (a) illustration and (b) inside a measurement chamber.

In-house measurements at Beyond Gravity have shown that the coating affects PIM. Previous studies have investigated PIM in ferromagnetic coating materials of coaxial connectors [91], which inherently have nonlinear characteristics. In contrast, the aluminum oxide coating is electrically insulating and does not possess nonlinear characteristics. Paper [E] investigated the PIM performance in several feeding networks to understand why PIM is generated and how different coating thicknesses affect the PIM level.

5.2.1 Samples of feeding networks

Three different coating thickness cases were investigated: native oxide (untreated), 20 μm coating, and 50 μm coating. Fig. 5.2 depicts the three cases. Four samples were fabricated for both the untreated case and the 50 μm case, while two samples were fabricated for the 20 μm case. The untreated case was realized to compare its PIM level to the anodized feeding lines. However, it is not suitable for space applications due to its low thermal emissivity. Native aluminum oxide is typically 2-3 nm [92] and aluminum has an emissivity of $\sim$0.1, whereas Al_2O_3 can have an emissivity of $\sim$0.8 [93]. The 20 μm coating was produced by a Type II class 1 (non-dyed) sulfuric acid anodizing following the MIL-A-8625 standard, where the pores were sealed by boiling deionized water. The 50 μm coating was produced by a Type III class 1 sulfuric acid hard coat anodizing following the MIL-A-8625 standard, and the pores were not sealed.

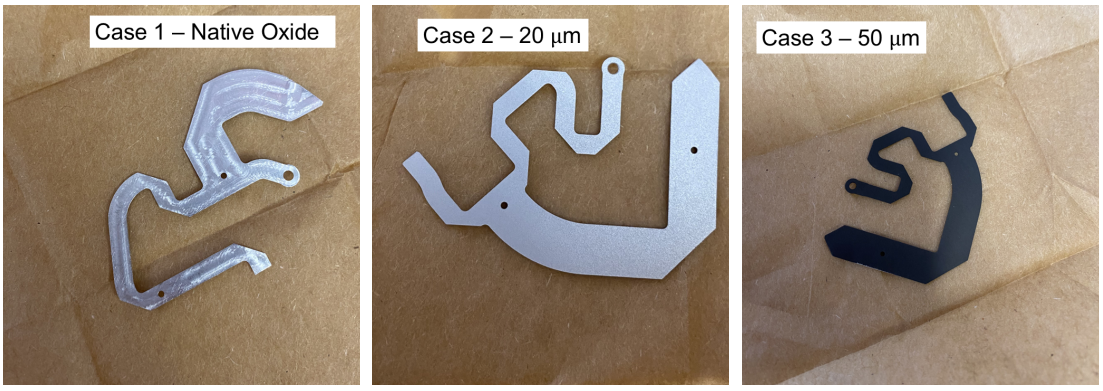

Figure 5.2. The three cases of the feeding networks: (a) Case 1 - untreated with native oxidation, (b) Case 2 - 20 μm coating, and (c) Case 3 - 50 μm coating.

5.3 Microstructures in the samples

The Al_2O_3 coating is electrically isolating and should not influence the current flowing through the aluminum feeding line. It was hypothesized that defects in the coating could impact the PIM level. SEM and focused ion beam (FIB) images of the samples were obtained to investigate this. The following section presents an analysis of the microstructures in the samples.

5.3.1 Analysis of the samples' microstructures

The surface of the samples was examined by SEM images, as shown in Fig. 5.3. The most visible difference between the untreated and anodized samples is the holes and cracks in the anodized samples. The cracks' widths vary between 0.1 to 1 μm, and their lengths vary between 5 to 200 μm. The samples with a thickness of 50 μm show more cracks than those with a thickness of 20 μm. The formation of cracks is caused by thermal stresses when two materials have different thermal expansion coefficients [94]. The thermal expansion coefficient of aluminum is 5 times greater than that of aluminum oxide. Consequently, temperature changes during the anodizing process and high-power antenna operation may lead to crack formation. Two other factors influencing crack formation are environmental humidity and coating thickness. In low humidity environments, coatings lose water, leading to significant tensile stresses. Thicker coatings are more susceptible to cracking compared to thinner coatings, and thicker coatings crack at lower temperatures [95]. Therefore, thicker coatings are more likely to have more cracks.

FIB imaging was employed to view the cross-section of the samples. This enables us to determine whether the holes and cracks extended to the aluminum, which may impede the current and affect the PIM level. The FIB process was time-consuming for the 50 μm samples, so some of their cross-section was prepared by cutting and polishing them. The images are displayed in Fig. 5.4. The native sample has a quite flat profile, but cracks were observed in the aluminum that could potentially be a source of PIM. No holes were found extending to the aluminum in the FIB images, which appeared as shown in Fig. 5.4b. However, the cracks did extend to or near the aluminum. In Fig. 5.4e, two cracks in the 50 μm sample are shown where a small bump of aluminum extends into the crack. This protrusion may have formed due to growth of aluminum during the anodizing process, which could also lead to the presence of aluminum throughout the entire crack.

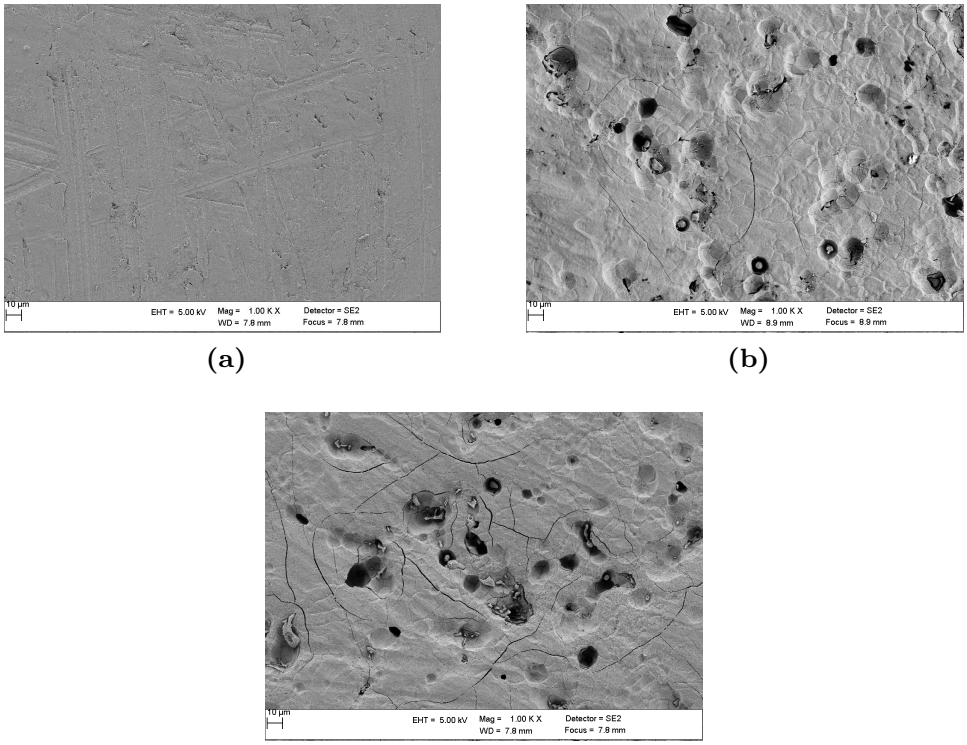

Figure 5.3. SEM images of (a) untreated sample, (b) 20 μm sample, and (c) 50 μm sample.

5.4 Phenomenological model

The anodized feeding network consists of aluminum, through which the current flows, and aluminum oxide, which helps reduce heat through thermal radiation. Ideally, the aluminum oxide should not interfere electrically with the aluminum because it has electrically isolating properties. However, observations from FIB images reveal that cracks extend to the aluminum. The cracks may disrupt the flow of the current, especially if the aluminum has grown into the crack during the anodizing process. This can generate highly localized electrical fields that create nonlinear effects. The cracks will act as nonlinear sources that are distributed along the feeding network, as illustrated in Fig. 5.5, which will generate PIM in the forward (PIM_f) and reversed (PIM_r) direction.

A phenomenological model was developed for the cracks, as the exact nonlinear phenomenon is unknown. In this model, the cracks are assumed to behave as diodes, where the size of the diode corresponds to the area of the cracks observed in the SEM images. The SEM images were processed into pixilated black-and-white images [see Fig. 5.6] to estimate the area of the cracks. White pixels correspond to cracks, and the total number of white pixels was summed

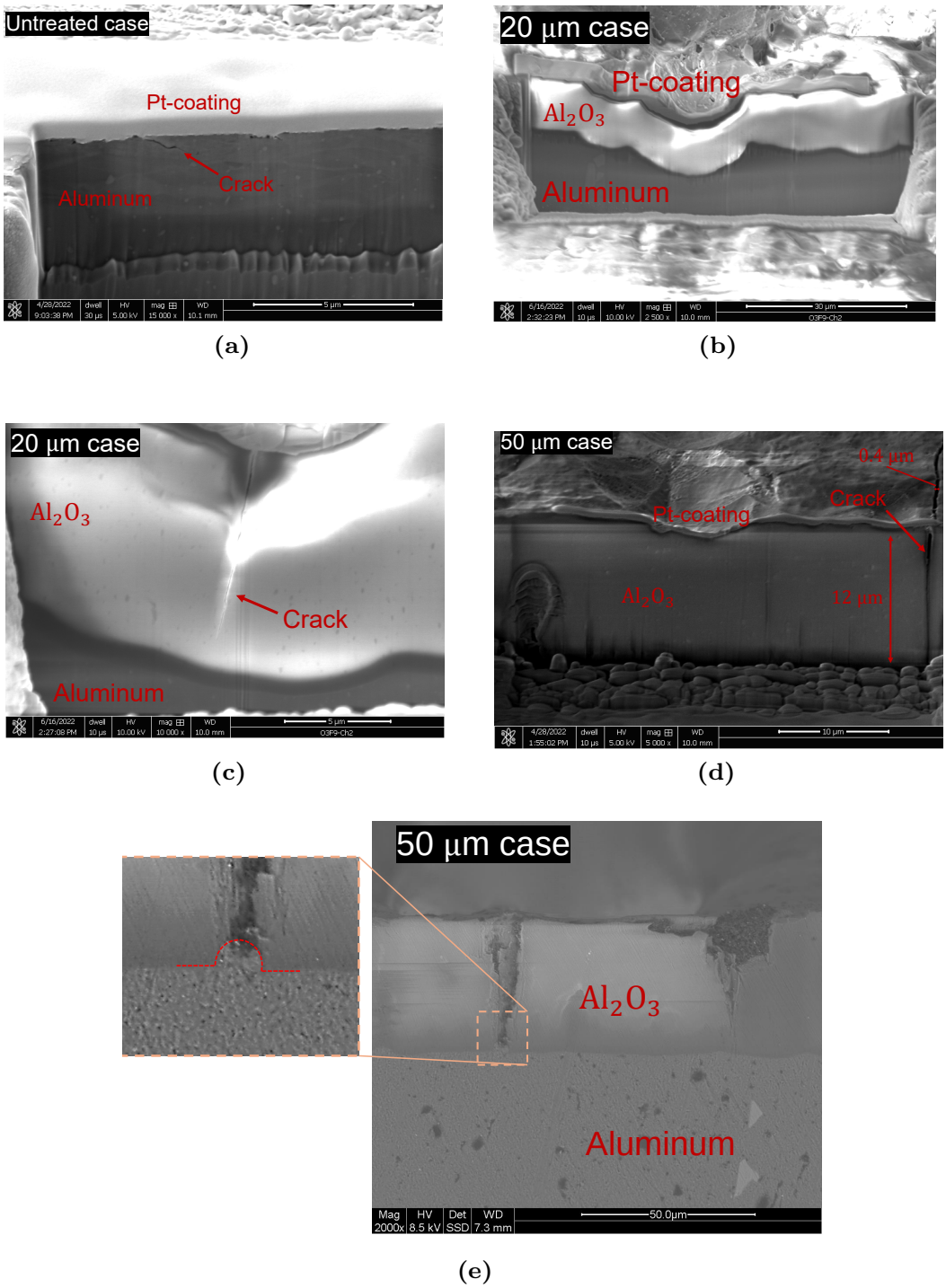

Figure 5.4. The cross-section of the different cases were we observe (a) untreated case with a crack, (b) 20 μm case with a hole, (c) 20 μm case with a crack, (d) 50 μm case with a crack, and (e) 50 μm case with two cracks.

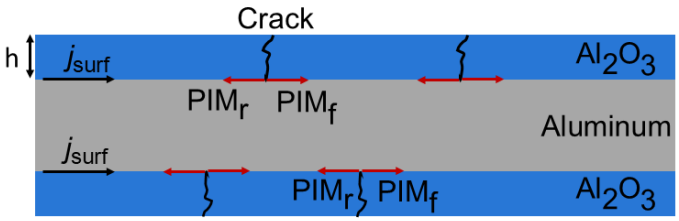

Figure 5.5. Illustration of nonlinear sources produced by cracks in the anodized feeding lines. The sources produce PIM in the forward and reversed direction.

and multiplied by the pixel area. Table 5.1 compares the area of the cracks (A_c) in several SEM images. The results show that the 50 μm has a larger area of cracks, approximately 2 to 7 times larger than the 20 μm case. The area of a SEM image is denoted as A_{SEM}.

Table 5.1. The area of SEM images and their corresponding crack area.

	20 μm		**50 μm**	
SEM #	A_{SEM} [mm^2]	A_c [mm^2]	A_{SEM} [mm^2]	A_c [mm^2]
1	0.0614	0.00022	0.0614	0.00079
2	0.058	0.00021	0.0614	0.00147
3	0.227	0.00184	0.227	0.00316

Fig. 5.6 illustrates a unit cell created based on the SEM images. It is composed of N diodes that have a randomly assigned area, and their total area adds up to A_c. The number of diodes is estimated from the SEM images. The diodes are separated by a transmission line representing the distance between the cracks. The model contains three simplifications:

1. A_c is assumed to be the same at both the top and bottom of the crack.

2. All cracks extend to the aluminum.

3. All cracks are affected by the same input power.

In reality, the cracks can vary in width and length at the bottom, and some may not extend all the way to the aluminum. Additionally, it is known that the current reaches its maximum at the edges of the feeding network and its minimum at the center.

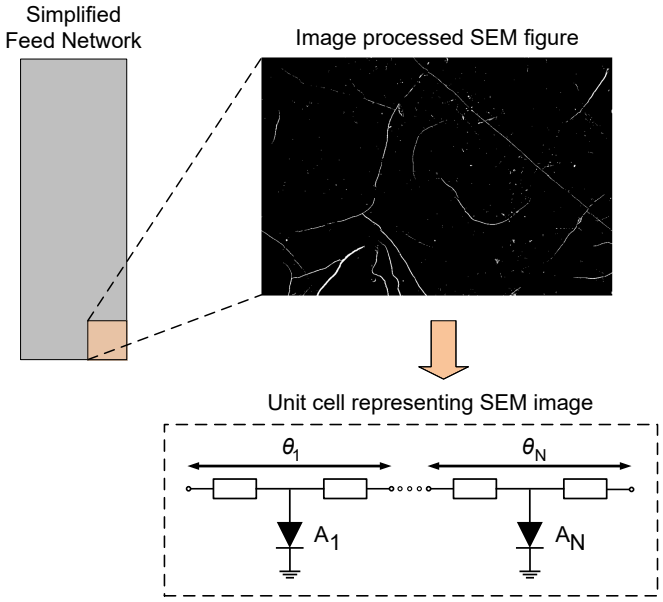

Figure 5.6. The process for modeling the unit cell from an SEM image starts by converting the image into a black-and-white format to estimate the total crack area. This area is then distributed randomly across N diodes representing the cracks in the image.

5.5 Experimental results

In the following section, the PIM performance is presented. The measurement setup is similar to Section 4.3.3. However, it is designed for the L-band, and the setup employs a diplexer that enables measurement of forward and reversed PIM. The two carriers have the frequency of $f_1 = 1518$ MHz and $f_2 = 1559$ MHz, and the fifth-order PIM (PIM_5) was measured at a frequency of 1641 MHz. The PIM_5 was measured at three different input power levels per carrier: 44 dBm, 47 dBm, and 50.5 dBm.

The feeding networks in the HPPEC were measured for ambient temperature (20 °C) and during thermal cycling to determine how the PIM level is influenced by temperature. The HPPEC is placed in a thermal chamber inside the anechoic chamber, where the temperature can be controlled. The thermal cycling varies the temperature between -40 °C and 120 °C. The temperature is held at a steady state for 20 minutes at the minimum and maximum temperatures. Initially, the temperature increases at a rate of 3 °C per minute from 20 °C to 120 °C. After the steady state, the temperature is decreased to -40 °C at a rate of -3 °C per minute. After the steady state at minimum temperature, the temperature is increased to 20 °C, and then the measurement is complete.

5.5.1 PIM at ambient temperature

The results of the PIM measurement at ambient temperature are presented in Fig. 5.7. Several measurements were conducted of the samples, and their variation in PIM level is shown in Fig. 5.7a-5.7c. Variations in the PIM levels across different measurements are expected, as each sample has an unique distribution of nonlinear sources. The variance in PIM level is compared at $P_{\text{in}} = 50.5$ dBm. The maximum variance is observed at $P_{\text{in}} = 44$ dBm, where measurement uncertainty increases due to lower PIM levels, which can be affected by the noise floor of the measurement setup. The variance in forward PIM is 2.5 dB, 3.1 dB, and 7.8 dB for the untreated case, 20 μm, and 50 μm, respectively. The variance in reversed PIM is 5.7 dB, 6.9 dB, and 4.7 dB for the untreated case, 20 μm, and 50 μm, respectively. The results show that the untreated case has the least variation on average and that the 50 μm samples exhibit the greatest variation. This could be a result of the crack formation in the coating that will vary between samples. Additionally, cracks might develop during a measurement cycle due to increased temperatures.

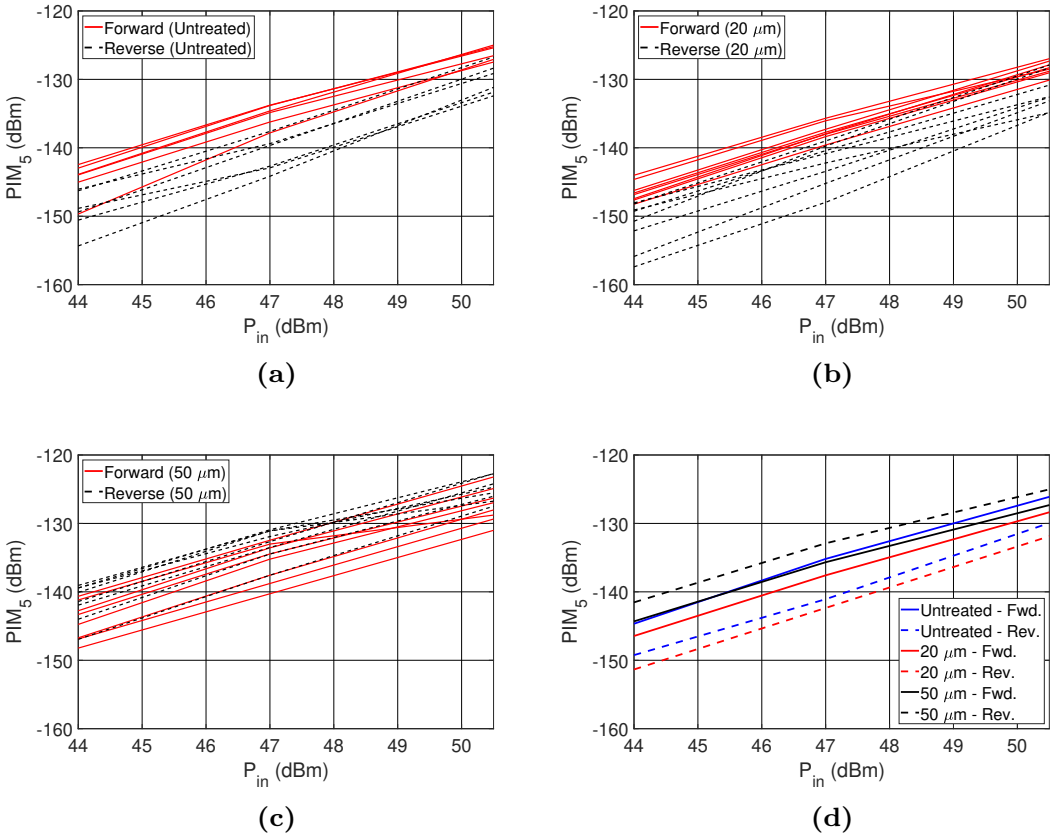

Figure 5.7. Measured 5$^{\text{th}}$-order PIM level for (a) untreated network, (b) 20 μm samples, (c) 50 μm samples, (d) mean value of measurements.

Fig. 5.7d shows the mean forward and reversed PIM level. The 20 μm coating has the best PIM performance. The untreated case exhibits a 1.9 dB larger PIM level than the 20 μm case at $P_{\text{in}} = 50.5$ dBm. The 50 μm coating has a similar forward PIM as the untreated case. However, it has an unusual behavior for reversed PIM as it is larger than the forward PIM level. Typically, $\text{PIM}_{5r} < \text{PIM}_{5f}$. This results in a 6.9 dB difference at $P_{\text{in}} = 50.5$ dBm between the 20 μm case and the 50 μm case.

An interesting observation from the results is that the slopes are lower than the theoretical slope of 5 dB/dB [see Section 2.1]. Previous research has shown that PIM can generate slopes lower than the expected order [96]. We see the same phenomenon here as the mean forward PIM slope is 2.59, 2.63, and 2.38 dB/dB for the untreated case, 20 μm, and 50 μm, respectively. The mean reversed PIM slope is 3.18, 2.99, and 2.26 dB/dB for the untreated case, 20 μm, and 50 μm, respectively. All slope values are lower than 5 dB/dB, and the 50 μm coating has the lowest slope, especially in the reverse direction.

5.5.2 PIM and temperature dependency

The PIM level during thermal cycling is depicted in Fig. 5.8, where each measurement point is plotted. The data of each measurement were fitted by linear regression to obtain a simple relationship between PIM level and temperature. Table 5.2 summarizes the change in PIM level for each measurement, where k_f is the forward slope and k_r is the reverse slope. The result shows that the untreated case has an increased forward and reverse PIM level with increasing temperature. For the 20 μm and 50 μm cases, the reversed PIM level decreases with increasing temperature, averaging around -2.8 dB/100°C. However, the result for forward PIM is inconclusive, as it both decreases and increases from separate measurements.

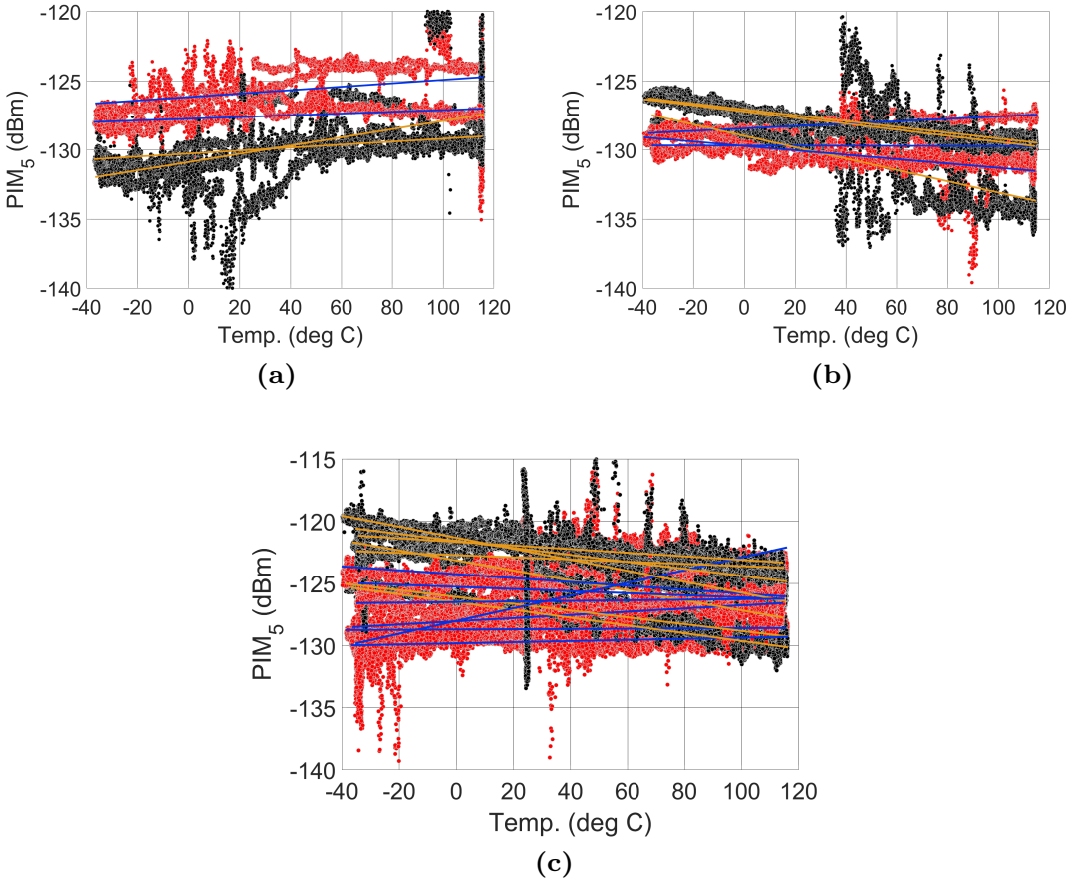

Figure 5.8. Measured PIM_5 as a function of temperature (a) untreated sample, (b) 20 μm sample, and (c) 50 μm sample. Red dot - Forward PIM (blue linear regression line). Black dot - Reversed PIM (orange linear regression line).

Table 5.2. The variation of PIM as a function of temperature.

	Untreated		20 μm		50 μm	
	[dB/100°C]		[dB/100°C]		[dB/100°C]	
Meas. #	k_f	k_r	k_f	k_r	k_f	k_r
1	1.24	2.98	0.87	-2.10	1.28	-4.02
2	0.63	1.08	-0.04	-4.12	0.22	-2.74
3	-	-	-1.59	-2.20	0.45	-3.13
4	-	-	-	-	5.12	-2.80
5	-	-	-	-	-0.85	-1.44
6	-	-	-	-	-1.56	-4.42
7	-	-	-	-	0.23	-0.88
Mean	0.935	2.03	-0.25	-2.81	0.7	-2.78

5.6 Model results

The model presented in Section 5.4 was employed to describe the nonlinear behavior of the anodized feeding networks, and to investigate how the crack area corresponds to the PIM level. The diode model employed was a p-n junction diode, which includes I_s, R_s, C_d, C_{j0}, ϕ, n, and the breakdown voltage (V_b). In the model, the diode's size is represented by the cracks area [see Section 5.4]. A parallel plate capacitor is expressed as $C = (\epsilon_0 A)/d$, where ϵ_0 is the permittivity of space, A is the area, and d is the separation. With this equation, the order of C_d is $\sim$1 fF, and we can assume that C_{j0} will be in the same order. The diode diameter is the width of the crack. In [97], the effect of diode size in micro Schottky contact diodes is studied. In their study, R_s increases with decreasing diode diameter and at 5 μm $R_s = 11$ Ω. As the widths of the cracks are smaller than 5 μm, we expect a larger R_s.

Diode parameters were estimated based on [97] and then tuned to see their effect on PIM. The analysis indicated that the diodes' area, I_s, and R_s had the greatest effects on the PIM level. The effects of ϕ and n were minimal, and their final value was set to $\phi = 1$ V and $n = 1$. Capacitance exhibited a minor effect on the PIM level, and their values were set to $C_d = 25$ fF and $C_{j0} = 5$ fF, based on parallel plate estimation. R_s was estimated to be larger than 11 Ω, and its final value was set to 25 Ω. Reducing R_s to 11 Ω increases the PIM level by 10 dBm. I_s had less effect on the PIM level than R_s, and $I_s = 0.1$ fA was employed in the simulation. Changing the diodes' area affected the PIM level greatly. A minimum and maximum PIM level were simulated corresponding to the values of A_c in row SEM 1 and SEM 3 in Table 5.1, respectively. The A_c was employed as the diode area in a unit cell randomly distributed over the N number of diodes. The number of diodes employed in the model is estimated by the SEM images where the 20 μm model has 20 diodes and the 50 μm model has 50 diodes.

The area of the feeding network A_{feed} is much greater than A_{SEM}, which makes it impractical to simulate the full structure. Instead, the unit cells cascaded composed a smaller area A_{Sim} of the whole feeding line. The PIM level of the simulated area was then multiplied by the ratio $A_{\text{feed}}/\ A_{\text{Sim}}$.

The simulated results are shown in Fig. 5.9. For the 20 μm case, the measured PIM falls within the simulated minimum and maximum levels. In the 50 μm case, the measured PIM is lower than the simulated value. The simulation indicates that the crack area corresponds to the diode's area. While the agreement is not perfect, it remains within an acceptable range for a simplified model, which introduces uncertainties.

The slopes generated in the model are 1 dB/dB because of compression. However, the slope can vary depending on the value of V_b. When

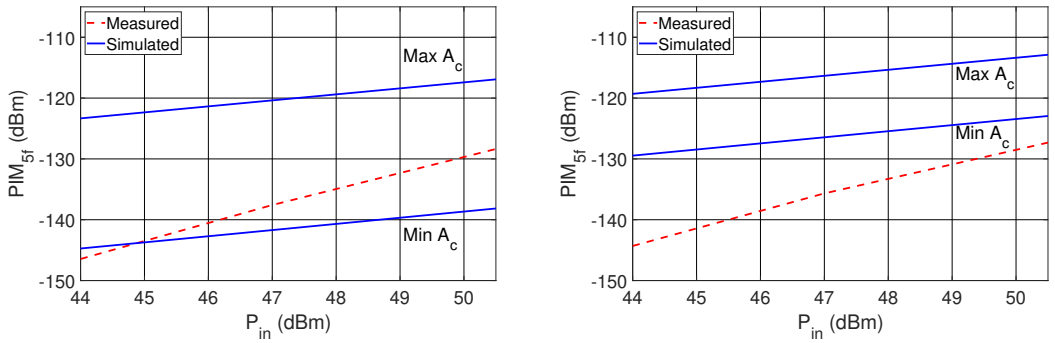

Figure 5.9. The simulated PIM level for (a) 20 μm coating, and (b) 50 μm coating.

$V_b > 0$ V, "sweet spots" are created, which result in minima at certain input powers. Fig. 5.10 illustrates an example of a "sweet spot" for the 20 μm at $P_{\text{in}} = 42.5$ dBm, which affects the slope and generates a 1.8 dB/dB slope between 45 and 47 dBm. Typically, "sweet spots" are linked to active devices [98] and have not yet been identified in passive devices. Lower slopes in PIM have been observed in earlier research for a varying range of input power. The existence of these "sweet spots" could account for the lower slope value, but it would be restricted to a smaller range of input power. The nonlinear PIM sources are more likely to enter compression, generating lower slope levels.

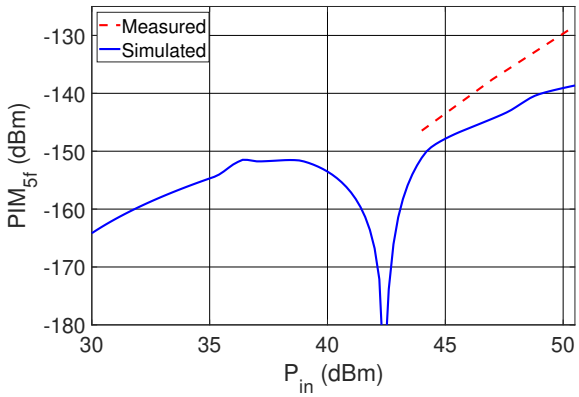

Figure 5.10. Simulated "sweet spot" for the 20 μm case that affects the slope.

5.7 Discussion

The measured results show that the Al_2O_3 coating affects the PIM level in the feeding network. All three cases have similar PIM and slopes, indicating intrinsic nonlinear sources in the feeding. One potential source could be electro-thermal effects as the PIM level increases with temperature for the untreated feeding network. Also, the reverse PIM level for the anodized cases is reduced with increasing temperature. However, other nonlinear sources can also have a temperature dependency.

The anodized feeding networks show varying PIM performance depending on the coating thickness, with the 20 μm coating showing an improvement. Al_2O_3 is electrically insulating and should not directly influence the currents in the feeding network. However, the cracks in the coating may introduce nonlinearities by disrupting current flow, particularly if aluminum grows into these cracks during the anodization process. The 20 μm coating had the least amount of cracks. The improved performance could result from the cracks being too few to be a dominating PIM source. The coating will then function as a heat sink due to the increased thermal emissivity. If the nonlinear source has a temperature dependence, like electro-thermal effects, it will reduce PIM.

The 50 μm coating is more prone to cracking, potentially making it a dominant source of PIM. Its PIM performance deviates from the untreated case and the 20 μm coating, exhibiting a lower slope, greater variability in measured PIM, and higher reversed PIM levels than forward PIM. This suggests that the 50 μm coating influences PIM performance differently, with cracks appearing to be the most likely source of nonlinearity. The phenomenological model also suggests that the cracks in the 50 μm coating could be the dominant source of PIM. The model predicts higher PIM than measured PIM for both the maximum and minimum crack areas in the 50 μm coating.

CHAPTER 6

Conclusions and Future work

6.1 Conclusions

In this thesis, intermodulation distortion (IMD) and passive intermodulation (PIM) have been analyzed and modeled in various components.

Firstly, IMD generated in periodic structures was examined. Specifically, loaded-line phase shifters periodically loaded by varactor diodes. Several phase shifters were designed, fabricated, and measured. A model was developed that accurately described their phase shifter performance and nonlinear behavior. The model in Paper [A] was employed to investigate if there is an optimum design with respect to phase-shift/loss and linearity. It was demonstrated that the phase-shift/loss primarily depends on the Q factor and distribution of varactor capacitance. IMD is primarily proportional to the total varactor-capacitance per unit cell. The study also revealed that an increase in the varactor's Q factor results in higher IMD. Therefore, it is a trade-off between low loss and low IMD. In Paper [B], forward and reverse IMD were investigated for varying numbers of unit cells separated by a quarter-wavelength. Forward IMD increased with more unit cells. Reversed IMD decreased when adding an odd number of unit cells.

The generation of PIM due to additive manufacturing (AM) was examined. An experimental investigation was conducted utilizing a rectangular coaxial transmission line with an interchangeable center conductor, which was fabricated by either milled aluminum or 3D-printed aluminum alloy AlSi10Mg. A

distributed nonlinear transmission line model was developed to describe the observed nonlinear behavior. The AM conductors produced a higher PIM level, which was attributed to their increased surface roughness. Additionally, it was concluded that the current distribution greatly affects the PIM level, which is dependent on the geometric shape of the conductors.

A comprehensive investigation was conducted on PIM in antenna feeding networks coated with aluminum oxide to enhance thermal emissivity. The coating's effect on PIM level was examined in three cases: native oxide (untreated), 20 μm coating, and 50 μm coating. The 50 μm coating had the highest PIM level, whereas the 20 μm coating had the lowest PIM level. The anodized coatings were observed to develop cracks, which were hypothesized to act as nonlinear sources. A phenomenological model was created to relate the area of these cracks to a diode model. The 50 μm coating displayed the highest number of cracks, correlating with its poor PIM performance. In contrast, the 20 μm coating had significantly fewer cracks, suggesting it may not be a dominant nonlinear source in the structure. The improved performance of the 20 μm coating may result from increased thermal emissivity, which can reduce PIM levels if the PIM sources are temperature-dependent.

6.2 Future work

The author would suggest future work with regard to the structures generating PIM. In the case of PIM resulting from AM, it would be valuable to develop the nonlinear model further. This development could involve establishing a relationship between the surface roughness model and electro-thermal effects. Additionally, measuring PIM levels after employing post-processing techniques that reduce surface roughness and porosity would be beneficial. For instance, Hirtisation® reduces surface roughness, and hot isostatic pressing reduces porosity. Studying these effects could improve our understanding of the sources of PIM in AM, and it would be interesting to compare the performance of these processed structures to milled structures.

Future work could also involve studying anodized structures with simpler geometries, such as a straight transmission line of constant width. It would be beneficial to examine more samples with varying thicknesses to observe differences in crack formation. This investigation could help confirm or disprove whether the cracks act as a nonlinear source.

CHAPTER 7

Summary of appended papers

Paper A

Modeling of intermodulation in a loaded-line phase shifter based on a polynomial varactor model

This work investigates if there is an optimum design of loaded-line phase shifters with respect to phase-shift/loss and linearity. Six loaded-line phase shifters were implemented in PCB technology with shunt-loaded varactor-diodes. A equivalent circuit model was developed employing a polynomial series to model the varactors' nonlinear capacitance, and the model was experimentally verified. It was demonstrated that the phase-shift/loss primarily depends on the Q factor and distribution of varactor capacitance. IMD is primarily proportional to the total varactor-capacitance per unit cell. Additionally, study also revealed that an increase in the varactor's Q factor results in higher IMD.
My contributions: design, measurements, nonlinear modeling, analysis of results, writing.

Paper B

Multi-source Intermodulation in a Loaded-line Phase Shifter

This work examines multi-source IM in a tunable loaded-line phase shifter. The phase shifter was constructed using 1, 4, and 7 unit cells, and the simulated and measured results showed good agreement. A quarter-wavelength transmission line separated the varactor-diodes. It was demonstrated that when the number of unit cells is increased, forward IM increases, whereas reverse IM can achieve minima for an odd number of unit cells.
My contributions: design, measurements, nonlinear modeling, analysis of results, writing, and oral presentation.

Paper C

Experimental Investigation of Distributed Intermodulation in an Artificial Transmission Line

This work examined the nonlinear effects of a periodic structure containing multiple nonlinear point sources with known locations and behaviors. The model was verified experimentally. A simulation study investigated how the PIM was affected by increasing the number of unit cells in the artificial transmission line while maintaining the same capacitance per unit cell length and effective electrical length. The results indicated that forward and reversed IMD decreased when we had more unit cells with smaller nonlinearity.
My contributions: design, measurements, nonlinear modeling, analysis of results, writing, and oral presentation.

Paper D

Passive Intermodulation in 3D Printed Coaxial Transmission Lines

This paper investigates the difference in PIM between milled aluminum and 3D printed aluminum alloy (AlSi10Mg). AM is a promising fabrication method. However, it increases surface roughness and porosity. These factors can contribute to elevated PIM levels. This study evaluated a coaxial transmission line test structure with interchangeable center conductors. The linear and nonlinear behavior of the coaxial transmission line was modeled using a distributed circuit model that included a nonlinear resistor. The results showed that AM printed structures have higher PIM levels than their milled counterparts. The

geometry of these structures played a significant role in influencing PIM levels.
My contributions: Idea generation, design, nonlinear modeling, analysis of results, and writing.

Paper E

Passive Intermodulation in Surface Treated Antenna Feeding Networks

This work investigates the generation of PIM in antenna feeding networks, which have a protective coating of aluminum oxide produced by anodization. Three cases were examined: native oxide (untreated), 20 μm coating, and 50 μm coating. SEM- and FIB images revealed that the anodized coating formed cracks, which were hypothesized to act as nonlinear sources. The results showed that the 50 μm coating had the highest PIM level and most cracks. The 20 μm coating had fewer cracks than the 50 μm coating and had the best PIM performance.
My contributions: Analysis of SEM- and FIB images, proposed model, nonlinear modeling, analysis of results, and writing.

References

[1] Ericsson AB, "Ericsson mobility report," Ericsson, Tech. Rep., 2024.

[2] O. Kodheli, E. Lagunas, N. Maturo, *et al.*, "Satellite communications in the new space era: A survey and future challenges," *IEEE Communications Surveys Tutorials*, vol. 23, no. 1, pp. 70–109, 2021. DOI: 10.1109/COMST.2020.3028247.

[3] I. F. Akyildiz, A. Kak, and S. Nie, "6G and beyond: The future of wireless communications systems," *IEEE Access*, vol. 8, pp. 133 995–134 030, 2020. DOI: 10.1109/ACCESS.2020.3010896.

[4] N. Pachler, I. del Portillo, E. F. Crawley, and B. G. Cameron, "An updated comparison of four low earth orbit satellite constellation systems to provide global broadband," in *2021 IEEE International Conference on Communications Workshops (ICC Workshops)*, 2021, pp. 1–7. DOI: 10.1109/ICCWorkshops50388.2021.9473799.

[5] J. Foust, "SpaceX's space-internet woes: Despite technical glitches, the company plans to launch the first of nearly 12,000 satellites in 2019," *IEEE Spectrum*, vol. 56, no. 1, pp. 50–51, 2019. DOI: 10.1109/MSPEC.2019.8594798.

[6] F. Raab, P. Asbeck, S. Cripps, *et al.*, "Power amplifiers and transmitters for RF and microwave," *IEEE Transactions on Microwave Theory and Techniques*, vol. 50, no. 3, pp. 814–826, 2002. DOI: 10.1109/22.989965.

[7] M. F. Haider, F. You, S. He, T. Rahkonen, and J. P. Aikio, "Predistortion-based linearization for 5G and beyond millimeter-wave transceiver systems: A comprehensive survey," *IEEE Communications Surveys Tutorials*, vol. 24, no. 4, pp. 2029–2072, 2022. DOI: 10.1109/COMST.2022.3199884.

[8] I. Angelov, L. Bengtsson, and M. Garcia, "Extensions of the chalmers nonlinear HEMT and MESFET model," *IEEE Transactions on Microwave Theory and Techniques*, vol. 44, no. 10, pp. 1664–1674, 1996. DOI: 10.1109/22.538957.

[9] J. Cai, J. King, and J. C. Pedro, "A new nonlinear behavioral modeling technique for RF power transistors based on bayesian inference," in *2017 IEEE MTT-S International Microwave Symposium (IMS)*, 2017, pp. 624–626. DOI: 10.1109/MWSYM.2017.8058645.

[10] Y. Yamamoto and N. Kuga, "A short-circuit transmission line method for PIM evaluation of metallic materials," in *2006 Asia-Pacific Microwave Conference*, 2006, pp. 1461–1464. DOI: 10.1109/APMC.2006.4429682.

[11] J. R. Wilkerson, K. G. Gard, A. G. Schuchinsky, and M. B. Steer, "Electro-thermal theory of intermodulation distortion in lossy microwave components," *IEEE Transactions on Microwave Theory and Techniques*, vol. 56, no. 12, pp. 2717–2725, 2008. DOI: 10.1109/TMTT.2008.2007084.

[12] C. Vicente and H. Hartnagel, "Passive-intermodulation analysis between rough rectangular waveguide flanges," *IEEE Transactions on Microwave Theory and Techniques*, vol. 53, no. 8, pp. 2515–2525, 2005. DOI: 10.1109/TMTT.2005.852771.

[13] D. E. Zelenchuk, A. P. Shitvov, A. G. Schuchinsky, and V. F. Fusco, "Passive intermodulation in finite lengths of printed microstrip lines," *IEEE Transactions on Microwave Theory and Techniques*, vol. 56, no. 11, pp. 2426–2434, 2008. DOI: 10.1109/TMTT.2008.2005886.

[14] C. Vicente, D. Wolk, H. L. Hartnagel, B. Gimeno, V. E. Boria, and D. Raboso, "Experimental analysis of passive intermodulation at waveguide flange bolted connections," *IEEE Transactions on Microwave Theory and Techniques*, vol. 55, no. 5, pp. 1018–1028, 2007. DOI: 10.1109/TMTT.2007.895400.

[15] J. Henrie, A. Christianson, and W. J. Chappell, "Prediction of passive intermodulation from coaxial connectors in microwave networks," *IEEE Transactions on Microwave Theory and Techniques*, vol. 56, no. 1, pp. 209–216, 2008. DOI: 10.1109/TMTT.2007.912166.

[16] J. R. Wilkerson, P. G. Lam, K. G. Gard, and M. B. Steer, "Distributed passive intermodulation distortion on transmission lines," *IEEE Transactions on Microwave Theory and Techniques*, vol. 59, no. 5, pp. 1190–1205, 2011. DOI: 10.1109/TMTT.2011.2106138.

[17] D. S. Kozlov, A. P. Shitvov, A. G. Schuchinsky, and M. B. Steer, "Passive intermodulation of analog and digital signals on transmission lines with distributed nonlinearities: Modelling and characterization," *IEEE Transactions on Microwave Theory and Techniques*, vol. 64, no. 5, pp. 1383–1395, 2016. DOI: 10.1109/TMTT.2016.2550046.

[18] P. Bolli, S. Selleri, and G. Pelosi, "Passive intermodulation on large reflector antennas," *IEEE Antennas and Propagation Magazine*, vol. 44, no. 5, pp. 13–20, 2002. DOI: 10.1109/MAP.2002.1077773.

[19] D. Smacchia, P. Soto, V. E. Boria, *et al.*, "Advanced compact setups for passive intermodulation measurements of satellite hardware," *IEEE Transactions on Microwave Theory and Techniques*, vol. 66, no. 2, pp. 700–710, 2018. DOI: 10.1109/TMTT.2017.2783383.

[20] J. G. Dumoulin, "Passive intermodulation and its effect on space programs," in *IEE Colloquium on Screening Effectiveness Measurements (Ref. No. 1998/452)*, 1998, pp. 2/1–210. DOI: 10.1049/ic:19980725.

[21] H. Zhang, Y. Zhang, C. Huang, Y. Yuan, and L. Cheng, *Spacecraft Electro-magnetic Compatibility Technologies*. Singapore: Springer, 2020.

[22] D. Wu, Y. Xie, Y. Kuang, and L. Niu, "Prediction of passive intermodulation on mesh reflector antenna using collaborative simulation: Multiscale equivalent method and nonlinear model," *IEEE Transactions on Antennas and Propagation*, vol. 66, no. 3, pp. 1516–1521, 2018. DOI: 10.1109/TAP.2017.2786304.

[23] G. C. Bailey and A. C. Ehrlich, "A study of rf nonlinearities in nickel," *Journal of Applied Physics*, vol. 50, no. 1, pp. 453–461, Jan. 1979. DOI: 10.1063/1.325633.

[24] Y. Wu, W. Ku, and J. Erickson, "A study of nonlinearities and intermodulation characteristics of 3-port distributed circulators," *IEEE Transactions on Microwave Theory and Techniques*, vol. 24, no. 2, pp. 69–77, 1976. DOI: 10.1109/TMTT.1976.1128777.

[25] J. Adam, L. Davis, G. Dionne, E. Schloemann, and S. Stitzer, "Ferrite devices and materials," *IEEE Transactions on Microwave Theory and Techniques*, vol. 50, no. 3, pp. 721–737, 2002. DOI: 10.1109/22.989957.

[26] T. Dahm and D. J. Scalapino, "Theory of intermodulation in a superconducting microstrip resonator," *Journal of Applied Physics*, vol. 81, no. 4, pp. 2002–2009, Feb. 1997. DOI: 10.1063/1.364056.

[27] C. Collado, J. Mateu, R. Ferrus, and J. O'Callaghan, "Prediction of nonlinear distortion in HTS filters for CDMA communication systems," *IEEE Transactions on Applied Superconductivity*, vol. 13, no. 2, pp. 328–331, 2003. DOI: 10.1109/TASC.2003.813723.

[28] J. C. Booth, J. A. Beall, D. A. Rudman, L. R. Vale, and R. H. Ono, "Geometry dependence of nonlinear effects in high temperature superconducting transmission lines at microwave frequencies," *Journal of Applied Physics*, vol. 86, no. 2, pp. 1020–1027, Jul. 1999. DOI: 10.1063/1.370841.

[29] J. R. Wilkerson, I. M. Kilgore, K. G. Gard, and M. B. Steer, "Passive intermodulation distortion in antennas," *IEEE Transactions on Antennas and Propagation*, vol. 63, no. 2, pp. 474–482, 2015. DOI: 10.1109/TAP.2014.2379947.

[30] J. R. Wilkerson, K. G. Gard, and M. B. Steer, "Electro-thermal passive intermodulation distortion in microwave attenuators," in *2006 European Microwave Conference*, 2006, pp. 157–160. DOI: 10.1109/EUMC.2006.281242.

[31] Q. Jin, Q. Feng, G. T. Flowers, L. Bi, and J. Luo, "Effect of impedance discontinuity induced by line bending on passive intermodulation in connector-microstrip assemblies," *IEEE Microwave and Wireless Components Letters*, vol. 32, no. 9, pp. 1047–1050, 2022. DOI: 10.1109/LMWC.2022.3168039.

[32] J. Mateu, C. Collado, and J. M. O'Callaghan, "Modeling superconducting transmission line bends and their impact on nonlinear effects," *IEEE Transactions on Microwave Theory and Techniques*, vol. 55, no. 5, pp. 822–828, 2007.

[33] J. Luo, J. Gao, W. Zhuang, and Z. Wang, "Modeling of passive intermodulation induced by concentrated current density in bent coaxial connectors," *IEEE Transactions on Microwave Theory and Techniques*, vol. 72, no. 8, pp. 4457–4474, 2024.

[34] Q. Jin, J. Gao, G. T. Flowers, Y. Wu, and G. Xie, "Modeling of passive intermodulation with electrical contacts in coaxial connectors," *IEEE Transactions on Microwave Theory and Techniques*, vol. 66, no. 9, pp. 4007–4016, 2018. DOI: 10.1109/TMTT.2018.2838147.

[35] X. Chen, Y. He, S. Yang, *et al.*, "Analytic passive intermodulation behavior on the coaxial connector using monte carlo approximation," *IEEE Transactions on Electromagnetic Compatibility*, vol. 60, no. 5, pp. 1207–1214, 2018. DOI: 10.1109/TEMC.2018.2809449.

[36] H. Yang, H. Wen, Y. Qi, and J. Fan, "An equivalent circuit model to analyze passive intermodulation of loose contact coaxial connectors," *IEEE Transactions on Electromagnetic Compatibility*, vol. 60, no. 5, pp. 1180–1189, 2018. DOI: 10.1109/TEMC.2018.2794992.

[37] X. Zhao, Y. He, M. Ye, *et al.*, "Analytic passive intermodulation model for flange connection based on metallic contact nonlinearity approximation," *IEEE Transactions on Microwave Theory and Techniques*, vol. 65, no. 7, pp. 2279–2287, 2017. DOI: 10.1109/TMTT.2017.2668402.

[38] C. Ge, B. Duan, W. Wang, S. Qian, and S. Lou, "An equivalent circuit model for rectangular waveguide performance analysis considering rough flanges' contact," *IEEE Transactions on Microwave Theory and Techniques*, vol. 67, no. 4, pp. 1336–1345, 2019. DOI: 10.1109/TMTT.2019.2896556.

[39] Y. R. Mao, Y. Liu, Y. J. Xie, and Z. H. Tian, "Simulation of electromagnetic performance on mesh reflector antennas: Three-dimensional mesh structures with lumped boundary conditions," *IEEE Transactions on Antennas and Propagation*, vol. 63, no. 10, pp. 4599–4603, 2015. DOI: 10.1109/TAP.2015.2459133.

[40] Y. Liu, Y. R. Mao, Y. J. Xie, and Z. H. Tian, "Evaluation of passive intermodulation using full-wave frequency-domain method with nonlinear circuit model," *IEEE Transactions on Vehicular Technology*, vol. 65, no. 7, pp. 5754–5757, 2016. DOI: 10.1109/TVT.2015.2483738.

[41] J. A. Greenwood, J. B. P. Williamson, and F. P. Bowden, "Contact of nominally flat surfaces," *Proceedings of the Royal Society of London. Series A. Mathematical and Physical Sciences*, vol. 295, no. 1442, pp. 300–319, 1966. DOI: 10.1098/rspa.1966.0242.

[42] L. Kogut and I. Etsion, "A finite element based elastic-plastic model for the contact of rough surfaces," *Tribology Transactions*, vol. 46, no. 3, pp. 383–390, 2003. DOI: 10.1080/10402000308982641.

[43] J. G. Simmons, "Generalized formula for the electric tunnel effect between similar electrodes separated by a thin insulating film," *Journal of Applied Physics*, vol. 34, pp. 1793–1803, 1963.

[44] J. Russer, A. Ramachandran, A. Cangellaris, and P. Russer, "Phenomenological modeling of passive intermodulation (PIM) due to electron tunneling at metallic contacts," in *2006 IEEE MTT-S International Microwave Symposium Digest*, 2006, pp. 1129–1132. DOI: 10.1109/MWSYM.2006.249389.

[45] T. Bechtold, E. B. Rudnyi, and J. G. Korvink, "Dynamic electro-thermal simulation of microsystems—a review," *Journal of Micromechanics and Microengineering*, vol. 15, no. 11, R17, Oct. 2005. DOI: 10.1088/0960-1317/15/11/R01.

[46] R. E. Collin, *Foundations for Microwave Engineering, 2nd Edition*. New York: IEEE Press, Hoboken, N.J, 2001.

[47] R.M. Phillips, "The Ubitron, a high-power traveling-wave tube based on a periodic beam interaction in unloaded waveguide," *IRE Transactions on Electron Devices*, vol. 7, no. 4, pp. 231–241, 1960. DOI: 10.1109/T-ED.1960.14687.

[48] A. Nagra and R. York, "Distributed analog phase shifters with low insertion loss," *IEEE Transactions on Microwave Theory and Techniques*, vol. 47, no. 9, pp. 1705–1711, 1999. DOI: 10.1109/22.788612.

[49] D. Sievenpiper, J. Schaffner, H. Song, R. Loo, and G. Tangonan, "Two-dimensional beam steering using an electrically tunable impedance surface," *IEEE Transactions on Antennas and Propagation*, vol. 51, no. 10, pp. 2713–2722, 2003. DOI: 10.1109/TAP.2003.817558.

[50] C.-S. Lin, S.-F. Chang, C.-C. Chang, and Y.-H. Shu, "Design of a reflection-type phase shifter with wide relative phase shift and constant insertion loss," *IEEE Transactions on microwave theory and techniques*, vol. 55, no. 9, pp. 1862–1868, 2007.

[51] C.-S. Lin, S.-F. Chang, and W.-C. Hsiao, "A full-360° reflection-type phase shifter with constant insertion loss," *IEEE microwave and wireless components letters*, vol. 18, no. 2, pp. 106–108, 2008.

[52] K. Miyaguchi, M. Hieda, K. Nakahara, *et al.*, "An ultra-broad-band reflection-type phase-shifter MMIC with series and parallel LC circuits," *IEEE Transactions on Microwave Theory and Techniques*, vol. 49, no. 12, pp. 2446–2452, 2001.

[53] H. A. Atwater, "Circuit design of the loaded-line phase shifter," *IEEE Transactions on Microwave Theory and Techniques*, vol. 33, no. 7, pp. 626–634, 1985.

[54] H.-C. Chiu, C.-M. Chen, L.-C. Chang, and H.-L. Kao, "A 5-bit X-band GaN HEMT-based phase shifter," *Electronics*, vol. 10, no. 6, p. 658, 2021.

[55] M. Rodwell, M. Kamegawa, R. Yu, M. Case, E. Carman, and K. Giboney, "GaAs nonlinear transmission lines for picosecond pulse generation and millimeter-wave sampling," *IEEE Transactions on Microwave Theory and Techniques*, vol. 39, no. 7, pp. 1194–1204, 1991. DOI: 10.1109/22.85387.

[56] S. A. Maas, *Nonlinear Microwave Circuits*. Norwood, MA: Artech House, 1988.

[57] Skyworks Solutions, Inc, *SMV123x series: Hyperabrupt junction tuning varactors*, https://www.skyworksinc.com/-/media/SkyWorks/Documents/Products/101-200/SMV123x_Series_200058AA.pdf, [Online; accessed January 2025], 2020.

[58] Infineon Technologies AG, *Silicon Schottky Diode - BAT63 Series*, https://www.infineon.com/dgdl/Infineon-BAT63SERIES-DS-v01_01-en.pdf?fileId=db3a304314dca38901151817843c0df4, [Online; accessed January 2025], 2011.

[59] G. Engen and C. Hoer, "Thru-reflect-line: An improved technique for calibrating the dual six-port automatic network analyzer," *IEEE Transactions on Microwave Theory and Techniques*, vol. 27, no. 12, pp. 987–993, 1979. DOI: 10.1109/TMTT.1979.1129778.

[60] Y. Wang, Q. Tan, F. Pu, D. Boone, and M. Zhang, "A review of the application of additive manufacturing in prosthetic and orthotic clinics from a biomechanical perspective," *Engineering*, vol. 6, no. 11, pp. 1258–1266, 2020. DOI: https://doi.org/10.1016/j.eng.2020.07.019.

[61] C. Tomassoni, O. A. Peverini, G. Venanzoni, G. Addamo, F. Paonessa, and G. Virone, "3D printing of microwave and millimeter-wave filters: Additive manufacturing technologies applied in the development of high-performance filters with novel topologies," *IEEE Microwave Magazine*, vol. 21, no. 6, pp. 24–45, 2020. DOI: 10.1109/MMM.2020.2979153.

[62] F. Calignano, D. Manfredi, E. P. Ambrosio, *et al.*, "Overview on additive manufacturing technologies," *Proceedings of the IEEE*, vol. 105, no. 4, pp. 593–612, 2017. DOI: 10.1109/JPROC.2016.2625098.

[63] D. Manfredi, F. Calignano, M. Krishnan, *et al.*, "Additive manufacturing of Al alloys and aluminium matrix composites (AMCs)," in *Light Metal Alloys Applications*, W. A. Monteiro, Ed., Rijeka: IntechOpen, 2014, ch. 1. DOI: 10.5772/58534.

[64] Y. S. Hedberg, B. Qian, Z. Shen, S. Virtanen, and I. Odnevall Wallinder, "In vitro biocompatibility of CoCrMo dental alloys fabricated by selective laser melting," *Dental Materials*, vol. 30, no. 5, pp. 525–534, 2014. DOI: https://doi.org/10.1016/j.dental.2014.02.008.

[65] T. Kurzynowski, E. Chlebus, B. Kuźnicka, and J. Reiner, "Parameters in selective laser melting for processing metallic powders," in *Proc. SPIE*, vol. 8239, 2012. DOI: 10.1117/12.907292.

[66] H. Niu and I. Chang, "Instability of scan tracks of selective laser sintering of high speed steel powder," *Scripta Materialia*, vol. 41, no. 11, pp. 1229–1234, 1999. DOI: https://doi.org/10.1016/S1359-6462(99)00276-6.

[67] R. Villa, Y. Liu, and Z. Siddique, "Review of defects and their sources in as-built Ti6Al4V manufactured via powder bed fusion," *The International Journal of Advanced Manufacturing Technology*, vol. 132, pp. 4105–4134, 2024.

[68] A. Charles, M. Bayat, A. Elkaseer, L. Thijs, J. H. Hattel, and S. Scholz, "Elucidation of dross formation in laser powder bed fusion at down-facing surfaces: Phenomenon-oriented multiphysics simulation and experimental validation," *Additive Manufacturing*, vol. 50, p. 102 551, 2022. DOI: https://doi.org/10.1016/j.addma.2021.102551.

[69] A. Leon, A. Shirizly, and E. Aghion, "Corrosion behavior of AlSi10Mg alloy produced by additive manufacturing (AM) vs. its counterpart gravity cast alloy," *Metals*, vol. 6, no. 7, 2016.

[70] P. Ansuinelli, A. G. Schuchinsky, F. Frezza, and M. B. Steer, "Passive intermodulation due to conductor surface roughness," *IEEE Transactions on Microwave Theory and Techniques*, vol. 66, no. 2, pp. 688–699, 2018. DOI: 10.1109/TMTT.2017.2784817.

[71] E. Rocas, C. Collado, N. D. Orloff, *et al.*, "Passive intermodulation due to self-heating in printed transmission lines," *IEEE Transactions on Microwave Theory and Techniques*, vol. 59, no. 2, pp. 311–322, 2011. DOI: 10.1109/TMTT.2010.2090356.

[72] J. Mateu, C. Collado, N. Orloff, *et al.*, "Third-order intermodulation distortion and harmonic generation in mismatched weakly nonlinear transmission lines," *IEEE Transactions on Microwave Theory and Techniques*, vol. 57, no. 1, pp. 10–18, 2009.

[73] J. Morgan Samuel P., "Effect of surface roughness on eddy current losses at microwave frequencies," *Journal of Applied Physics*, vol. 20, no. 4, pp. 352–362, Apr. 1949. DOI: 10.1063/1.1698368.

[74] E. Hammerstad and O. Jensen, "Accurate models for microstrip computer-aided design," in *1980 IEEE MTT-S International Microwave symposium Digest*, 1980, pp. 407–409. DOI: 10.1109/MWSYM.1980.1124303.

[75] S. Groiss, I. Bardi, O. Biro, K. Preis, and K. Richter, "Parameters of lossy cavity resonators calculated by the finite element method," *IEEE Transactions on Magnetics*, vol. 32, no. 3, pp. 894–897, 1996. DOI: 10.1109/20.497385.

[76] P. G. Huray, S. Hall, S. Pytel, *et al.*, "Fundamentals of a 3-D "snowball" model for surface roughness power losses," in *2007 IEEE Workshop on Signal Propagation on Interconnects*, 2007, pp. 121–124.

[77] L. Simonovich, "Practical method for modeling conductor surface roughness using the cannonball stack principle," in *Proc. Int. Conf. Des.*, 2015, pp. 1–23.

[78] Q. M. Khan and D. Kuylenstierna, "Analysis of Q-factor for AM-SLM cavity based resonators using surface roughness models," *IEEE Journal on Multiscale and Multiphysics Computational Techniques*, vol. 9, pp. 75–83, 2024.

[79] V. K. Patel, R. Kant, A. choudhary, M. Painuly, and S. Bhattacharya, "Performance characterization of Bi2O3/Al nanoenergetics blasted microforming system," *Defence Technology*, vol. 15, no. 1, pp. 98–105, 2019.

[80] D. Zelenchuk, A. Shitvov, A. Schuchinsky, and V. Fusco, "Discrimination of passive intermodulation sources on microstrip lines," 6th International Workshop on Multipactor, Corona and Passive Intermodulation in Space RF Hardware, PIM Session 1, MULCOPIM 2008.

[81] J. Booth, K. Leong, S. Schima, J. Mateu, C. Collado, and J. O'Callaghan, "A unified description of nonlinear effects in high temperature superconductor microwave devices," *Journal of Superconductivity and Novel Magnetism*, vol. 19, no. 7/8, pp. 531–540, 2006.

[82] D. M. Pozar, *Microwave engineering*. Hoboken, NJ: Wiley, 2012.

[83] T.-S. Chen, "Determination of the capacitance, inductance, and characteristic impedance of rectangular lines," *IRE Transactions on Microwave Theory and Techniques*, vol. 8, no. 5, pp. 510–519, 1960. DOI: 10.1109/TMTT.1960.1124779.

[84] A. Milovanovic and B. Koprivica, "Analysis of square coaxial lines by using equivalent electrodes method," in *Proceedings of the Joint INDS'11 & ISTET'11*, 2011, pp. 1–6. DOI: 10.1109/INDS.2011.6024808.

[85] S. Seghier, N. Benabdallah, N. Benahmed, N. Benmostefa, and R. Bouhmidi, "Accurate closed-form formulas for the electromagnetic parameters of squared coaxial lines," *AEU - International Journal of Electronics and Communications*, vol. 62, no. 5, pp. 395–400, 2008. DOI: https://doi.org/10.1016/j.aeue.2007.05.010.

[86] S. M. Musa and M. N. O. Sadiku, "Analysis of rectangular coaxial lines," in *2007 IEEE Region 5 Technical Conference*, 2007, pp. 322–325. DOI: 10.1109/TPSD.2007.4380328.

[87] A. Milovanović and M. Bjekić, "Approximate calculation of capacitance of lines with multilayer medium," *Journal of Electrical Engineering*, vol. 62, no. 5, pp. 249–257, 2011.

[88] M. Hołyńska, A. Tighe, and C. Semprimoschnig, "Coatings and thin films for spacecraft thermo-optical and related functional applications," *Advanced Materials Interfaces*, vol. 5, no. 11, p. 1 701 644, 2018. DOI: https://doi.org/10.1002/admi.201701644.

[89] Beyond Gravity, *Antennas for GNSS Receivers*, https://www.beyondgravity.com/sites/default/files/media_document/2024-07/Antennas_for_GNSS_receivers_D-I-PRB-00029-SE_01-24.pdf, [Online; accessed January 2025], 2024.

[90] S. Gao, K. Clark, M. Unwin, *et al.*, "Antennas for modern small satellites," *IEEE Antennas and Propagation Magazine*, vol. 51, no. 4, pp. 40–56, 2009. DOI: 10.1109/MAP.2009.5338683.

[91] Q. Jin, J. Gao, G. T. Flowers, Y. Wu, G. Xie, and L. Bi, "Modeling of passive intermodulation in connectors with coating material and iron content in base brass," *IEEE Transactions on Microwave Theory and Techniques*, vol. 67, no. 4, pp. 1346–1356, 2019. DOI: 10.1109/TMTT.2019.2893193.

[92] A. Raveh, Z. Tsameret, and E. Grossman, "Surface characterization of thin layers of aluminium oxide," *Surface and Coatings Technology*, vol. 88, no. 1, pp. 103–111, 1997. DOI: https://doi.org/10.1016/S0257-8972(95)02757-2.

[93] S.-H. Yu, D. Jang, and K.-S. Lee, "Effect of radiation in a radial heat sink under natural convection," *International Journal of Heat and Mass Transfer*, vol. 55, no. 1, pp. 505–509, 2012. DOI: https://doi.org/10.1016/j.ijheatmasstransfer.2011.09.026.

[94] C. C. He and T. M. Heslin, "Preventing cracking of anodized coatings," *NASA Technical Memorandum, 104622*, 1995.

[95] R. S. Alwitt, J. Xu, and R. C. McClung, "Stresses in sulfuric acid anodized coatings on aluminum," *Journal of The Electrochemical Society*, vol. 140, no. 5, p. 1241, May 1993.

[96] M. Silicani and S. Ricard, "Presentation of MDA PIM test facility capabilities and studies of PIM order amplitude relationship and PIM level variation as a function of transmit power flux density," *Proc. 9th Int. Workshop Multipactor, Corona Passive Intermodulation*, pp. 1–9, Apr. 2017.

[97] M. A. Yeganeh, S. Rahmatallahpur, A. Nozad, and R. K. Mamedov, "Effect of diode size and series resistance on barrier height and ideality factor in nearly ideal Au/n type-GaAs micro schottky contact diodes," *Chinese Physics B*, vol. 19, no. 10, p. 107 207, Oct. 2010. DOI: 10.1088/1674-1056/19/10/107207.

[98] C. Fager, J. Pedro, N. de Carvalho, H. Zirath, F. Fortes, and M. Rosario, "A comprehensive analysis of IMD behavior in RF CMOS power amplifiers," *IEEE Journal of Solid-State Circuits*, vol. 39, no. 1, pp. 24–34, 2004. DOI: 10.1109/JSSC.2003.820860.